Anne-Kristine Meland

Impedance Diagrams of the Electrodes in the Polymer Electrolyte Membrane Fuel Cell

Thesis for the degree philosophiae doctor

Trondheim, October 2007

Norwegian University of Science and Technology
Faculty of Natural Sciences and Technology
Department of Chemistry

NTNU
Norwegian University of Science and Technology

Thesis for the degree philosophiae doctor

Faculty of Natural Sciences and Technology
Department of Chemistry

ISBN 978-82-471-3926-4 (printed version)
ISBN 978-82-471-3943-1 (electronic version)
ISSN 1503-8181

Doctoral theses at NTNU, 2007:179

Printed by NTNU-trykk

Acknowledgement

This thesis is the result of my Ph.D. study at the Department of Chemistry, Norwegian University of Science and Technology (NTNU). My study has been made possible by financial support by Nordic Energy Research, Hydro Norge ASA, and the Department of Chemistry. I would like to thank my current employer, Reinertsen Engineering AS, for financial support during the finishing of this work.

Especially I would like to thank my supervisor, Professor Signe Kjelstrup, for excellent guidance and encouragement. She never stopped believing in me and was able to motivate me to keep trying. Also her husband Dick Bedeaux is thanked for the work with the theory.

I also thank all my colleagues in the Physical Chemistry group. The coffee breaks with all the discussions were enjoyable. Terje Bruvoll is thanked for financing experimental equipment that made it possible to do all the measurements. Preben Vie is thanked for helping me with the test facility in the laboratory and always being helpful when problems occurred - and they did. A special thanks also to Rune Halseid for invaluable help. I am fortunate to have had the opportunity to discuss my work with someone with that experimental experience and theoretical knowledge.

Most of all I want to thank my dear Rune for an absolute and continues support and for always believing in me. My beloved daughters, Elise and Signe, are thanked for their unconditionally love. They were a good distraction from work.

This thesis is dedicated to my late parents, Signe and Albert Meland.

Summary

The objective of this thesis was to better understand the electrodes of the polymer electrolyte membrane fuel cell (PEMFC), and especially the anode. We were interested in how CO poisoning affected the fuel cell and therefore we started by looking at the unpoisoned anode. It was important to get a good understanding of the mechanisms of the unpoisoned electrode to have a good background to understand the poisoned one.

The electrodes were investigated using *in situ* electrochemical impedance spectroscopy (EIS). The cell studied in all experiments consisted of two similar E-TEK Elat gas diffusion electrodes (Elat/Std/DS/V2) with 0.5 mg/cm^2 Pt loading and 20% Pt/C. The electrodes were sprayed with a 5 wt% Nafion solution to give 0.6 mg/cm^2. The two electrodes were separated by a Nafion 117 membrane. A two electrode set-up was used in all the experiments. Symmetric cells were used, $H_2|H_2$ and $O_2|O_2$, to avoid using a reference electrode. In addition, experiments with the whole fuel cell, $H_2|O_2$, were done. The frequency range used in the EIS experiments was 10 kHz-10 mHz. The operating temperatures were 30 and 50°C.

We started out by investigate the unpoisoned anode using EIS and a symmetrical hydrogen cell, and we discovered the Gerischer behaviour in the low frequency area. This showed that hydrogen diffused along the carbon pores in the electrode and that the adsorption reaction took place in combination with surface diffusion of hydrogen in the carbon layer located before the platinum surface. The reaction was thus not only dependent of the platinum catalyst particles. We were not able to distinguish between molecular or atomic adsorption. The relaxation time for this rate-limiting adsorption/diffusion step was independent of bias voltage. In Chapter 2 we show the results for this Gerischer phase element and included this in the equivalent circuit. The equivalent circuit consisted of two rate-limiting steps, one charge transfer step taking place

at the platinum particles and one adsorption/diffusion step. The equivalent circuit was determined from irreversible thermodynamics.

We discovered a third rate limiting step at the anode. The third step was the proton hydration step. In Chapter 3 we show that water plays an important role at the anode. The arc was seen at the highest frequencies in the Nyquist diagram. This third step was best seen at the low temperature, 30°C, at 50°C this small arc was superimposed on the charge transfer arc in the Nyquist plot. Again we saw the Gerischer behaviour. An equivalent circuit with three rate limiting steps was determined using irreversible thermodynamics. The surface coefficient of hydrogen diffusion was estimated to 10^{-7} m^2/s.

In Chapter 4, we saw how the anode and the whole fuel cell reacted when 103 ppm carbon monoxide (CO) was introduced in the fuel gas. Bias voltages of 0 and 0.05 V were used. Three steps were again revealed in the reaction mechanism, the charge transfer step, the adsorption/diffusion step, and the proton hydration step. This confirmed earlier results from the unpoisoned anode. The CO had a big effect on the charge transfer step and the relaxation time increased drastically. The relaxation time for the adsorption/diffusion step was unaffected by the CO. We also concluded that CO reduces the diffusion rate of the surface diffusion of hydrogen on carbon. Also the relaxation time for the proton hydration step was unaffected by CO. CO hindered hydrogen access to the Pt surface, occupied the Pt surface and made the surface more polarisable. These results supported the results from the two previous chapters. From cyclic voltammetry and stripping voltammetry experiments we found the CO coverage to be 0.90 at 30°C and 0.85 at 50°C.

In Chapter 5 we looked at the oxygen electrode and the oxygen reduction reaction (ORR). A symmetric oxygen cell was investigated both in the potentiostatic and galvanostatic mode. The oxygen electrode was not reversible and the whole fuel cell was also investigated at the same conditions as the symmetric oxygen. The anodic and cathodic contribution of the oxygen electrode were then discovered. We found two rate-limiting steps. One dominating arc in the Nyquist diagram related to the charge transfer reaction and one small high frequency arc that we assigned to a proton dehydration step. This small high frequency arc did not change with the bias voltage. We believe we had peroxide formation followed by decomposition of peroxide. The Butler-Volmer equation was also fitted to the experimental data. The transfer coefficient β was determined to 0.70 ± 0.03 and the exchange current density, j_0 was $(9.42 \pm 0.01)10^{-5}$ A/cm^2.

Nomenclature

Roman letters

A	constant	
C	capacitance	$\mathrm{F/m^2}$ or $\mathrm{s/\Omega\ m^2}$
c_i^{a}	surface excess concentration	$\mathrm{mol/m^2}$
c_i	concentration	$\mathrm{mol/m^3}$
D	diffusion coefficient	$\mathrm{m^2/s}$
D	displacement field	$\mathrm{C/m^2}$
d	thickness of layer	m
F	Faraday's constant	96484 C/mol
f	fugacity	bar
G	Gibbs energy	J/mol
J_i	flux of component i	$\mathrm{mol/s\ m^2}$
j	current density	$\mathrm{A/cm^2}$
j_0	exchange current density	$\mathrm{A/cm^2}$
k	rate constant	1/s
l	length	m
P^{s}	polarisation of the surface	C/m
p	pressure	bar
Q	charge	$\mathrm{C/m^2}$
R	gas constant	8.3145 J/K mol
R	area specific resistance	$\mathrm{\Omega\ cm^2}$

r	reaction rate	mol/s m^3
T	temperature	K
T	admittance parameter	$s^{\alpha}/\Omega\ cm^2$
t	time	s
t_{H_2O}	transport number for water	
u	ion mobility in an electric field	m^2/s V
x	coordinate axis	m
Y_0	admittance parameter	$s^{1/2}/\Omega\ cm^2$
Z	impedance	$\Omega\ cm^2$

Greek letters

α_i	angle parameter	
β	overall transfer coefficient	
η	overpotential	V
ε_0	Dielectric constant of vacuum	8.854×10^{-12} C^2/ J m
Γ^s	surface adsorption	mol/m^2
γ	activity coefficient	
γ	surface coordinate, position	
λ	Number of water molecules per sulfonic group in the membrane	
ϕ	electric potential	V
μ	chemical potential	J/mol
ρ	area specific resistivity	$\Omega\ cm^2$
σ^s	entropy production rate of surface	J/K m^2
τ	relaxation time	s
θ	coverage	
ω	frequency	1/s

Sub- and superscripts

a	adsorption
a	anodic
ac	alternating current
ad	adsorption
c	cathodic
cm	proton hydration
ct	charge transfer
d	diffusion
dc	direct current
eq	equilibrium
g	gas
i	species i
m	membrane
p	dipole
s	surface
W	Warburg

Abbreviations

ACL	Anode catalyst layer
AFC	Alkaline fuel cell
CL	Catalytic layer
CCL	Cathode catalyst layer
CPE	Constant phase element
EIS	Electrochemical impedance spectroscopy
CV	Cyclic voltammetry
GDL	Gas diffusion layer
HOR	Hydrogen oxidation reaction
Im	Imaginary

MEA	Membrane- and electrode assembly
OCV	Open circuit voltage
ORR	Oxygen reduction reaction
PAFC	Phosophoric acid fuel cell
PEM	Polymer electrolyte membrane or proton exchange membrane
PEMFC	Polymer electrolyte membrane fuel cell
Re	Real
SEM	Scanning electron microscope

Contents

Chapter 1

Introduction

1.1 Background

1.1.1 Fuel cell history

The "fuel cell effect" was first discovered by C. F. Schoenbein. In January 1839 he reported on current caused by combining hydrogen and oxygen. The first working fuel cell was invented by W.R. Grove (1842). By connecting a hydrogen anode and an oxygen cathode, he produced an electric current [1]. Grove identified the control of the interfaces between the electrolyte, electrocatalyst and reactant gas [2]. Since then, there have been several attempts to apply it for more than 100 years but none were very successful. Fuel cell technology was too crude and inefficient and could not compete with the dynamo invented by von Siemen. F. T. Bacon developed the modern alkaline fuel cell (AFC) in the 1930s that used alkaline electrolyte and nickel electrodes [3]. This was the first approach towards fuel cell commercialisation and he could in 1959 demonstrate AFC stack producing up to 5 kW [3]. Later the same year, H. K. Ihrig demonstrated the first fuel cell powered veichle. By combining 1008 cells he produced a fuel stack that produced 15 kW and was capable of powering a 20 horsepower tractor [4].

In the early 1960s General Electric (GE) developed with NASA the Grubb-Niedrach fuel cell. This fuel cell hade a sulphonated polystyrene ion-exchange membrane as the electrolyte (a solid electrolyte). This was the first application of a polymer electrolyte membrane (PEM), also referred to as proton exchange membrane. Platinum was deposited on to this membrane. This fuel cell was

used on the Gemini space project and was the first commercial use of a fuel cell. AFC was used in the Apollo space-program. This cell had better performance and durability compared to the PEM fuel cell. Alkali cells have been used since on most subsequent missions [5].

In 1973 an oil embargo renewed interest in fuel cells for terrestrial applications. A number of companies and organisations began serious research. The phosphoric acid fuel cell (PAFC) plant were manufactured and became commercially available in the early 1990s.

Membranes with better stability and performance than used in the Gemini fuel cell stack were developed. The first major advance in PEM fuel cells lifetime came when DuPont developed the Nafion membrane. This is still today the PEM choice [2].

Possibly the most significant barrier that PEM fuel cells had to overcome was the costly amount of platinum required as a catalyst. The large amount of platinum in original PEM fuel cells is one of the reasons why fuel cells were excluded from commercialisation. An effort was made to reduce the quantities of electrocatalyst used in the membrane-electrode assembly (MEA). Two significant steps in the development of the catalyst layer (CL) of the PEM fuel cell were the use of highly dispersed Pt catalyst, with particle size in the range 1-10 nm, deposited on high-surface-area carbon, as well as impregnation with Nafion ionomere. This enabled the reduction of catalyst loadings from 4-10 mg Pt/cm^2 to about 0.2 mg Pt/cm^2 [6].

Today the PEM fuel cell is the most promising low-temperature fuel cell for transportation applications since it is very compact. The fuel cell technology has the potential of meeting the needs of stationary and portable electricity generation as well as battery replacements.

1.1.2 Polymer electrolyte membrane fuel cells today

Because of their potential to reduce the environmental impact and consequences of the use of fossil fuels, fuel cells have emerged as attractive alternatives to combustion engines. Like a combustion engine, a fuel cell uses some sort of chemical fuel as its energy source, but like a battery, the chemical energy is directly converted to electrical energy. In addition to high efficency and low emissions, fuel cells are attractive for their modular and distributed nature, and zero noise pollution.

Currently there is a lot of focus on PEM fuel cells for transportation veichles and an example of a recent achievement of the PEM fuel cell is the General Motors (GM) fuel cell car Chevrolet Sequel. On May 15. 2007 the Chevrolet Sequel was the first electrically driven fuel cell veichle to achieve 480 km on one tank of hydrogen, in and out on traffic on public roads [7]. Three lightweight, carbon composite tanks stored hydrogen at 700 bars and carried 8 kg of hydrogen. The hydrogen had been generated from a hydro power plant near Niagara Falls using hydro-electro power from the falls so no fossil fuels were used to power them.

The PEM fuel cell has high power density, relatively quick start-up, rapid response to varying loads, and low operating temperatures [8, 9]. The primary components of a PEM fuel cell are an ion conducting electrolyte, a cathode, and an anode. Together these three are often referred to as the membrane-electrode assembly (MEA). In its simplest form, the MEA consists of a membrane, two dispersed catalyst layers, and two gas diffusion layers (GDL). The membrane separates the half reactions allowing protons to pass through to complete the overall reaction. The electron created on the anode side is forced to flow through an external circuit thereby creating current. The GDL allows direct and uniform access of the fuel and oxidant to the catalyst layer, which stimulates each half reaction.

An effective electrode is one that correctly balances the transport processes required for an operational fuel cell. The three transport processes required are the transport of 1) protons from the membrane to the catalyst, 2) electrons from the current collector to the catalyst through the gas diffusion layer, and 3) the reactant and product gases to and from the catalyst layers and the gas channels. Protons, electrons, and gas belongs to the three phases found in the catalyst region. Part of the optimisation of electrode design is the attempt to correctly distribute the amount of volume in the catalyst layer between the transport media for each of the three phases to reduce transport losses.

Most efforts in the electrode theory and experiments focus on the cathode catalyst layer (CLL). The oxygen reduction reaction (ORR) occurs in the CCL and here we find 30-40% of the total performance loss in the PEMFC. It is also important to focus on the anode catalyst layer and the hydrogen oxidation reaction (HOR). The anode does not contribute significant to the total loss in the PEMFC when the fuel is neat. But when the fuel is contaminated with CO, then the performance loss is due to the anode and the anode catalyst layer (ACL). It is therefore of great importance to know the mechanisms of

the unpoisoned ACL to be able to understand in detail how CO affects the ACL and the cell performance.

Impurities in hydrogen fuel and in air are brought along with the fuel and air feed streams into the anodes and cathodes of a PEM fuel cell causing performance degradation, and sometimes permanent damage to the MEA [10]. The hydrogen impurities can be CO, H_2S, NH_3, organicsulfur-carbon, and carbon-hydrogen compounds. They are mainly from the manufacturing process, in which natural gas or other small organic fuels are reformed to produce hydrogen gas with a small amount of impurities. It has been identified that the MEA is mostly affected by a contamination process. Three major effects have been identified [10]: Kinetic effect, e.g. poisoning of the electrode, conductivity effect (increase in the solid electrolyte resistance), and mass transfer effect (catalyst layer structure and hydrophobility changes causes a mass transfer problem). In PEM fuel cells using reformate H_2-rich gas as a fuel, CO has become a major concern because it binds strongly to Pt sites, resulting in the reduction of surface active sites available [11, 12]. The poisoning effect is strongly related to the CO concentration, the exposure time to CO, the operation temperature in the cell, and anode catalyst type. The presence of CO impurities in the anode hydrogen fuel could also significantly affect the cathode, probably primarily through pin-holes in the membrane [13, 14].

Pt is still the only known catalyst that provides acceptable reaction rates at operating temperatures in PEMFC. Electrocatalyst development is fundamental to performance enhancement and cost reduction. New alloys are being developed to reduce cost, enhance performance and operational flexibility like CO-tolerance etc. [2]. Non-noble catalysts for PEMFC are also a focus for researchers [15, 16]. Today only about 40% of the expensive Pt in the catalytic layer is utilised [6]. New techniques for catalyst application are being developed to be able to increase the Pt utilisation [17, 18, 19].

The GDL is also subject for research. Materials like carbon-fibre paper, cloth materials and non-woven materials. Nanoparticle surfaces are also studied. These extremely small particles affect the electronic structure of the Pt/C system and changes the catalyst surface heterogeneity [2].

The proton exchange membrane component stands out as being of great importance. Today the perfluorosulfonic acid PEM is the only commercial membrane [2]. Several developments activities are underway [20]. The focus is on addressing improved performance and reliability, dramatic cost reduction, ease of manufacture, optimisation for use in specific applications, operation under

reduced or zero external humidification and high-temperature operation.

Various porous gas-diffusion electrode models that also have been used for the PEMFC, have developed since the late 1960's [21, 22, 23]. Most of these models have treated the electrodes in their steady state [24, 25, 26]. The dynamic response of the system, the topic of this investigation, was also studied [27, 28]. Most of the focus has been on the oxygen electrode.

Several researchers have used EIS and studied the porous gas diffusion electrodes used in the PEM fuel cell. Both the anode and the cathode have been studied in addition to the whole fuel cell [29]. A lot of the experiments done at the anode are done at higher temperatures, i.e. 50° and more. Ciureanu and Wang [30] looked at the symmetric hydrogen cell in a two electrode set-up using EIS and found two rate-limiting steps. These were assigned to the charge transfer across the interface and the dissociative chemisorption of hydrogen at the electrode. They also studied the effect of CO poisoning of the anode. Also Kim et al. [31] studied the symmetric hydrogen cell with and without CO poisoning. They found three rate limiting processes. They assigned this new third arc in the Nyquist plot to gas phase diffusion of hydrogen.

Some experimental investigations on the symmetric oxygen cell (ORR) have been done. Romero-Castanon et al. [32] investigated the MEA in the PEM fuel cell using a reference electrode to separate the anode and cathode contribution. They discovered two rate-limiting processes at the oxygen electrode at all potentials, including OCV. Hombrados and coworkers [33] also discovered two rate limiting steps at OCV conditions.

There is no consensus about the equivalent circuit representing the anode and cathode. Based on experimental data up until today several equivalent circuits that represents the electrodes are presented. However the data does not converge towards one model and there are still uncertainties connected to the modelling of the processes taking place at the electrodes. This thesis shall present experimental results that can help this model development.

1.2 Thermodynamics

The second law of thermodynamics states that the entropy change of the system plus its surroundings is zero for a reversible process and positive for an irreversible process. The second law gives the direction for the process but it does not give the rate [34]. Non-equilibrium thermodynamics can be used to derive this rate equations. Our interest is the transport of heat, mass, charge

and chemical reactions at the electrode surface. We shall use this theory as developed by Kjelstrup and Bedeaux [35] for the porous gas-diffusion electrode.

1.2.1 Excess properties of the surface

Heterogenous systems with transport of heat, mass, and charge are important in industry as well as in nature. Evaporation and condensation are examples of mass and heat transport. All electrochemical cells have such transport properties at their electrodes. In a fuel cell, chemical reactions take place at the electrode surface converting chemical energy into electrical energy. This can be described by non-equilibrium thermodynamics for surfaces. The theoretical foundation is described elsewhere. Here a short overview of essential points shall be given.

Most of the dissipation of energy in a fuel cell takes place at the electrode surfaces. A surface or interface is the thin layer between two homogenous phases. The thermodynamics properties of the surface are given by the values of the excess properties [34]. Gibbs choose this way to allocate surface energies to a particular position. Properties of a layer are then integrated out.

We describe our system as having flat surfaces and in this respect our description differ from others. The two-dimensional surface is shown in Fig. 1.1.

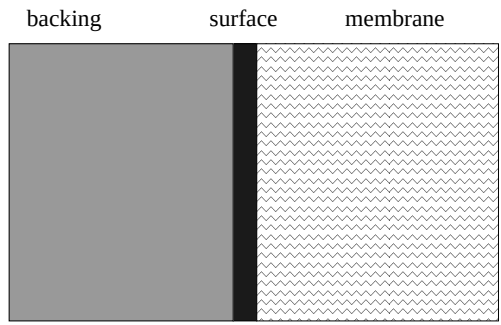

Figure 1.1. The two-dimensional electrode surface with its adjacent membrane and backing as they are used in the description.

In real life this surface is agglomoratic, but by integrating over the surfaces we can then look upon them as flat surfaces and choose the x-axis perpendicular to the surface to describe transport. The backing and membrane are continues phases as described also by others. A schematic picture of PEM fuel cell is shown in Fig. 1.2.

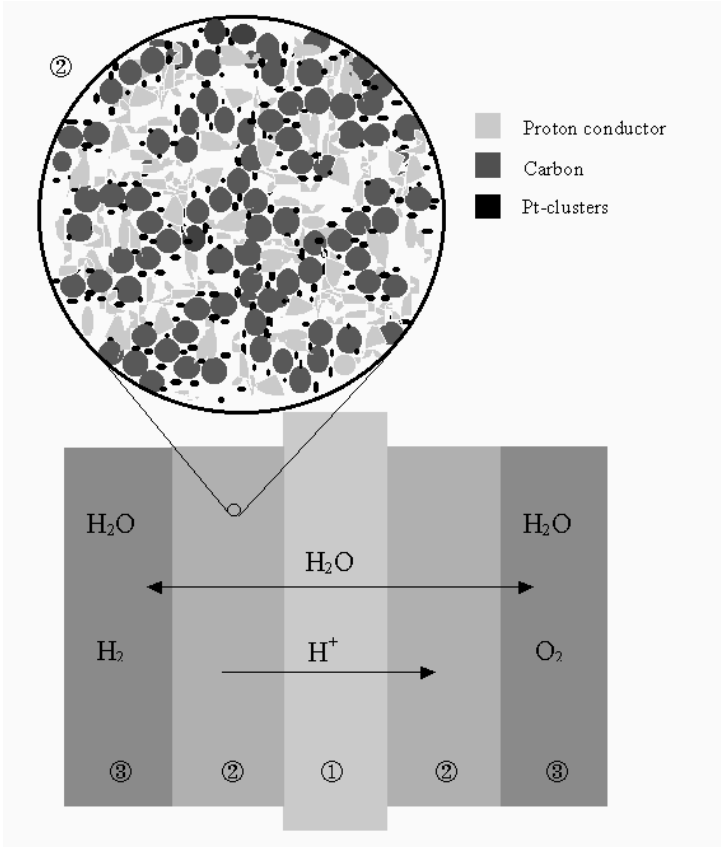

Figure 1.2. A schematic picture of the polymer electrolyte fuel cell. The membrane (1), the electrode surfaces (2) and the electrode backings (3) are shown. Courtesy of Steffen Møller-Holst.

The system contains of five subsystems. The mid section (labelled 1) is the water-containing membrane. The membrane has an anode surface to the left and a cathode surface to the right (labelled 2). The outer sections are the porous carbon matrixes (labelled 3) that transport gas, charge and heat. Humidified hydrogen diffuses through the pores in the carbon backing and reaches the catalytic platinum in the surface. Here it reacts and forms protons and electrons. The electrons go into the carbon matrix while the protons go into the proton conducting electrolyte membrane.

The densities in the carbon backing, the anode surface, and in the membrane are illustrated in Fig. 1.3. Here we see the variation in the densities of the components in the surface, membrane and anode layer of the electrode. The

density function of platinum (Pt) has a peak in the surface and the density function of adsorbed hydrogen will follow the one of Pt. The membrane will have the highest density of water. The highest density of fuel (H_2) will be in the carbon backing and this will decrease as the fuel moves through the surface and reacts. By integrating the area under these density functions the excess concentration can be found. These excess concentrations are shown in Fig. 1.4.

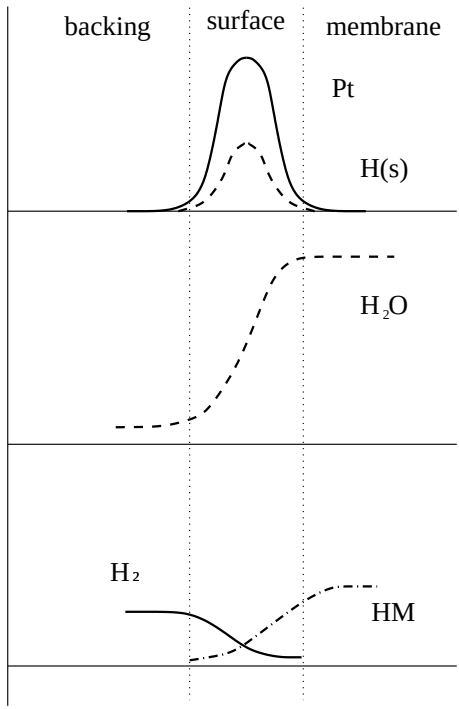

Figure 1.3. The density functions of the electrode surface.

With the help of these excess variables we define the surface as a surface in local equilibrium according to Gibbs and can find its excess entropy production rate and be able to use thermodynamics and model the dynamic processes at the surface. One can then write transport equations (fluxes and driving forces) for the surface. The fluxes are here the mass fluxes and the current density (per unit of membrane area). The driving forces are jumps in chemical and electric potentials at the surface, see [35] for more details.

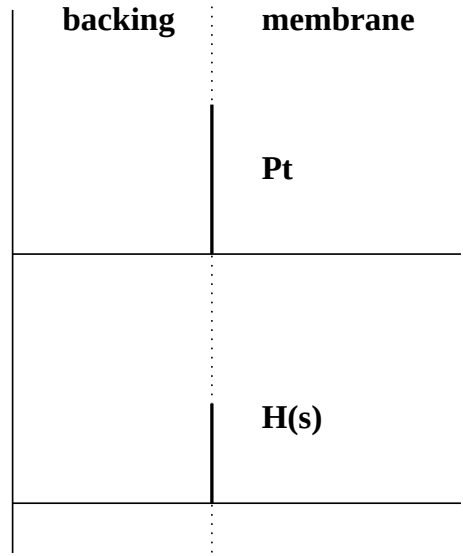

Figure 1.4. Excess concentrations of the electrode surface.

1.3 Aim and outline of thesis

The aim of this doctoral work is to provide more experimental data that can improve the current understanding of the physical processes taking place at the electrodes in the PEM fuel cell. The data shall be reduced using a theoretical model based on irreversible thermodynamics.

Modelling activities have increased the speed and reliability of the fuel cell development. Also development of analytical techniques (SEM, CV, EIS and more) that reveals the microstucure, function, interaction, and performance of the components continues to advance the characterisation and optimisation of the PEMFC.

The fundamental difficulties associated with fuel cell design stem from the nonlinear coupling. Several tens of operational, transport, kinetic, and design parameters which characterise fuel cells exists, most of them strongly linked [6]. The fuel cell system must therefore be designed as a whole.

In order to understand this complex system it is necessary to have thorough knowledge of the basic physical and chemical processes taking place in the system. Only when the various processes are identified and one knows about their relative effects and how they interact, it is possible to construct models which can describe the entire fuel cell system accurately. It is through development

of such sophisticated models the fuel cell can be optimised both in respect of high performance and high tolerance of impurities.

Electrochemical impedance spectroscopy (EIS) is the experimental tool that is used here to investigate the system *in situ* [36, 33, 32, 27, 19]. To be able to separate the anode and the cathode without using a reference electrode, we used a symmetric cell with the same gas fed to both sides of the fuel cell.

In Chapter 2 we study the symmetric hydrogen fuel cell by EIS. The combination of a low frequency range and a low operating temperature do that we find that the rate-limiting step at the lowest frequencies is an adsorption/diffusion process that gives us the Gerischer element in the equivalent circuit. This shows that the porous carbon matrix plays an important part in the hydrogen reduction reaction. The equivalent circuit is derived theoretically by using irreversible thermodynamics. We shall use this to postulate a similar step in the cathode.

In Chapter 3 we study the symmetric hydrogen cell by EIS and find a third rate-limiting step at the high frequencies. We assign this to the hydration of protons at the platinum catalyst surface. We give the equivalent circuit for all three steps (proton hydration, charge transfer and adsorption/diffusion) using the electrode reactions and irreversible thermodynamics.

In Chapter 4 the anode is investigated when the hydrogen gas contains 103 ppm of CO. EIS is used to analyse losses when the fuel is contaminated. We use the earlier developed equivalent circuit with the three rate-limiting steps and analyse the different losses and find that the experiments support this model. We see that the CO has a big influence of the charge transfer step.

In Chapter 5 the oxygen electrode is investigated and the anodic branch of the Butler-Volmer equation for the ORR is discovered. The experimental data are fitted to the Butler-Volmer equation and the transfer factor and exchange current density for the ORR is obtained. We assume from the results and earlier experience that there are two rate limiting steps, the peroxide formation and the proton dehydration.

Each chapter has been written as independent parts and are published in or submitted to scientific journals.

Chapter 2

A Gerischer phase element in the impedance diagram of the polymer electrolyte membrane fuel cell anode

Anne-Kristine Meland, Dick Bedeaux and Signe Kjelstrup

Department of Chemistry
Norwegian University of Science and Technology
N-7491 Trondheim, Norway

This paper has been published
J. Phys. Chem. B, 109 (45), 21380-21388, 2005

Abstract

We study the isothermal hydrogen adsorption and reaction at the E-TEK electrode of a polymer electrolyte fuel cell with a Nafion 117 membrane by impedance spectroscopy at 30°C. We find that the impedance diagram must include a Gerischer phase element. Constant phase elements are not sufficient to describe the experimental data. This means that an adsorption reaction takes place in combination with surface diffusion of hydrogen in the carbon layer located before the platinum surface, separate from the charge transfer step at the platinum particle surface. We are not able to distinguish between molecular or atomic hydrogen diffusion on carbon. We predict and find that the relaxation time of the adsorption step is independent of the applied potential. Water may also enter rate-limiting steps in the electrode reaction, but its role needs further clarification.

2.1 Introduction

Electrochemical impedance spectroscopy (EIS) is an experimental technique that can separate phenomena with different relaxation times, and is thus useful for determination of rate-limiting steps at electrode surfaces [37]. It has been widely used, also in studies of rather complicated three-phase contacts [29, 38]. Such contacts are typical for fuel cell electrodes.

Most polymer fuel cell electrodes consist of a porous matrix of carbon black that allow gas diffusion up to the catalyst (Pt) particles. The carbon layer is up to a few hundred micrometre thick [39]. The gas will eventually react at the catalyst, which is also in contact with the proton-conducting membrane electrolyte. This contact is often enhanced by adding membrane polymer solution to the catalyst layer, as described for instance in the Experimental section. A complicating factor is the required presence of water in the membrane [29, 40].

Impedance studies on fuel cells have mostly concerned rate limiting processes in the complete cell [29, 36, 41]. The cathode, or the oxygen electrode, will then dominate the spectrum. We shall study the anode of the fuel cell; the hydrogen electrode in a cell with two identical hydrogen electrodes. Recent impedance studies of this electrode have been motivated by the need to understand the CO tolerance of this electrode [30, 31]. As a background for such studies, it is important to have a good understanding of the elementary steps concerning hydrogen alone. Also, with the present discussion on the mode of hydrogen

adsorption in carbon nanotubes [42], it is interesting to see if impedance studies can give information on the role of carbon in the anode reaction.

The aim of the present investigation is to give experimental and theoretical support to the first step in the anode reaction. We shall see that this must include a reversible reaction (the adsorption reaction) followed by diffusion of the adsorbed species to the site where the charge transfer takes place. The adsorption reaction takes place in a layer of a thickness estimated to be 200 μm, located around the Pt particles. Such an adsorption reaction has earlier been allocated to the Pt particle itself; see, for example, the work of Chen and Kucernak [43] who studied insulated Pt particles.

Various methods have been used to establish a theoretical background for the impedance of a porous electrode. The porous electrode model, e.g. Weber and Newman [44] consists of a network of normal and charge transfer resistors. Taylor expansions around point values of non-linear equations for reaction kinetic are since long used to find the impedance [37, 36, 45]. Gomadam et al. [41] derived impedances for composite electrode models, which treat the composite electrode as a superposition of two continuous phases; one phase is a pure ion conductor, and the other phase is a pure electronic conductor. The fractal structure of these materials can also explain the typically depressed semicircles [46].

Pugazhendi et al. [38] divided the heterogeneous region into bulk parts and surfaces, and treated the surface as a two-dimensional system according to Gibbs [47], with surface properties integrated out to give excess variables. The excess energy dissipation at the electrode (or the excess entropy production) of the surface was used in the derivation of the surface impedance. We shall use this method, which is always in agreement with the second law of thermodynamics.

The aim of the study is then, from a chosen model, to first predict an impedance spectrum of the anode. We shall next use the obtained relations, to obtain properties of the electrode from experimental results. We shall see that the experiments give support to a reaction-diffusion step as the first steps in the electrode reaction. We report findings for a common membrane electrode assembly, namely the E-TEK electrode with 0.5 mg Pt/cm^2 and a Nafion 117 membrane. It is common to assume that the rate-limiting process in the electrode backing of the anode (as well as the cathode) is diffusion in the gas phase [29, 30, 36]. The good fit of the data that we obtain to a Gerischer phase element, indicates that the reversible adsorption reaction of hydrogen to carbon black along the pore walls and the subsequent diffusion along the surface to the

catalyst plays a more important role than assumed previously. Gerischer phase elements have been observed for porous electrodes before, but only in the solid oxide fuel cell [48, 49]. The results do not discriminate between molecular or atomic adsorbed hydrogen.

The paper is organised as follows. We derive the impedance of the hydrogen electrode using a two-layer model in sections 2.2 and 2.3. The first layer is that of the porous carbon layer supporting the catalyst particles, the so-called adsorption-diffusion layer. The next layer is the surface layer of the catalyst, where the charge transfer reaction takes place. The experiments and the results, that confirm this model, are described in section 2.4 and 2.5 and discussed in section 2.6.

2.2 The electrode reactions

Our theoretical model uses that only a small part of the platinum particle has an interface with the gas in the pores, so that only a few active sites are accessible directly from the gas. To reach most of the active sites on the Pt surface, the hydrogen molecules must first adsorb to one of the surfaces involved (the gas-carbon, the gas-membrane or the gas-Pt surface), and then move to the rest of the Pt surface by diffusion along the mentioned surfaces. They arrive at the active sites after passing some three phase contact lines. Hydrogen molecules cannot go *directly* to the contact line from the gas phase. This would lead to an infinite velocity of the gas close to the contact line, which is impossible. Early adsorption on a surface is therefore crucial for the hydrogen to reach most of the active sites on the Pt surface. As the area of the Pt surface that is accessible to the gas is only a fraction of the porous carbon surface, we have assumed that the absorption/desorption on the walls of the pores is the dominant process in our description. As we shall document this process is (relatively) slow.

In our model we assume that hydrogen gas is absorbed continuously along the pores in the carbon matrix:

$$\frac{1}{2}\mathrm{H_2(g)} \rightarrow \frac{1}{2}\mathrm{H_2(a)} \qquad \text{(ad-1)}$$

The adsorption reaction is labelled "ad", and a refers to the anode. Hydrogen proceeds to diffuse along the pore surface to the platinum catalyst, located between the porous carbon matrix and the cation exchange membrane. During the diffusion process some of the hydrogen desorbs to form molecular hydrogen in the gas phase again. This reversibility in the adsorption/desorption reaction

is characteristic of a system that leads to a Gerischer impedance. The reaction for chemisorption

$$\frac{1}{2}\mathrm{H_2(g)} \rightarrow \mathrm{H(a)} \tag{ad-2}$$

will lead to the same type impedance.

Most reports assume physisorbed gas molecules, so we proceed with model (ad-1) and assume that the adsorption has first order reaction kinetics in both directions:

$$r(x,t) = \frac{1}{2}k^{\mathrm{a}}_{\mathrm{H_2}}c^{\mathrm{g}}_{\mathrm{H_2}} - \frac{1}{2}k^{\mathrm{d}}_{\mathrm{H_2}}c^{\mathrm{a}}_{\mathrm{H_2}}\,(x,t) \tag{2.1}$$

We use a course-grained description in which both concentrations are given in $\mathrm{mol/m^3}$. The concentration $c^{\mathrm{g}}_{\mathrm{H_2}}$ is the gas concentration in the pores times the porosity of the carbon layer. The course-grained concentration $c^{\mathrm{a}}_{\mathrm{H_2}}$ is the surface excess concentration in $\mathrm{mol/m^2}$ times the surface area of the pores per unit of volume in $\mathrm{m^{-1}}$. The constants $k^{\mathrm{a}}_{\mathrm{H_2}}$ and $k^{\mathrm{d}}_{\mathrm{H_2}}$ are rate constants of the reaction. The reaction

$$\frac{1}{2}\mathrm{H_2(a)} \rightarrow \mathrm{H(s)} \tag{ad-3}$$

takes place at the metal surface, denoted s, see e.g. Chen and Kucernak [43], if not before, cf. Eq. (ad-2). In the Volmer mechanism, the surface atom in active sites on the surface of the platinum dissociates into protons in the membrane and electrons in the electronically conducting carbon matrix:

$$\mathrm{H(s)} \rightarrow \mathrm{H^+(m) + e^-(a)} \tag{ct}$$

The charge transfer reaction is labelled ct. A recent discussion of the relevant sites on Pt, that are active in the reaction, is given by Chen and Kucernak [43].

In summary, we have a model where adsorption takes place in a reaction-diffusion layer located before the catalyst surface, while charge transfer takes place at the metal particle surface, i.e. at the catalyst surface. The thickness of the carbon matrix in the experiment is in the order of 0.2 mm, while the thickness of the catalyst layer is in the order of 0.01 mm. In the theory given below we use a continuous model for the carbon matrix while it is sufficient to use a sharp interface for the catalyst layer, see Kjelstrup et al.[45] for further explanations.

The reaction Gibbs energy of the adsorption reaction is:

$$\Delta_r G^{\mathrm{s}}_{\mathrm{ad}}(x,t) = \frac{1}{2}\left(\mu^{\mathrm{a}}_{\mathrm{H_2}}(x,t) - \mu^{\mathrm{g}}_{\mathrm{H_2}}\right) \tag{2.2}$$

We assume equilibrium in the reaction (ad-3), giving the relation $2\mu^{\mathrm{s}}_{\mathrm{H}} = \mu^{\mathrm{a}}_{\mathrm{H_2}}(x=0)$ between the chemical potential of hydrogen just before the surface and the chemical potential of atoms at the surface. Here $x=0$ indicates the position of the catalyst surface. The hydrogen gas in the experiment has a constant (independent of position and time) pressure, leading to a constant $\mu^{\mathrm{g}}_{\mathrm{H_2}}$. The bulk anode is located at $x<0$ and the membrane at $x>0$. In our coarse grained description, transport takes place along a coordinate normal to the surface of the membrane. All variables are then independent of coordinates parallel to the surface.

In order to describe the electrochemical processes at the surface, we need the change in Gibbs energy at the surface, due to the neutral species:

$$\Delta_n G^{\mathrm{s}}_{\mathrm{ct}}(t) = -\mu^{\mathrm{s}}_{\mathrm{H}}(t) \equiv -\frac{1}{2}\mu^{\mathrm{a}}_{\mathrm{H_2}}(x=0,t) \tag{2.3}$$

For the total electrode reaction, we then have

$$\Delta_n G^{\mathrm{s}} = \Delta_r G^{\mathrm{s}}_{\mathrm{ad}}(x=0,t) + \Delta_n G^{\mathrm{s}}_{\mathrm{ct}}(t) = -\frac{1}{2}\mu^{\mathrm{g}}_{\mathrm{H_2}} \tag{2.4}$$

We can take the catalyst surface to be electro-neutral, by choosing its thickness such that the adsorptions (in $\mathrm{mol/m^2}$) of protons, $\Gamma_{\mathrm{H^+}}$, and of electrons, $\Gamma_{\mathrm{e^-}}$ are equal. Each excess proton near the metal surface therefore forms a dipole with an excess electron in the metal surface. We define the adsorption of the dipoles by:

$$\Gamma_{\mathrm{p}}(t) \equiv \Gamma_{\mathrm{H^+}}(t) \tag{2.5}$$

The chemical potential of the dipoles formed by adsorbed proton-electron pairs at the catalyst is given by Bedeaux and Kjelstrup [50]:

$$\mu^{\mathrm{s}}_{\mathrm{p}}(t) \equiv \mu^{\mathrm{s}}_{\mathrm{H^+}}(t) + \mu^{\mathrm{s}}_{\mathrm{e^-}}(t) = \mu^{\mathrm{m}}_{\mathrm{H^+}}(x=0,t) + \mu^{\mathrm{a}}_{\mathrm{e^-}}(x=0,t) \tag{2.6}$$

A superscript m indicates a property of the membrane. The chemical potential of the dipoles is

$$\mu^{\mathrm{s}}_{\mathrm{p}} = \mu^{\mathrm{s},0}_{\mathrm{p}} + 2RT\ln\left(\gamma^{\mathrm{s}}_{\mathrm{p}}\Gamma_{\mathrm{p}}/\Gamma^{0}_{\mathrm{p}}\right) \tag{2.7}$$

where Γ^0_{p} is the standard excess concentration of adsorbed dipoles, $\gamma^{\mathrm{s}}_{\mathrm{p}}$ is the activity coefficient and $\mu^{\mathrm{s},0}_{\mathrm{p}}$ is the standard chemical potential.

One often refers to the layer in front of the metal surface containing the protons as the double layer and the excess electron density of the metal surface as the charge density of the surface. Our description above clarifies that these

two layers in combination are electroneutral and form a dipole layer. The polarisation P^{s} we find, cf. Eqs. (2.9) and (2.11), is nothing else than the polarisation due to the double layer and $c_{\mathrm{p}}^{\mathrm{s}}$ used in Eq. (2.11) is the capacitance of the double layer.

The charge transfer reaction (ct) increases the number of adsorbed dipoles while the electric current j decreases it, therefore

$$\frac{d}{dt}\Gamma_{\mathrm{p}} = r_{\mathrm{ct}}^{\mathrm{s}} - \frac{j}{F} \tag{2.8}$$

where $r_{\mathrm{ct}}^{\mathrm{s}}$ refers to the reaction rate, and F is Faraday's constant. The surface polarisation in the direction normal to the surface is equal to the dipole concentration times Faraday's constant, F, times the average distance, d_{s}, between the charges

$$P^{\mathrm{s}} = d_{\mathrm{s}} F \Gamma_{\mathrm{p}} \tag{2.9}$$

With a constant d_{s} it follows that the surface polarisation and the adsorption of dipoles depend on each other. By eliminating Γ_{p} from Eq. (2.8), we obtain

$$r_{\mathrm{ct}}^{\mathrm{s}} = \frac{1}{F}\left(j + \frac{1}{d_{\mathrm{s}}}\frac{d}{dt}P^{\mathrm{s}}\right) \tag{2.10}$$

The surface polarisation divided by the surface thickness gives the surface potential difference times the capacitance of the dipole layer, c_{p}

$$\frac{P^{\mathrm{s}}}{d_{\mathrm{s}}} = F\Gamma_{\mathrm{p}} = c_{\mathrm{p}}^{\mathrm{s}}\Delta_{\mathrm{s}}\phi \tag{2.11}$$

It is common to assume that there is equilibrium for water across the pore channel, across the catalyst surface and into the membrane. We shall also use this assumption in our first calculation.

2.3 The electrode impedance

2.3.1 The variables in the oscillating field

Impedances are measured as a function of the frequency ω of the alternating potential, in the presence of a constant applied potential. The cell under investigation is symmetric, so we consider the potential difference between the anode and the centre of the membrane:

$$\Delta\phi = \Delta\phi_{\mathrm{dc}} + \Delta\phi_{\mathrm{ac}}\exp(i\omega t) \tag{2.12}$$

The potential difference between the centre of the membrane and the cathode is the same. We can disregard the contribution to the emf of the two hydrogen electrodes. They are equal and opposite, and in the total cell potential they cancel each other. Each contribution is then the sum of the potential difference across one surface and half the membrane:

$$\Delta\phi_{\rm dc} = \Delta_{\rm s}\phi_{\rm dc} + \frac{1}{2}\Delta_{\rm m}\phi_{\rm dc} \quad \text{and} \quad \Delta\phi_{\rm ac} = \Delta_{\rm s}\phi_{\rm ac} + \frac{1}{2}\Delta_{\rm m}\phi_{\rm ac} \tag{2.13}$$

The electric current similarly has a dc and an ac contribution

$$j = j_{\rm dc} + j_{\rm ac}\exp(i\omega t) \tag{2.14}$$

In the membrane, which conducts by protons, one has

$$\Delta_{\rm m}\phi_{\rm dc} = r_{\rm m} j_{\rm dc} \quad \text{and} \quad \Delta_{\rm m}\phi_{\rm ac} = r_{\rm m} j_{\rm ac} \tag{2.15}$$

The corresponding relations for the potential differences across the surface is derived below.

The surface polarisation can also be written as the sum of a stationary and an oscillating contribution

$$P^{\rm s} = P^{\rm s}_{\rm dc} + P^{\rm s}_{\rm ac}\exp(i\omega t) \tag{2.16}$$

For the dc and the ac contributions to $r^{\rm s}_{\rm ct}$ this gives, using Eq. (2.10),

$$r^{\rm s}_{\rm ct,dc} = \frac{1}{F} j_{\rm dc} \quad \text{and} \quad r^{\rm s}_{\rm ct,ac} = \frac{1}{F}\left(j_{\rm ac} + \frac{i\omega P^{\rm s}_{\rm ac}}{d_{\rm s}}\right) \tag{2.17}$$

2.3.2 The adsorption-diffusion layer in front of the catalyst

The time dependence of the concentration of hydrogen at position x in the anode is given by

$$\frac{\partial c^{\rm a}_{\rm H_2}(x,t)}{\partial t} = -\frac{\partial J^{\rm a}_{\rm H_2}(x,t)}{\partial x} + \frac{1}{2}k^{\rm a}_{\rm H_2} c^{\rm g}_{\rm H_2} - \frac{1}{2}k^{\rm d}_{\rm H_2} c^{\rm a}_{\rm H_2}(x,t) \tag{2.18}$$

where

$$J^{\rm a}_{\rm H_2}(x,t) = -D^{\rm a}_{\rm H_2}\frac{\partial c^{\rm a}_{\rm H_2}(x,t)}{\partial x} \tag{2.19}$$

is the coarse grained diffusion flux (in mol/m^{2}s) of molecular hydrogen along the surface of the pores in the carbon matrix to the catalyst surface at $x = 0$ and $D^{\rm a}_{\rm H_2}$ is the diffusion constant (in m^2/s). Equilibrium in the adsorption

reaction gives, using Eq. (2.1), the equilibrium concentration of adsorbed hydrogen

$$c^{\mathrm{a}}_{\mathrm{H}_2,eq} = c^{\mathrm{g}}_{\mathrm{H}_2} \frac{k^{\mathrm{a}}_{\mathrm{H}_2}}{k^{\mathrm{d}}_{\mathrm{H}_2}} \tag{2.20}$$

The rate coefficients may depend on the state of the surface, whether it is polarised or not, and on the pressure. The constant hydrogen pressure in the pore gives a constant gas concentration, $c^{\mathrm{a}}_{\mathrm{H}_2}$ and therefore also a constant value for $c^{\mathrm{a}}_{\mathrm{H}_2,eq}$. We use linear kinetics for the adsorption-desorption reaction. As we will discuss in section 2.6.3 the absorption of hydrogen is well below saturation, so that linear kinetics is appropriate for this reaction. We introduce the deviation from the equilibrium concentration

$$c^{\mathrm{a}}_{\mathrm{H}_2}(x,t) \equiv c^{\mathrm{a}}_{\mathrm{H}_2,eq} + \delta c^{\mathrm{a}}_{\mathrm{H}_2}(x,t) \tag{2.21}$$

Equation 2.18 then becomes for $\delta c^{\mathrm{a}}_{\mathrm{H}_2}$

$$\frac{\partial \delta c^{\mathrm{a}}_{\mathrm{H}_2}(x,t)}{\partial t} = D^{\mathrm{a}}_{\mathrm{H}_2} \frac{\partial^2 \delta c^{\mathrm{a}}_{\mathrm{H}_2}(x)}{\partial x^2} - \frac{1}{2} k^{\mathrm{d}}_{\mathrm{H}_2} \delta c^{\mathrm{a}}_{\mathrm{H}_2}(x,t) \tag{2.22}$$

For a dc electric current Eq. (2.22) reduces to

$$0 = D^{\mathrm{a}}_{\mathrm{H}_2} \frac{\partial^2 \delta c^{\mathrm{a}}_{\mathrm{H}_2,\mathrm{dc}}(x)}{\partial x^2} - \frac{1}{2} k^{\mathrm{d}}_{\mathrm{H}_2} \delta c^{\mathrm{a}}_{\mathrm{H}_2,\mathrm{dc}}(x) \tag{2.23}$$

The solution is given by

$$\delta c^{\mathrm{a}}_{\mathrm{H}_2,\mathrm{dc}}(x) = -\frac{j_{\mathrm{dc}}}{F\sqrt{2D^{\mathrm{a}}_{\mathrm{H}_2} k^{\mathrm{d}}_{\mathrm{H}_2}}} \exp\left(x\sqrt{\frac{k^{\mathrm{d}}_{\mathrm{H}_2}}{2D^{\mathrm{a}}_{\mathrm{H}_2}}}\right) \tag{2.24}$$

where we used

$$2J^{\mathrm{a}}_{\mathrm{H}_2}(x=0) = r^{\mathrm{s}}_{\mathrm{ct,dc}} = r^{\mathrm{s}}_{\mathrm{ad,dc}} = j_{\mathrm{dc}}/F \tag{2.25}$$

We see from Eq. (2.24) that $\delta c^{\mathrm{a}}_{\mathrm{H}_2,dc}$ is negative when $j_{\mathrm{dc}} > 0$ and positive when $j_{\mathrm{dc}} < 0$.

When the thickness d of the carbon layer is smaller than $\sqrt{2D^{\mathrm{a}}_{\mathrm{H}_2}/k^{\mathrm{d}}_{\mathrm{H}_2}}$ one should use that the diffusion flux in $x = -d$ is zero. One must then replace $\exp\left[x\sqrt{k^{\mathrm{d}}_{\mathrm{H}_2}/2D^{\mathrm{a}}_{\mathrm{H}_2}}\right]$ by
$\cosh\left[(x+d)\sqrt{k^{\mathrm{d}}_{\mathrm{H}_2}/2D^{\mathrm{a}}_{\mathrm{H}_2}}\right] / \cosh\left[d\sqrt{k^{\mathrm{d}}_{\mathrm{H}_2}/2D^{\mathrm{a}}_{\mathrm{H}_2}}\right]$ in Eqs. (2.24) and (2.29)

and make a similar replacement in Eqs. (2.32) and (2.34). This implies that the mass transport at low frequencies will be reduced compared to the expressions given. The further analysis is not affected.

We use

$$\begin{aligned}\mu^{\mathrm{a}}_{\mathrm{H}_2}(x,t) &= \mu^{\mathrm{a},0}_{\mathrm{H}_2} + RT\ln\left(\frac{c^{\mathrm{a}}_{\mathrm{H}_2}(x,t)}{c^{\mathrm{a},0}_{\mathrm{H}_2}}\right)\\ &= \mu^{\mathrm{a},0}_{\mathrm{H}_2} + RT\ln\left(\frac{c^{\mathrm{a}}_{\mathrm{H}_2,eq}}{c^{\mathrm{a},0}_{\mathrm{H}_2}}\right) + RT\ln\left(\frac{c^{\mathrm{a}}_{\mathrm{H}_2}(x,t)}{c^{\mathrm{a}}_{\mathrm{H}_2,eq}}\right)\\ &= \mu^{\mathrm{a}}_{\mathrm{H}_2,eq} + RT\ln\left(\frac{c^{\mathrm{a}}_{\mathrm{H}_2}(x,t)}{c^{\mathrm{a}}_{\mathrm{H}_2,eq}}\right) \qquad (2.26)\end{aligned}$$

for the chemical potential of hydrogen, where $\mu^{\mathrm{a},0}_{\mathrm{H}_2}$ and $c^{\mathrm{a},0}_{\mathrm{H}_2}$ are standard values. To linear order in $\delta c^{\mathrm{a}}_{\mathrm{H}}$ this gives

$$\mu^{\mathrm{a}}_{\mathrm{H}_2}(x,t) = \mu^{\mathrm{a}}_{\mathrm{H}_2,eq} + RT\ln\left(1+\frac{\delta c^{\mathrm{a}}_{\mathrm{H}_2}(x,t)}{c^{\mathrm{a}}_{\mathrm{H}_2,eq}}\right) \qquad (2.27)$$

$$= \mu^{\mathrm{a}}_{\mathrm{H}_2,eq} + RT\frac{\delta c^{\mathrm{a}}_{\mathrm{H}_2}(x,t)}{c^{\mathrm{a}}_{\mathrm{H}_2,eq}} \qquad (2.28)$$

By introducing Eq. (2.24) we obtain

$$\mu^{\mathrm{a}}_{\mathrm{H}_2,dc}(x) = \mu^{\mathrm{a}}_{\mathrm{H}_2,eq} - \frac{j_{\mathrm{dc}}RT}{Fc^{\mathrm{a}}_{\mathrm{H}_2,eq}\sqrt{2D^{\mathrm{a}}_{\mathrm{H}_2}k^{\mathrm{d}}_{\mathrm{H}_2}}}\exp\left(x\sqrt{\frac{k^{\mathrm{d}}_{\mathrm{H}_2}}{2D^{\mathrm{a}}_{\mathrm{H}_2}}}\right) \qquad (2.29)$$

The total Gibbs energy change over the whole layer becomes

$$\begin{aligned}\Delta_r G_{\mathrm{ad,dc}} &= \mu^{\mathrm{s}}_{\mathrm{H,dc}} - \frac{1}{2}\mu^{\mathrm{g}}_{\mathrm{H}_2}\\ &= \frac{1}{2}\left[\mu^{\mathrm{a}}_{\mathrm{H}_2,dc}(x=0) - \mu^{\mathrm{a}}_{\mathrm{H}_2,dc}(x=-\infty)\right]\\ &= -\frac{j_{\mathrm{dc}}RT}{2Fc^{\mathrm{a}}_{\mathrm{H}_2,eq}\sqrt{2D^{\mathrm{a}}_{\mathrm{H}_2}k^{\mathrm{d}}_{\mathrm{H}_2}}} \qquad (2.30)\end{aligned}$$

$\Delta_r G_{\mathrm{ad,dc}}$ gives a contribution to the surface potential drop via $\delta\mu^{\mathrm{a}}_{\mathrm{H}_2,\mathrm{dc}}(x=0)$.

The ac contribution to $c^{\mathrm{a}}_{\mathrm{H}_2}(x,t)$ is also small. Eq. (2.22) together with Eq. (2.19) therefore reduces to

$$i\omega\delta c^{\mathrm{a}}_{\mathrm{H}_2,\mathrm{ac}}(x) = D^{\mathrm{a}}_{\mathrm{H}_2}\frac{\partial^2\delta c^{\mathrm{a}}_{\mathrm{H}_2,\mathrm{ac}}(x)}{\partial x^2} - \frac{1}{2}k^{\mathrm{d}}_{\mathrm{H}_2}\delta c^{\mathrm{a}}_{\mathrm{H}_2,\mathrm{ac}}(x) \tag{2.31}$$

The solution to Eq. (2.31) becomes

$$\delta c^{\mathrm{a}}_{\mathrm{H}_2,\mathrm{ac}}(x) = -A\exp\left[\, x\sqrt{\frac{k^{\mathrm{d}}_{\mathrm{H}_2}}{2D^{\mathrm{a}}_{\mathrm{H}_2}}(1+i\omega\tau_{\mathrm{ad}})}\,\right] \tag{2.32}$$

where the relaxation time in the adsorption is

$$\tau_{\mathrm{ad}} = \frac{2}{k^{\mathrm{d}}_{\mathrm{H}_2}} = \frac{2c^{\mathrm{a}}_{\mathrm{H}_2,eq}}{k^{\mathrm{a}}_{\mathrm{H}_2}c^{\mathrm{g}}_{\mathrm{H}_2}} \tag{2.33}$$

We used Eq. (2.20) in the last equality. The constant A in Eq. (2.32) must be determined from the boundary condition in $x = 0$. The resulting contribution to the chemical potential, cf. Eq. (2.28), due to the ac current is

$$\begin{aligned}\mu^{\mathrm{a}}_{\mathrm{H}_2,\mathrm{ac}}(x) &= RT\delta c^{\mathrm{a}}_{\mathrm{H}_2,\mathrm{ac}}(x)/c^{\mathrm{a}}_{\mathrm{H}_2,eq}\\ &= -\frac{ART}{c^{\mathrm{a}}_{\mathrm{H}_2,eq}}\exp\left[x\sqrt{\frac{k^{\mathrm{d}}_{\mathrm{H}_2}}{2D^{\mathrm{a}}_{\mathrm{H}_2}}(1+i\omega\tau_{\mathrm{ad}})}\right]\end{aligned} \tag{2.34}$$

The contribution due to a small dc current has already been given as the second term on the right hand side of Eq. (2.29).

The total amount of adsorbed hydrogen molecules on the pore surface due to the ac current, is

$$n^{\mathrm{a}}_{\mathrm{H}_2,\mathrm{ac}} = \int_{-\infty}^{0}\delta c^{\mathrm{a}}_{\mathrm{H}_2,\mathrm{ac}}(x)\,dx = -A\sqrt{\frac{2D^{\mathrm{a}}_{\mathrm{H}_2}}{k^{\mathrm{d}}_{\mathrm{H}_2}(1+i\omega\tau_{\mathrm{ad}})}} \tag{2.35}$$

The ac contribution to the reaction rate for the adsorption reaction is then given by

$$r^{\mathrm{s}}_{\mathrm{ad},\mathrm{ac}} = -k^{\mathrm{d}}_{\mathrm{H}_2}\int_{-\infty}^{0}\delta c^{\mathrm{a}}_{\mathrm{H}_2,\mathrm{ac}}(x)\,dx = -k^{\mathrm{d}}_{\mathrm{H}_2}n^{\mathrm{a}}_{\mathrm{H}_2,\mathrm{ac}} = A\sqrt{\frac{2D^{\mathrm{a}}_{\mathrm{H}_2}k^{\mathrm{d}}_{\mathrm{H}_2}}{1+i\omega\tau_{\mathrm{ad}}}} \tag{2.36}$$

The corresponding reaction rate for the charge transfer reaction is given by

$$\begin{aligned}r^{\mathrm{s}}_{\mathrm{ct},\mathrm{ac}} = 2J^{\mathrm{a}}_{\mathrm{H}_2}(x=0) &= A\sqrt{2D^{\mathrm{a}}_{\mathrm{H}_2}k^{\mathrm{d}}_{\mathrm{H}_2}(1+i\omega\tau_{\mathrm{ad}})}\\ &= (1+i\omega\tau_{\mathrm{ad}})r^{\mathrm{s,a}}_{\mathrm{ad},\mathrm{ac}}\end{aligned} \tag{2.37}$$

The ac contribution to the reaction Gibbs energy of the adsorption is

$$\begin{aligned}\Delta_r G_{\mathrm{ad,ac}} &= \frac{1}{2}(\mu^{\mathrm{a}}_{\mathrm{H_2,ac}}(x=0) - \mu^{\mathrm{g}}_{\mathrm{H_2,ac}}) \\ &= \frac{1}{2}\mu^{\mathrm{a}}{}_{\mathrm{H_2,ac}}\,(x=0) = -\frac{ART}{2c^{\mathrm{a}}_{\mathrm{H_2},eq}}\end{aligned} \tag{2.38}$$

where we used Eq. (2.34). By eliminating A in Eq. (2.38) using Eq. 2.37 we find,

$$\Delta_r G_{\mathrm{ad,ac}} = -Z_{\mathrm{ad}} F^2 r^{\mathrm{s}}_{\mathrm{ct,ac}} \tag{2.39}$$

where

$$Z_{\mathrm{ad}} = \frac{RT}{2F^2 c^{\mathrm{a}}_{\mathrm{H_2},eq}\sqrt{2D^{\mathrm{a}}_{\mathrm{H_2}} k^{\mathrm{d}}_{\mathrm{H_2}}\,(1+i\omega\tau_{\mathrm{ad}})}} \tag{2.40}$$

With chemisorption of atomic hydrogen at the surface (reaction ad-2), the corresponding equation becomes:

$$Z_{\text{ad-2}} = \frac{RT}{F^2 c^{\mathrm{a}}_{\mathrm{H},eq}\sqrt{2D^{\mathrm{a}}_{\mathrm{H}} k^{\mathrm{d}}_{\mathrm{H}} c^{\mathrm{a}}_{\mathrm{H},eq}\,(1+i\omega\tau_{\mathrm{ad}})}} \tag{2.41}$$

where the diffusion coefficient, the reaction coefficients and the equilibrium concentration at the surface now refer to atomic hydrogen, cf. Eq. (ad-2). These are impedances of a Gerischer element, and we shall see that experimental results for the hydrogen electrode of the fuel cell fit well to such an element, while e.g. a Warburg element or other elements can only be fitted with larger inaccuracies or do not describe the measurements at all. The expressions show that the impedance becomes smaller as the equilibrium adsorption of the hydrogen to the pore surface in the carbon matrix becomes larger. The two impedances differ in their dependence on this concentration.

2.3.3 The charge transfer reaction at the catalyst surface

Consider next the catalyst surface, or the interface between the membrane and the adsorption-diffusion layer in the electrode. The excess entropy production rate of this surface, $\sigma^{\mathrm{s}}_{\mathrm{ct}}$, contains the information about the surface dynamics. For isothermal conditions, the contribution due to the alternating field is [50]:

$$T\sigma^{\mathrm{s}}_{\mathrm{ct,ac}} = -j_{\mathrm{ac}}\Delta_{\mathrm{s}}\phi_{\mathrm{ac}} + i\omega P^{\mathrm{s}}_{\mathrm{ct,ac}}\left(\frac{D - D^{\mathrm{s}}_{eq}}{\varepsilon_0}\right)_{\mathrm{ac}} - r^{\mathrm{s}}_{\mathrm{ct,ac}}\Delta_n G^{\mathrm{s}}_{\mathrm{ct,ac}} \tag{2.42}$$

The D in this equation is the displacement field and ε_0 is the dielectric constant of vacuum. The equilibrium displacement field is zero for free charges, $D^{\mathrm{s}}_{eq} = 0$.

The displacement field is given by $D = -\varepsilon_0 \Delta_s \phi_{ac}/d_s$. Using Eq. (2.17) for the ac contribution one obtains

$$T\sigma^s_{ct,ac} = -r^s_{ct,ac}\left(\Delta_n G^s_{ct,ac} + F\Delta_s\phi_{ac}\right) \tag{2.43}$$

The theory of non-equilibrium thermodynamics prescribes that the force and the flux are related by

$$\Delta_s\phi_{ac} + \frac{\Delta_n G^s_{ct,ac}}{F} = -\rho^s_{ct} F r^s_{ct,ac} \tag{2.44}$$

where ρ^s_{ct} is the resistivity of the charge transfer reaction. The electrochemical reaction rate is normally not related to its driving force by a linear relation. In this experiment, the alternating contribution to the forces are small (± 5 mV), however, so that we can use a linear theory. Also, it is likely that the combination of the two terms on the right hand side of Eq. (2.43) is smaller in absolute value than one of the terms. The adsorption-diffusion layer has an impact on $\Delta_s\phi_{ac}$, through the chemical potential of hydrogen atoms at position $x = 0$. The resistivity is independent of the driving force, but can depend on the temperature and the polarisation induced by the dc-field.

The dc contribution to the excess entropy production rate is found using $\omega = 0$ and $j_{dc} = F r^s_{ct,dc}$. This gives

$$T\sigma^s_{ct,dc} = -j_{dc}\left(\Delta_s\phi_{dc} + \frac{\Delta_n G^s_{ct,dc}}{F}\right) \tag{2.45}$$

For small dc-currents the linear law is thus:

$$\Delta_s\phi_{dc} + \frac{\Delta_n G^s_{ct,dc}}{F} = -\rho^s_{ct} F r^s_{ct,dc} = -\rho^s_{ct} j_{dc} \tag{2.46}$$

which is exactly the same relation as for the ac current, Eq. (2.44).

2.3.4 The surface impedance and surface properties

The impedance of the catalyst surface is defined as:

$$Z^s \equiv -\frac{\Delta_s\phi_{ac}}{j_{ac}} \tag{2.47}$$

We find the surface impedance by adding Eqs. (2.39) and (2.44). This gives:

$$\Delta_s\phi_{ac} + \frac{\Delta_n G^s_{ac}}{F} = \Delta_s\phi_{ac} = -\left(\rho^s_{ct} + Z_{ad}\right) F r^s_{ct,ac} \tag{2.48}$$

where we used that the chemical potential of the hydrogen gas is constant, cf. Eq. (2.4). It furthermore follows from Eqs. (2.10) and (2.11) that

$$Fr^{\mathrm{s}}_{\mathrm{ct,ac}} = j_{\mathrm{ac}} + i\omega c^{\mathrm{s}}_{\mathrm{p}} \Delta_{\mathrm{s}} \phi_{\mathrm{ac}} \tag{2.49}$$

By combining Eqs. (2.47)-(2.49), we obtain the impedance of the surface

$$Z^{\mathrm{s}} = \frac{\rho^{\mathrm{s}}_{\mathrm{ct}} + Z_{\mathrm{ad}}}{1 + i\omega c^{\mathrm{s}}_{\mathrm{p}} \left(\rho^{\mathrm{s}}_{\mathrm{ct}} + Z_{\mathrm{ad}}\right)} \tag{2.50}$$

When $\omega \to \infty$, we see that:

$$Z^{\mathrm{s}}_{\omega\to\infty} = 0 \tag{2.51}$$

In the present experiments, we measure the response of two identically made electrodes plus membrane electrolyte. When a dc current is passing the cell, one electrode will be a sink for hydrogen, while the other will be a source for hydrogen. The impedances of the two electrodes are the same, however. Both electrodes therefore give the same contribution to the measurement, also when the electrodes are polarised. In terms of the measured impedance, Z^{cell}, and the membrane impedance, Z^{mem}, the impedance of one electrode is then:

$$Z^{\mathrm{s}} = \frac{1}{2}(Z^{\mathrm{cell}} - Z^{\mathrm{mem}}) \tag{2.52}$$

The membrane impedance is found from Eq. (2.50) by taking the limit of Z^{cell} for $\omega \to \infty$. The results that are calculated for Z^{s} from Eq. (2.52), can be fitted to formula (2.50) using Eq. (2.40) for Z_{ad}.

With the heterogeneous catalyst surface one may expect a non-ideal contribution to the impedance. A constant phase element (CPE) shall thus be used, rather than a capacitance in parallel with the resistance. The CPE is defined by its impedance:

$$Z_{\mathrm{CPE}} = \frac{1}{T_{\mathrm{ct}}(i\omega)^{\alpha_{\mathrm{ct}}}} \tag{2.53}$$

The phase angle of the CPE is constant and independent of the frequency. When α_{ct}=1, T_{ct}= $c^{\mathrm{s}}_{\mathrm{p}}$. The more depressed the semi-circle is, the lower is the α-value. We define the relaxation time:

$$\tau_{\mathrm{ct}} = (T_{\mathrm{ct}\rho_{\mathrm{ct}}})^{1/\alpha_{\mathrm{ct}}} \tag{2.54}$$

The limiting behaviour $\omega \to 0$ gives:

$$Z^{\mathrm{s}}_{\omega\to 0} = Z_{\omega\to 0,\mathrm{ad}} + \rho_{\mathrm{ct}} \tag{2.55}$$

The fit of the experimental results to the theoretical expressions gave Y_0 and $\tau_{\rm ad}$ in the following expression for $Z_{\rm ad}$:

$$Z_{\rm ad} = \frac{1}{Y_0\sqrt{\tau_{\rm ad}^{-1} + i\omega}} \tag{2.56}$$

with the relaxation time, $\tau_{\rm ad} = 2/k^{\rm d}_{\rm H_2}$, see Eq. (2.33). According to model (ad-1) the relaxation time is constant. According to model (ad-2), the corresponding relaxation time depends on the square root of the hydrogen concentration in the gas phase, with $\tau_{\rm ad} = (2k_{\rm H}c_{{\rm H},eq})^{-1} = 2\sqrt{c^g_{\rm H_2}k^{\rm a}_{\rm H_2}k_{\rm H}}$. The admittance is, with adsorption of molecular hydrogen, model (ad-1):

$$Y_0 = \frac{4F^2}{RT}c^{\rm a}_{{\rm H}_2,eq}\sqrt{D^{\rm a}_{\rm H_2}} \tag{2.57}$$

and with adsorption of atomic hydrogen, model (ad-2):

$$Y_0 = \frac{F^2}{RT}c^{\rm a}_{{\rm H},eq}\sqrt{2D^{\rm a}_{\rm H}\tau_{\rm ad}k^{\rm d}_{\rm H}c^{\rm a}_{{\rm H},eq}} = \frac{F^2}{RT}c^{\rm a}_{{\rm H},eq}\sqrt{D^{\rm a}_{\rm H}} \tag{2.58}$$

We see that knowledge of the diffusion constant for the hydrogen molecule (or atom) along the pore, enables us to calculate the concentrations of the adsorbed species from the equation above. The admittance may depend on the applied potential if the kinetic constants and the adsorption depends on this parameter.

2.4 Experimental

2.4.1 The membrane-electrode assembly

The electrodes in this study were E-TEK gas diffusion electrodes (Elat/Std/DS/V2) with 0.5 mg/cm^2 Pt loading and 20% Pt/C. The electrodes were sprayed with a 5 wt% Nafion solution to give 0.6 mg/cm^2. The cell membrane and electrode assembly (MEA) consisted of two such electrodes separated by a Nafion 117 membrane. The membrane was pre-treated using a standard procedure, as described for instance by Møller-Holst [51]. The mechanical pressure over the MEA was 4.2 bar, controlled by a pneumatic cylinder. The same hydrogen pressure of 1 bar was used on the two sides.

The MEAs were tested in a test-station developed by Møller-Holst [51] and Vie [39]. The fuel cell was a circular single cell with an electrode area of 4.91

cm^2. The fuel cell housing was made of stainless steel (SS-316) and was supported by two pistons (SS-316). At the top of the pistons, there were flow fields in a serpentine pattern. The pistons also served as current collectors and thermostats. They contained heating elements inside. Thermocouples in the cell housing measured the temperature in the electrode backings. The temperatures were controlled by a PID controller (Eurotherm 2408) to $30.0 \pm 0.1^{\circ}C$. The cell voltage was measured between the pistons' tops.

Care was taken to always use new MEA preparations, as a certain ageing effect was observed if the same MEA was used for more than 30 experiments. It has been shown that, for instance, agglomeration of Pt particles take place over time when the system is under stress [52], with the important effect that the available surface area is reduced.

2.4.2 The gas humidification system

The hydrogen gas (99.999% purity from AGA) was humidified at $80^{\circ}C$ outside the cell, making sure that the gas and MEA were always saturated with water. The gases were humidified in a gas-humidifying system developed by Vie [39] before entering the fuel cell. There are two humidifiers, one for the cathode and one for the anode. The temperatures of the humidifiers were controlled independently of one another.

The dry gas entered at the top of the humidifier tank and was preheated in a heating coil. The gas was then bubbled through a glass-sieve and finely dispersed into an 800 ml internal container filled with water at a given temperature. The small internal container was placed in a larger 10 l tank also filled with water. This outer container was heated by an electrical heating tape. This ensures a stable temperature of the gas. The humidified gas left the humidifier at the top of the internal container and entered next the fuel cell system. Saturation of the gases at the given temperature can then be assumed. The humidifying temperature was always higher than the cell temperature to prevent the MEA from drying out when electric current was passing the cell. A gas flow of 20 ml per minute prevented problems with condensing water. This flow rate did not pose any limitations on the spectra observed, see however Kim et al. [31] who studied CO adsorption and found flow rate effects at low gas flow rates.

2.4.3 Impedance measurements (EIS)

The impedance of the cell described above was measured at 30°C for five different applied potentials. The applied potentials were 10, 20, 30, 50 and 60 mV. These potentials gave all the small current density required for validity of the theoretical derivations.

The impedance spectra were recorded using a PAR 263A potentiostat and a Solartron 1260 FRA. Z-plot software from Scribner Associates, Inc. was used to run the experiments. Measurements were made in a two-electrode set-up. The impedance was obtained by sweeping over the frequency range from 10 kHz to 10 mHz, recording 12 steps/decade for each constant applied potential. An amplitude of 5 mV was used. In our experience, amplitudes larger than this can make a significant change in the spectrum. This is noteworthy, since many investigations are done with an amplitude of 10 mV [30] or more. The current density that corresponded to a particular applied potential was recorded before and after the impedance measurement, to check if the cell was stable. Results were discarded if the current density changed by more than 5%.

2.4.4 Cyclic voltammetry (CV)

The reproducibility of each cell's performance was also investigated by cyclic voltammetry. Voltammograms were recorded with the PAR 263A and CorrWare software (Scribner) for the same cell as in the impedance experiments. The reference side of the system was then fed with hydrogen gas, while the working side contained nitrogen gas, also 99.999% purity (AGA). Voltammetry experiments were done before and after every series of impedance measurements. The scan rate was 50 mV/s, and the applied potential varied between 0.04 V and 1.5 V. The temperature was 30°C. One such voltammogram is shown in Fig. 2.1. It did not change by more than 5% from the start to the end of the series of EIS experiments.

We determined the integral under the curve between the boundary values 0.4 and 0.05 V, subtracting the constant basis value of 14 mC/cm^2, believed to be due to the electro-neutral layer of H(ads) [53]. The integration was done with Z-View (Scribner), giving an adsorption of protons of $Q_H(mC/cm^2$ = 23 mC/cm^2 or 2.4×10^{-7} mol/ cm^2. This charge was converted to a surface area, using as basis the adsorption of a hydrogen mono-layer on bright Pt (210 $\mu C/cm^2$ Pt [53]). For the Pt content used here (0.5 mg Pt/cm^2), the result was 22 m^2 Pt/g Pt. Ciureanu and Wang [30] found an electrochemical surface

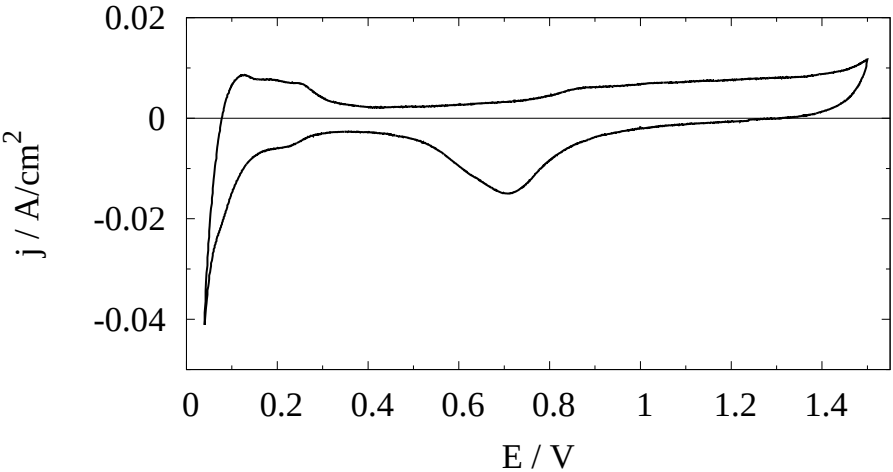

Figure 2.1. Cyclic voltammetry results for the cell in Fig. 2.2. The working electrode compartment contained pure N_2 and the scan rate was 50 mV/s

area of 14 m^2 Pt/g Pt in a similar calculation for a surface with a larger Pt loading, while Springer et al. [52] found 24 m^2 Pt/g Pt for new MEAs, similar to ours.

These tests all mean that the surface conditions did not change significantly for the series of measurements that were performed. This also mean that our MEA can be compared to similar MEAs documented in the literature, and that they therefore appear to be typical for the polymer electrolyte fuel cell anode.

2.5 Results

The EIS experiments are represented by Figs. 2.2 and 2.3 and Table 2.1. The spectra are given as Nyquist plots of Z^{cell} according to

$$Z^{\text{cell}} = Z(\text{Re})^{\text{cell}} + iZ(\text{Im})^{\text{cell}} \tag{2.59}$$

A typical EIS for a cell with unpolarised, new MEAs is shown in Fig. 2.2a, the left curve. The spectrum of a cell with an applied dc potential of 50 mV is also shown, the right curve. Fig. 2.3 shows the difference between the first and the 30'th experiments in an unpolarised cell, i.e. the ageing effect of the impedance.

The spectra were fitted as described in section 2.3.4, and the variables derived are given in Table 2.1. The variation in the variables of the spectrum with applied potential is seen in detail in this table.

Table 2.1. Fit of experimental results for the fuel cell hydrogen electrode in Fig. 2.2 according to section 2.3.4. Electrodes are E-TEK, Elat/Std/DS/V2 0.5 mg Pt/cm^2, 20 Pt/C, impregnated with 0.6 mg Nafion/cm^2 (5 wt% solution). The membrane is Nafion 117. The cell temperature is 30°C and the hydrogen pressure is 1 bar. The applied potential refers to the whole cell. The fits gave all a Nafion membrane area resistance of $0.51 \pm 0.01\ \Omega\ \text{cm}^2$ *and* $\alpha_{\text{ct}} = 0.61 \pm 0.02$

$\Delta\phi_{\text{dc}}$ (mV)	ρ_{ct} (Ω cm^2)	T_{ct} (s$^{\alpha_{\text{ct}}}/\Omega$ cm^2)	Y_0 (s$^{1/2}/\Omega$ cm^2)	τ_{ad} (s)
0	0.063±0.002	0.14±0.02	210±30	6
10	0.072±0.003	0.13±0.02	190±20	8
20	0.076±0.003	0.12±0.01	170±20	8
30	0.081±0.003	0.12±0.01	160±20	8
50	0.084±0.003	0.11±0.02	130±10	8
60	0.087±0.004	0.10±0.01	120±10	8

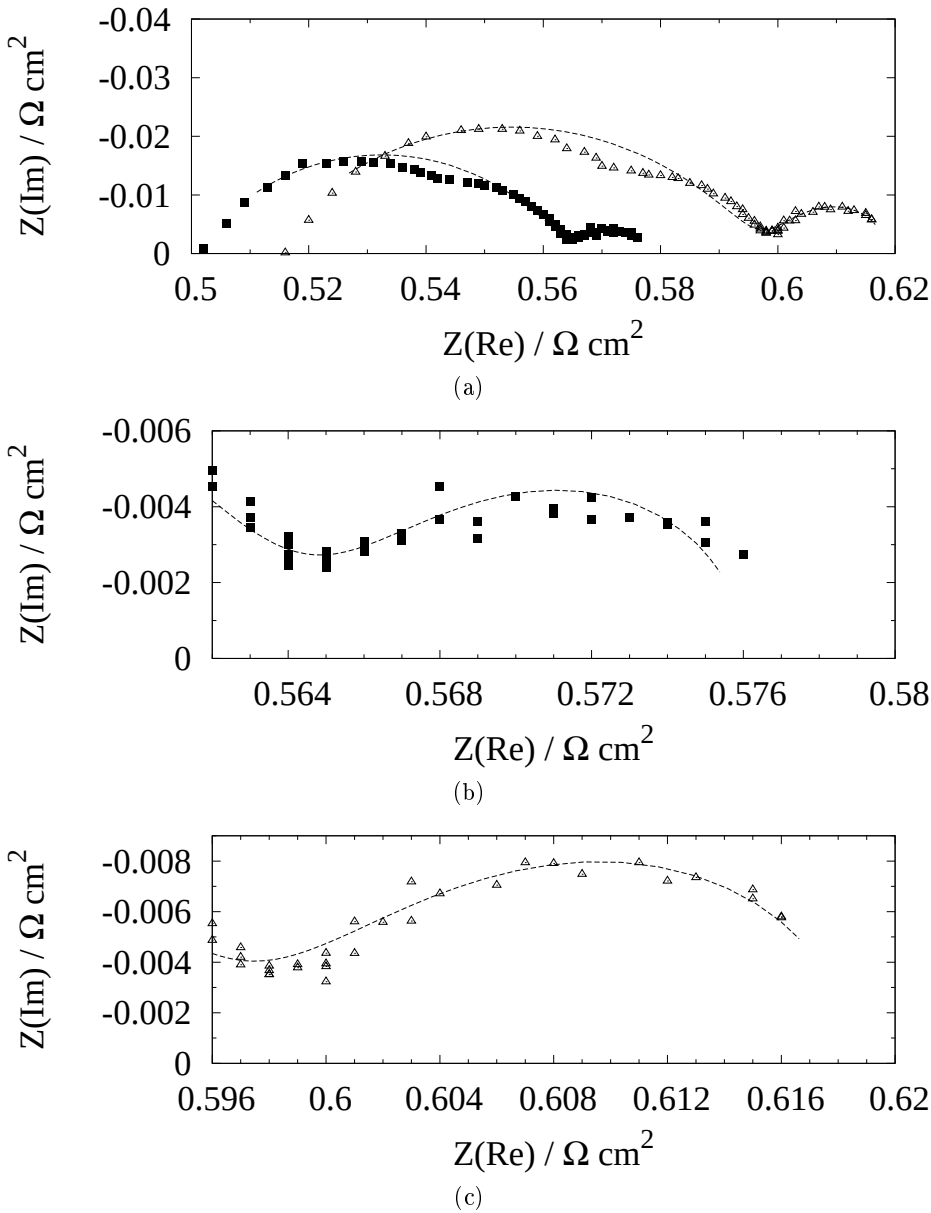

Figure 2.2. (a) The impedance spectrum of a cell with two identical, new hydrogen fuel cell membrane electrodes and a proton-conducting, water-filled membrane. The electrodes are E-TEK assemblies and the membrane is Nafion 117. The hydrogen gas saturated with water has a pressure of 1 bar, and the cell temperature is 30°C. The applied potential is 0 (left curve) and 50 mV (right curve). Lines represent the fitted data. (b) The last arc magnified for the unpolarised electrode. (c) The last arc magnified for the 50 mV experiment.

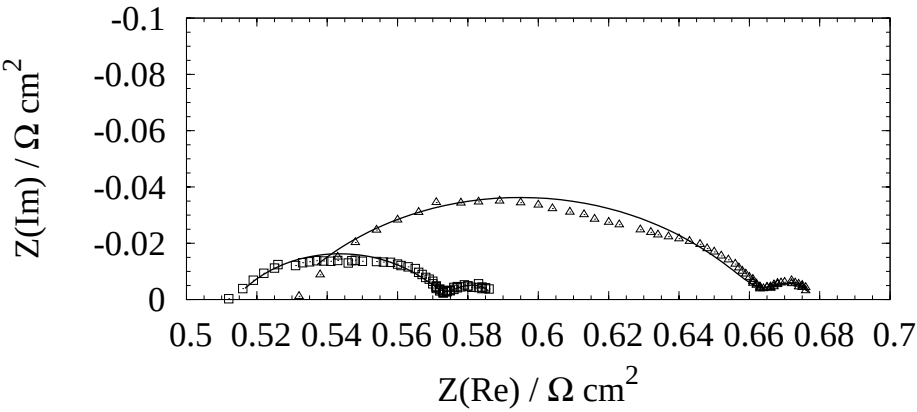

Figure 2.3. The impedance spectrum of an unpolarised cell with two identical hydrogen fuel cell membrane electrodes and a proton-conducting, water-filled membrane. The electrodes are E-TEK assemblies and the membrane is Nafion 117. The hydrogen gas saturated with water has a pressure of 1 bar, and the cell temperature is 30°C. To the left, the impedance of a new MEA, and to the right, the same MEA after 30 experiments. Lines represent the fitted data.

2.6 Discussion

The first conclusion to be made is that the high frequency intercept with the real axis in Fig. 2.2 is remarkably constant in all spectra recorded, it is $0.50 \pm 0.02\ \Omega\ \mathrm{cm}^2$ in Table 2.1, and does not vary more than 5% between the samples investigated. The value, which is the area resistance of the Nafion 117 membrane in the cell, is in good agreement with results reported in the literature [40] for the same membrane and 25°C. The reproducible value can be taken as experimental support for a reproducible sample preparation method. We can thus expect the same agglomeration level of catalyst particles, or fractality in the materials, between the samples that were investigated. The absence of inductance is also a good sign. Therefore, in spite of the complicated heterogeneous structure of the electrode, we believe that the observations reflect real electrochemical processes, rather than instrument artifacts.

2.6.1 The Gerischer element

Our most interesting experimental finding is the low frequency semicircle in the impedance diagram. We find that this can only be fitted in a meaningful way to a Gerischer phase element. A fit to a Warburg impedance is *not* possible, as such an element does not turn to the axis, but continues at a

45° angle. The behaviour seen in Fig. 2.2 is in sharp contrast to results for the hydrogen oxidation reaction on Pt electrodes in acid solutions, a reaction which is diffusion controlled [54]. Similarly shaped arcs have been seen before [31, 48], but only Gonzales-Cuenza et al. [48] have used a Gerischer element in their interpretation (for a porous solid oxide fuel cell electrode). A Gerischer element has not previously been reported for this electrode.

Alternative circuits were tried like the Randle's circuit and the same circuit with CPE. When fitted to a Randle's type circuit with two CPE, the last arc gave an α value of 0.50 $\pm$0.02, a clear indication of a Gerischer type element. None of the alternative fits had the accuracy we found when a Gerischer element was used (around 10% in the fitted variable Y_0, see Table 2.1). Self similar (fractal) surfaces have a depressed semi-circle, it is however symmetric unlike the Gerischer [46, 55]. In addition, we found studying the ageing of the cell, that the Gerischer element was unchanged in the experiments (Fig. 2.3). The layer in front of the catalyst is thus not ageing, in agreement with the view that ageing involves agglomeration of Pt particles [52]. We therefore have confidence in the conclusion that the electrode mechanism must include a step which involves adsorption combined with diffusion. We proceed to discuss possible relevant models in section 2.6.3.

For comparison, Ciureanu and Wang [30] obtained an α-value of 0.7 for the second arc in their spectrum. They found that this arc did neither depend on the gas flow rates between 20 and 1200 sccm, nor on $\omega^{-1/2}$, and allocated the arc to hydrogen adsorption at the Pt- surface. In our view their evidence is not conclusive for such an allocation, see also the discussion below.

In their study of the whole fuel cell, Paganin et al. [29] also found a low frequency arc at 10 mHz, where we see our second arc. These authors allocated the arc to water *diffusion*, because it depended on the membrane thickness. This allocation cannot be correct, since such a phenomenon would give a more Warburg-like behaviour. Furthermore, the fractal nature of the material can explain a depression like the one described by a constant phase elements, but it cannot explain a Gerischer element.

As a remaining possibility, we discuss the possibility that the present Gerischer element can be allocated to reaction and diffusion on the membrane side of the electrode surface. On the membrane side a reaction must involve charged or polarised species (protons and water). Such processes are not expected to be slow and have a relaxation time in the order of seconds, as observed here.

2.6.2 The high frequency regime

The high frequency regime of the impedance diagram, is according to the theory of Section 2.3, Eq. (2.49), related to the charge transfer step. It is immediately clear, however, that the peak is not a perfect semicircle. In some experiments it appeared as one depressed semi-circle, but in others, like shown here, a shoulder could be seen on the right hand side of the (depressed) peak. There is such a shoulder in the unpolarised as well as the polarised electrode (see Fig. 2.2).

The heterogeneity of the electrode may cause a depression of the arc like the one we and others have observed. This has also motivated us and others [30] to fit this part of the circle to a constant phase element. The value of the variable $\alpha_{\rm ct}$ in the fit of the diagram to such an element was 0.61 ± 0.02 for all applied dc-potentials (see the heading of Table 2.1).

The shoulder indicates that a third phenomenon is present. We expect that water may be rate-limiting for the electrode reaction in some contexts. We have assumed that there is equilibrium for water everywhere, but the formation of this equilibrium may not be so fast that this assumption is correct. A rate-limiting role for water, which has been proposed also by others [29, 40, 56], requires a revision of the theory given above. We have chosen to postpone a detailed revision of the theory, and focus on the implications of the Gerischer element. For the time being, we regard the first part of the diagram in a qualitative manner. The part reflects the charge transfer step and possibly a proton hydration step. The relaxation times for both possible steps are around a millisecond.

In order to derive system properties from the diagram, a fit was made as described in section 2.3.4. Neither $T_{\rm ct}$ nor $\rho_{\rm ct}$ obtained from this fit, varied much with the applied potential (see Table 2.1). The resulting $\tau_{\rm ct}$, calculated using Eq. (2.54), is $4.6(\pm0.4)\times10^{-4}$ s for all applied dc-potentials. $T_{\rm ct}$ and $\rho_{\rm ct}$ did vary with the number of experiments, however (Fig. 2.3). This may be typical for a low resistance electrode like the hydrogen electrode. We shall discuss the details in this part of the diagram in a report to come, and return now to the low frequency part.

2.6.3 The adsorption reaction on pore walls in the carbon backing

A number of questions arise from the conclusion that there is Gerischer element in the equivalent circuit. If the data shows that there is an adsorption - reaction

process present, how sure can we be that it takes place along the pore walls in the carbon backing and not at the Pt- particles? After all, Chen and Kuzernak [43] found, using Pt on carbon as a catalyst, that an adsorption step took place in front of the charge transfer step *on the submicron Pt particles*. The carbon was not exposed to hydrogen in this case, however. But, how sure can we be, that hydrogen diffuses as a molecule and not as an atom before it reaches the surface? Can we understand the kinetic parameters, that we obtain for the adsorption reaction, for one model, but not for the other? And finally, what are the possible consequences of the finding?

Let us discuss the location of the reaction diffusion process first. It is true that equations can be obtained with the exact same form as given above, but with a Gerischer type element valid for the catalyst surface instead as for the porous carbon phase. We need only assume that the reaction (ad) and the diffusion takes place at a different location. The consequences of such a shift are several, however, and we shall argue against them below, mainly from implications for the system's *properties*.

We can first observe that the relaxation time $\tau_{\rm ad}$ is constant with the applied dc potential in the experiments (see the last row of Table 2.1). This is exactly as predicted from Eq. (2.33), however. This fact alone does not favour the carbon backing over the surface as a location for the reaction. We have therefore made the following estimates for the diffusion constant $D^{\rm a}_{\rm H_2}$ and the variables that follow from knowledge of $D^{\rm a}_{\rm H_2}$.

With a porosity of the electrode of 0.4 [36], and a pore diameter of 50 nm [57], the estimated surface area of the pores is $3{\times}10^{-7}{\rm m}^2$ of carbon. The diffusion coefficient of hydrogen in the gas phase is order of magnitude $2{\times}10^{-4}$ ${\rm m}^2/{\rm s}$ [58]. Scaled for the surface volume fraction (taking a surface thickness of 0.33 nm), and a tortuosity of 7 [36], this gives a course-grained value of $D^{\rm a}_{\rm H_2} = 3{\times}10^{-7}$ ${\rm m}^2/{\rm s}$. We find from Table 2.1 and Eq. (2.57) that the equilibrium concentration of hydrogen at the surface is $c^{a}_{\rm H_2,eq} = 260$ ${\rm mol}/{\rm m}^3$ in the unpolarised electrodes, and decreases to 148 ${\rm mol}/{\rm m}^3$ for $\Delta\phi_{\rm dc} = 60$ mV across the cell. The kinetic constant follows from Table 2.1 and Eq. (2.33) and is $k^{\rm d}_{\rm H_2} = 0.25$ ${\rm s}^{-1}$ for all values of the applied potential. A characteristic length for the reaction-diffusion layer is then:

$$l^{\rm a}_{\rm H_2} = \sqrt{D^{\rm a}_{\rm H_2}\tau_{\rm ad}} = 1.5 \text{ mm} \tag{2.60}$$

Reducing the coarse-grained surface diffusion coefficient by a factor 10, will increase the concentrations with a factor 3.3, and reduce the characteristic

length by the same factor. A mono-layer of H_2 corresponds to a coarse grained concentration of about 3 kmol/m^3. The concentration we calculated above is well below this value, which is reasonable. A characteristic length of 200 μm, comparable to the thickness of the anode backing, would correspond to a diffusion coefficient of $D^{\mathrm{a}}_{\mathrm{H_2}} = 5{\times}10^{-9}$ m^2/s and a close to fully occupied mono-layer.

The range of probable values can thus explain that reaction and diffusion takes place across a carbon layer with a thickness characteristic for the fuel cell electrode backing, of around 200 μm. They are all too large to explain that a similar step takes place at the metal (Pt) particle itself, because these particles are submicron particles [57]. A similar estimate for the Pt surface gives a characteristic length much larger than the size of the particle. We conclude that the Gerischer element cannot be understood by reaction combined with diffusion on the Pt surface. The value obtained by Bae and Lee [59] for the equilibrium adsorption of hydrogen molecules on a carbon molecular sieve, was for comparison, $c^{\mathrm{a}}_{\mathrm{H_2,eq}} = 4$ kmol/m^3 for 1 bar, when adjusting for a density of the carbon sieve of 0.6 g/cm^3.

If the estimates above hold, the carbon surface plays a more active role in the electrode reaction than hitherto assumed. This may then have a consequence for the design of the electrode. When the access of hydrogen to the three phase contact line is via the two-phase contact, and this contact can become rate-limiting, the two-phase contact should be made as large as possible.

The results do not give any conclusive information on the state of adsorbed hydrogen on the carbon surface. The mathematical form of the impedance, Eq. (2.49), does not distinguish between models (ad-1) or (ad-2). The relaxation time is constant in both models as long as the concentration of hydrogen in the gas in the pores is constant.

Most reports consider physisorption of hydrogen gas on carbonaceous materials. Diffusion of physisorbed molecules may be faster than of chemisorbed atoms, favouring a large value of $l^{\mathrm{a}}_{\mathrm{H_2}}$ like we estimate. The value of the admittance Y_0 in Table 2.1 is sensitive to the applied potential, however. This property depends in the first model (ad-1) on the concentration of adsorbed molecules and the surface diffusion constant of H_2. In the second model, the relevant concentration is that of the adsorbed hydrogen atoms. It is likely that the chemisorbed state depends more on the polarisation. There is some support for hydrogen adsorption in atomic form on graphite-like forms [42].

More experiments should be performed to establish relations further. Knowledge about the surface diffusion constant will be helpful. It may be interesting to vary the gas pressure and the temperature. Also important is to study the role of water. Does it play a role in getting the proton into the membrane, as indicated by the high frequency part of the diagram?

2.7 Conclusion

Electrochemical impedance spectroscopy was performed on the fuel cell electrode E-TEK, Elat/Std/DS/V2 0.5 mg Pt/cm^2, 20 Pt/C, impregnated with 0.6 mg Nafion/cm^2 (5 wt% solution). The membrane contact was Nafion 117. The electrode was studied at 30° C and 1 bar.

We found that a Gerischer element was required to explain the low frequency part of the electrode impedance. The variables that were deduced from this element support hydrogen adsorption and diffusion along carbon in front of the catalyst where the charge transfer takes place. The data do not allow us to conclude on the form of the adsorbed hydrogen. It may be physisorbed or chemisorbed. Experiments that may answer this question were proposed. Water may also enter rate-limiting steps in the electrode reaction, but its role needs further clarification.

Acknowledgements

A.K. Meland is grateful to Nordic Energy Research and Norsk Hydro ASA.

Chapter 3

Rate limiting proton hydration in the anode of the polymer electrolyte membrane fuel cell

Anne-Kristine Meland and Signe Kjelstrup

Department of Chemistry
Norwegian University of Science and Technology,
N-7491 Trondheim, Norway

This paper has been published in
J. Mem. Sci 282, 96-108, 2006

Abstract

We studied the isothermal hydrogen adsorption and reaction at the carbon and platinum (Pt) surface of the humidified E-TEK electrode of a polymer electrolyte fuel cell (PEMFC) with a Nafion 117 membrane by impedance spectroscopy at 30 and 50°C. We found three rate-limiting steps, one of them is interpreted as proton hydration, a step that has not been reported previously. We analysed the influence of water transport on the impedance and found that the semicircle for the charge transfer reaction and that of proton hydration are superimposed at 50°C, but separate at 30°C. Additional evidence is presented for hydrogen adsorption to the carbon surface prior to charge separation. The surface diffusion coefficient of hydrogen was calculated to 1 x 10^{-7} m^2/s.

3.1 Introduction

It is well known that water plays an important role in the low temperature polymer membrane fuel cell (PEMFC). High performance of PEMFC requires a continuous supply of water to hydrate the membrane and maintain its proton conductivity. Water is carried by protons that are transported through the membrane from the anode to the cathode, i.e. electro-osmosis. Water is also produced at the cathode. This will induce a diffusional back flow of water in the membrane [60].

But does water affect the anode reaction? To answer this question one can use impedance spectroscopy. This is an experimental technique that can separate phenomena with different relaxation times, and is thus useful for determination of rate-limiting steps at electrode surfaces [37]. It has been used widely, also in studies of rather complicated three-phase contacts [29, 38], which are typical for fuel cell electrodes.

The fuel cell electrodes consist of a porous matrix of carbon black that allows gas diffusion up to the catalyst (Pt) particles. The gas reacts at the catalyst, which is in contact with the proton-conducting membrane electrolyte. Three phases must be near each other to allow charge transfer. To describe the events at the three-phase contact-line by thermodynamic variables is a difficult task. The successful agglomerate model [61] describes the production of charges in the interface region in a continuous way. We have chosen to address the problem, taking a Gibbs surface as a starting point [62]. In this picture, the interface region, which in fact has a thickness around 10 μm, is described

as a two-dimensional layer. It is a separate thermodynamic system, and we shall refer to this layer as *the surface.* The thermodynamic variables of this layer are excess properties [60]. In the present case, the surface contains excesses of catalyst material (platinum), gas, adsorbed gas and water, membrane polymer and membrane water. This description leads to discontinuities in the thermodynamic variables at the surface.

We have earlier studied the cell in which both the anode and cathode were hydrogen electrodes. The electrode region was considered to consist of a catalyst interface (i.e. the two-dimensional thermodynamic system), surrounded on one side of a homogeneous phase of gaseous carbon, and on the other side of a homogeneous phase of a water filled membrane, respectively. In order to reach the platinum catalyst and the surface, the gas was allowed to diffuse also along the carbon phase. The electrode region is pictured schematically in Fig. 3.1. We see the two-dimensional surface indicated by two stippled vertical lines, and the surrounding homogeneous phases. The transport pathway for hydrogen is on the right hand side, while the flux of hydrated protons in the membrane is to the left in the figure. In our coarse grained, one-dimensional description, transport takes place along a coordinate normal to the surface of the membrane. All variables are then independent of coordinates parallel to the surface. Using these conditions with this division into subsystems, we were able to derive the electrode impedance for the interface with two rate-limiting steps [62] of charge transfer and of hydrogen adsorption/diffusion on carbon. The present work offers supplementary support for these steps, and includes also a third step, namely proton hydration.

Impedance studies of the hydrogen electrode have mostly been motivated by the need to understand the CO tolerance of this electrode [30, 31]. As a background for such studies, it is important to have a good understanding of the elementary steps concerning hydrogen alone. This is why we have chosen to use only hydrogen electrodes here. We have found experimental support for the hypothesis of reversible gas adsorption on carbon black as a first step in the electrode reaction. The adsorption reaction took place most probably in front of the catalyst (Pt) particles. In our previous paper [62] we assumed that water was in equilibrium throughout the system, even if results from the high frequency part of the impedance diagram indicated that this assumption was questionable. In this paper we analyse by theory and experiments how water affects the behaviour of the system, using again two hydrogen electrodes. We shall see, that it is probably not correct to assume equilibrium for water at the surface, not even in the absence of a d.c. electric current. At low tempera-

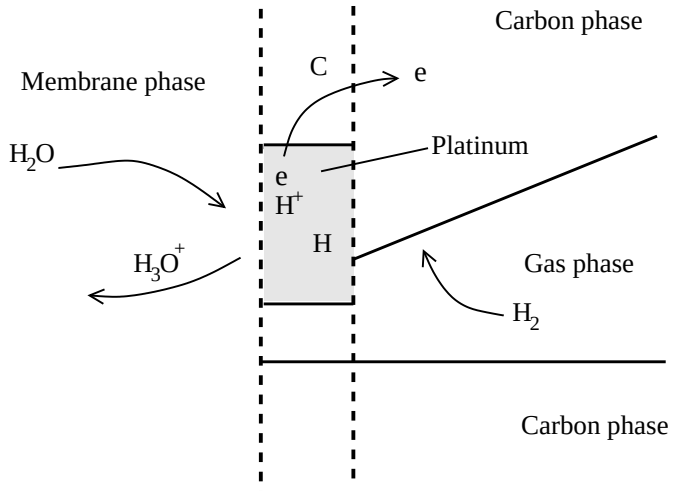

Figure 3.1. Schematic drawing of the electrocatalyst layer, the thermodynamic surface, and its adjacent homogeneous phases.

tures, we find evidence that hydration of protons can be rate-limiting at high frequencies in the anode reaction of PEMFC, also when the electric current is zero. The membrane electrode assemblies consisted of E-TEK electrodes with 0.5 mg Pt/cm^2 and a Nafion 117 membrane.

The paper is organised as follows. The model is first described in section 3.2. We then give the formulae of the impedance (which is derived in Appendix A.1) in section 3.3. The experiments and the results, which confirm the three-step model, are then described in sections 3.4 and 3.5 and discussed in section 3.6.

3.2 A model with three rate-limiting steps

The model assumes that hydrogen gas is first adsorbed along the pores in the carbon matrix (see Fig. 3.1):

$$\frac{1}{2}\mathrm{H_2(g)} \rightarrow \frac{1}{2}\mathrm{H_2(a)} \tag{3.1}$$

Adsorption can happen close to or far from the platinum particle. Once adsorbed, hydrogen proceeds to diffuse along the carbon surface to the platinum, that is located in the electrode interface [63]. The catalyst particle is located in the surface between the porous carbon matrix and the cation exchange membrane (see grey area in Fig. 3.1). During the diffusion process some of the

hydrogen molecules desorbs back to form molecular hydrogen in the gas phase. We assumed that the adsorption has a first order forward reaction in both directions (the superscript a refers to the carbon surface of the anode):

$$r(x,t) = \frac{1}{2}k^{\mathrm{a}}_{\mathrm{H_2}}c^{\mathrm{g}}_{\mathrm{H_2}} - \frac{1}{2}k^{\mathrm{d}}_{\mathrm{H_2}}c^{\mathrm{a}}_{\mathrm{H_2}}(x,t) \tag{3.2}$$

A model using adsorption of atomic hydrogen was also possible [62]. We use a coarse-grained description in which both concentrations are given in $\mathrm{mol/m^3}$ for the carbon matrix. The concentration $c^{\mathrm{g}}_{\mathrm{H_2}}$ is the time and position independent concentration in the pores times the porosity of the layer. The concentration $c^{\mathrm{a}}_{\mathrm{H_2}}(x,t)$ is the concentration in $\mathrm{mol/m^2}$ times the surface area of the pores per unit of volume (in $\mathrm{m^{-1}}$). In most models, the adsorption reaction (1) is assumed to take place on the metal surface, see e.g. [43]. We have shown that the adsorption may take place earlier, and have found to continue working with this hypothesis [62]. Support for this model has recently been given also by Paulus et al. [63].

In the Tafel-Volmer mechanism, the molecule dissociates into protons and electrons in active sites in the electrode surface on the platinum particles:

$$\frac{1}{2}\mathrm{H_2(a)} \rightarrow \mathrm{H^+(s)} + \mathrm{e^-(a)} \tag{3.3}$$

Electrons are eventually transported into the anode carbon phase (see Fig. 3.1).

There are two modes of transport related to water in the fuel cell membrane: (1) the electro-osmotic transport, or (2) diffusion of water. The transport number of water in the membrane is a measure of the number of water molecules that is carried by each proton in the absence of a concentration gradient. For the vapour-equilibrated membrane the transport number, $t_{\mathrm{H_2O,vap}}$, was close to 1 [64]. In the present case, the membrane is saturated with water, and the transport number can be regarded as constant [65]. We may therefore in good approximation, say that one water molecule is associated with each proton that is moving across the membrane. The protons bind then, on the average, to one water molecule at the surface, before they move into the cation exchange membrane (m) as hydronium ions:

$$\mathrm{H^+(s)} + \mathrm{H_2O(m)} \rightarrow \mathrm{H^+H_2O(m)} \tag{3.4}$$

In summary, we have a model where hydrogen is adsorbed as molecular hydrogen/atomic hydrogen on the surface of the carbon pores in a reaction-diffusion

layer located before the surface. The hydrogen is then converted into protons and electrons in active sites in the surface on the platinum catalyst in Fig. 3.1. The electrons move into the carbon phase (a porous matrix), while the protons bind to water at the surface to form hydronium ions which move into the membrane. The thickness of the carbon phase in the experiment is in the order of 0.5 mm, while the thickness of the catalyst layer is in the order of 0.01 mm.

The impedance that follows from these steps is derived in the Appendix. The impedance was derived following a systematic procedure, starting with the mass and energy balances of the steps, and using the entropy production of the surface to define the relation between the surface potential drop and the electric current as a function of frequency.

3.3 Equations for data reduction

We show in Appendix A.1, by combining Eqs. (A.38) and (A.42)-(A.44), that the impedance of the whole surface is

$$Z^{\mathrm{s}} = \frac{\rho^{\mathrm{s}}_{\mathrm{cm}} + Z_{\mathrm{ct}}}{1 + i\omega C^{\mathrm{s}}_{\mathrm{H_3O^+}} \left(\rho^{\mathrm{s}}_{\mathrm{cm}} + Z_{\mathrm{ct}}\right)} \tag{3.5}$$

In this equation, Z_{ct} is the impedance of the charge transfer step

$$Z_{\mathrm{ct}} = \frac{\rho^{\mathrm{s}}_{\mathrm{ct}} + Z_{\mathrm{ad}}}{1 + i\omega C^{\mathrm{s}}_{\mathrm{H^+}} \left(\rho^{\mathrm{s}}_{\mathrm{ct}} + Z_{\mathrm{ad}}\right)} \tag{3.6}$$

and the capacitance and the resistivity of the proton hydration are given by $C^{\mathrm{s}}_{\mathrm{H_3O^+}}$ and $\rho^{\mathrm{s}}_{\mathrm{cm}}$. The relaxation time for the proton hydration reaction, τ_{cm}, is

$$\tau_{\mathrm{cm}} = \rho_{\mathrm{cm}}\, C^{\mathrm{s}}_{\mathrm{H_3O^+}} \tag{3.7}$$

The find that the proton hydration, step 3, modifies the impedance of the charge transfer step. The impedance of step 1, the step for adsorption and surface diffusion was given by [62]

$$Z_{\mathrm{ad}} = \frac{RT}{2F^2 c^{\mathrm{a}}_{\mathrm{H_2},eq}\sqrt{2Dk^{\mathrm{d}}_{\mathrm{H_2}}(1 + i\omega\tau_{\mathrm{ad}})}} \tag{3.8}$$

where the relaxation time in the absorption process was

$$\tau_{\mathrm{ad}} = \frac{2}{k^{\mathrm{d}}_{\mathrm{H_2}}} = \frac{2c^{\mathrm{a}}_{\mathrm{H_2},eq}}{c^{\mathrm{g}}_{\mathrm{H_2}} k^{\mathrm{a}}_{\mathrm{H_2}}} \tag{3.9}$$

The hydrogen pressure in the pores was assumed constant in the derivation of this equation, giving a constant gas concentration, $c^{\mathrm{g}}_{\mathrm{H_2}}$ and therefore also a constant value for the concentration of absorbed gas at equilibrium, $c^{\mathrm{a}}_{\mathrm{H_2,eq}}$. The impedance Z_{ad} was the impedance of a Gerischer element. Experimental results fitted this impedance better than a finite length Warburg element, so it shall be used also here, see the Results section below.

The equivalent circuit that can be put up on the basis of Eqs. (3.5) and (3.6) is given in Fig. 3.2. In this context it is important to note that the sequencing of the contributions to the total spectrum is fixed. There is no possibility to switch the elements of the circuit in Fig. 3.2. When $\omega \to \infty$, we see that:

$$Z^{\mathrm{s}}_{\omega\to\infty} = 0 \tag{3.10}$$

In the present experiments, we measure the response of two identically made electrodes plus membrane electrolyte. When a dc current is passing the cell, one electrode will be a sink for hydrogen, while the other will be a source for hydrogen. The impedances of the two electrodes are the same, however. Both electrodes therefore give the same contribution to the measurement, also when the electrodes are polarised. In terms of the measured impedance, Z^{cell}, and the membrane impedance, Z^{mem}, the impedance of one electrode is then;

$$Z^{\mathrm{s}} = \frac{1}{2}(Z^{\mathrm{cell}} - Z^{\mathrm{mem}}) \tag{3.11}$$

The membrane impedance is found by assuming $Z^{\mathrm{mem}} = Z^{\mathrm{cell}}$ as $\omega \to \infty$. The results that are calculated for Z^{s} from Eq. (3.11), can now be fitted to formulas (3.5) and (3.6) using Eq. (3.8) for Z_{ad}.

A constant phase element (CPE) shall be used for the charge transfer step in Eq. (3.5), rather than one capacitance in parallel with the resistance. The CPE is defined as:

$$\mathrm{Z_{CPE}} = \frac{1}{T_{\mathrm{ct}}(i\omega)^{\alpha}} \tag{3.12}$$

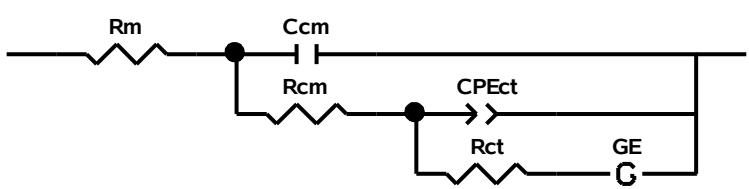

Figure 3.2. Equivalent circuit on the basis of Eqs. (3.5) and (3.6).

The phase angle of the CPE impedance is constant and independent of the frequency. When α equals 1, CPE is identical to $C_{\rm ct}$. The more depressed the semi-circle is, the lower is the α-value. We found α to be typically 0.82. The relaxation time for the charge transfer reaction is

$$\tau_{\rm ct} \equiv (T_{\rm ct}\ \rho_{\rm ct})^{1/\alpha} \tag{3.13}$$

Eq. (3.6) then becomes:

$$Z_{\rm ct} = \frac{\rho^{\rm s}_{\rm ct} + Z_{\rm ad}}{1 + T_{\rm ct}(i\omega)^{\alpha}\,(\rho^{\rm s}_{\rm ct} + Z_{\rm ad})} \tag{3.14}$$

The limiting behaviour $\omega \to 0$ gives

$$Z^{\rm s}_{\omega\to 0} = Z_{\omega\to 0,{\rm ad}} + \rho_{\rm ct} + \rho_{\rm cm} \tag{3.15}$$

The fit of the experimental results to the theoretical expressions gave Y_0 and $\tau_{\rm ad}$ in the following expression for $Z_{\rm ad}$:

$$Z_{\rm ad} = \frac{1}{Y_0\sqrt{\tau^{-1}_{\rm ad} + i\omega}} \tag{3.16}$$

The expression for the relaxation time, $\tau^{-1}_{\rm ad} = k^{\rm d}_{\rm H_2}/2$, was given in Eq. (3.9) while the other variable is

$$Y_0 = \frac{2F^2}{RT} c^{\rm a}_{\rm H_2,eq}\sqrt{2Dk^{\rm d}_{\rm H_2}\tau_{\rm ad}} = \frac{4F^2}{RT} c^{\rm a}_{\rm H_2,eq}\sqrt{D} \tag{3.17}$$

We see that the admittance Y_0 is proportional to the hydrogen concentration in the gas phase, that is the hydrogen pressure. Knowledge of the diffusion constant for hydrogen along the pores gives $c^{\rm a}_{\rm H_2,eq}$ from this equation. Such calculations were performed earlier.

3.4 Experimental

3.4.1 The membrane-electrode assembly

The electrodes were E-TEK Elat/Std/DS/V2 gas diffusion electrodes with a loading of 0.5 mg Pt/cm^2. The catalyst was 20 wt% Pt supported on Vulcan XC-72. To obtain a better ionic contact between the layers in the membrane- and electrode assembly (MEA), the electrodes were sprayed with a 5% Nafion

solution to give 0.6 - 0.8 mg/cm^2. This was done with a Badger Airbrush Pistol (model 200). The airbrush was operated at an air pressure of about 200 kPa (2 bar). The electrode was weighed before and after the spraying so the amount of Nafion could be calculated. The electrodes were then dried in a heating cabinet at 125°C for 30 minutes. The electrodes were stored at least 48 hours before they were used in the fuel cell.

The MEA consisted of two identical electrodes separated by a Nafion membrane. The membranes were pretreated in several steps as described for instance by Møller-Holst [51]. This procedure included hydrogen-peroxide (5%) to oxidise organic impurities, sulfuric acid (0.05 M) to remove metallic impurities and rinsing in distilled water several times. All was done at temperatures around 90°C. The prepared membranes were stored in distilled water until use.

The mechanical pressure over the MEA was 4.2 barg, controlled by a pneumatic piston. The hydrogen gas pressure on the two sides of the MEA were the same and varied between 1 and 4 bar. The pressure and temperature were constant during each experiment. The hydrogen flow into the cell was controlled by Brooks 5850S mass flow controllers.

The MEAs were tested in a test-station developed by Møller-Holst [51] and Vie [66]. The fuel cell was a circular single cell with a cell area of 4.91 cm^2. The fuel cell housing was made of stainless steel (SS-316) and was supported by two pistons (SS-316). At the top of the pistons there were serpentine patterned flow fields. These pistons also served as current collectors. Each piston contained a heating element. Thermocouples inside the cell housing measured the temperature at the electrode backings. The temperature was controlled by a PID controller (Eurotherm 2408) and a Pt-100 thermistor to 30.0±0.1 and 50.0±0.1°C.

3.4.2 The gas humidifying system

The hydrogen gas (AGA 99.999%) was humidified at 80°C before it entered the cell, making sure that gas was always saturated with water. The dry gas entered at the top of the humidifier tank and was preheated in a heating coil. The gas was then bubbled through a glass-sieve and finely dispersed into an 800 ml internal container filled with water at a given temperature. The small internal container was placed inside a larger 10 l tank also filled with water. This outer tank was heated with an electrical heating tape. This ensures a stable temperature of the gas. The humidified gas left the humidifier at the

top of the internal container and entered then the fuel cell system. Saturation of the gases at the given temperature can then be assumed. The humidifying temperature was always minimum 20°C higher than the cell temperature to prevent the MEA to drying out when electric current was passing the cell.

3.4.3 The water condensers

The water condensers were designed by Vie [66]. They remove the water by condensing the water in the gas flow. The outer container has a volume of 10 l and is filled with cooling water. Gas enters at the top of the container, goes through a condensing coil and into a smaller (500 ml) condensate tank. The gas escapes at the top of the tank and water at the bottom. The condensers are able to operate at an elevated pressure and the condensing medium is tap water (5-8°C). There are two condensers in the system, one for the anode side and one for the cathode side. The gas from each condenser enters a pressure control valve (Brooks 5866). The valves are controlled from the computer.

3.4.4 Impedance measurements (EIS)

The impedance diagrams were recorded using a PAR 263A/94 potentiostat and a Solartron 1260 FRA. Z-plot software from Scribner Ass. Inc. was used to run the experiments. Measurements were made in a two-electrode set-up on freshly prepared membrane-electrode samples, unless otherwise is stated. The impedance was obtained by sweeping over the frequencies from 10 kHz to 10 mHz, recording 12 steps/decade, for each pressure. An amplitude of 5 mV was used in all experiments.

The impedance was first measured at 30°C, with zero dc voltage across the cell, and with the varying gas pressure. Five different hydrogen pressures were used: 1.0, 1.56, 2.25, 3.06 and 4.0 bar.

The impedance was next measured, with constant gas pressure (1 bar) at different dc voltages. The applied dc voltages were 10, 20, 30, 50, and 60 mV. The temperature was then 30 and 50°C.

3.5 Results

3.5.1 Data reductions

The results are shown in Figs. 3.3-3.8. At all pressures at low temperature and no dc voltage (Figs. 3.3, 3.4, 3.6 and 3.7), the EIS showed three relaxing phenomena, as expected from the theoretical model. All data were therefore interpreted using this model. All spectra were fitted using the software Z-View (Scribner Associated Inc.) and are given as Nyquist plots of Z^{cell}. The results of the fits of these as well as those from the previous article [62] are given in Appendix A.2, Tables A.4-A.9. The two high frequency arcs became superimposed at the highest temperature, 50°C, see Fig. 3.5.

The relaxation times for all three processes are presented in Tables 3.1 - 3.3. The relaxation time for adsorption/diffusion τ_{ad}, followed directly from the measurements. The relaxation time for the charge transport, τ_{ct}, was calculated using Eq. (3.13) and the relaxation time for the proton hydration reaction, τ_{cm}, was found using Eq. (3.7).

Table 3.1. Relaxation times for the three rate-limiting steps in the symmetric cell with E-TEK Elat 0.5 mg Pt/cm^2 gas diffusion electrodes and Nafion 117 membrane for various hydrogen gas pressures. $T = 30°C$ and E=0 V. τ_{cm} and τ_{ct} were calculated using Eqs. (3.7) and (3.13). τ_{ad} followed directly from the data fitting.

p_{H_2} (bar)	τ_{cm} (10^{-4} s)	τ_{ct} (10^{-3} s)	τ_{ad} (s)
1.00	2.61	2.9	6
1.56	2.05	4.1	6
2.25	1.94	5.5	6
3.06	1.92	6.5	6
4.00	1.86	6.9	6

3.5.2 The membrane area resistance

A constant membrane area resistance, R_{m}, was observed. For the experiments done at 30°C, the membrane area resistance was 0.50±0.02 Ω cm^2 and when the cell temperature was raised to 50°C, the value was 0.40±0.02 Ω cm^2. These values are in good agreement with results reported in the literature for the same membrane and temperatures [29, 40], and are taken as evidence for a good measurement technique. The resistances did never vary more than 5%

Table 3.2. Relaxation times for the three rate-limiting steps in the symmetric cell with E-TEK Elat 0.5 mg Pt/cm^2 gas diffusion electrodes and Nafion 117 membrane for various potentials. T=30°C and p_{H_2}=1 bar. τ_{cm} and τ_{ct} were calculated using Eqs. (3.7) and (3.13). τ_{ad} followed directly from the data fitting.

$\Delta\phi_{dc}$ (mV)	j (A/cm^2)	τ_{cm} (10^{-4} s)	τ_{ct} (10^{-3} s)	τ_{ad} (s)
0	0	2.49	3.5	6
10	0.02	2.32	3.7	8
20	0.03	2.34	3.9	8
30	0.04	2.33	4.4	8
50	0.07	2.30	4.6	8
60	0.08	2.35	5.0	8

Table 3.3. Relaxation times for the three rate-limiting steps in the symmetric cell with E-TEK Elat 0.5 mg Pt/cm^2 gas diffusion electrodes and Nafion 117 membrane for various potentials. T=50°C and p_{H_2}=1 bar. τ_{cm} and τ_{ct} were calculated using Eqs. (3.7) and (3.13). τ_{ad} followed directly from the data fitting.

$\Delta\phi_{dc}$ (mV)	j (A cm^{-2})	τ_{cm} (10^{-4} s)	τ_{ct} (10^{-3} s)	τ_{ad} (s)
0	0	9.9	4.2	5
10	0.02	9.6	2.9	5
20	0.04	9.4	3.0	5
30	0.07	7.4	3.8	5
50	0.11	7.7	4.7	5
60	0.13	6.2	4.6	5

for a given MEA. This was seen as long as freshly prepared MEAs were used. Gas pressure changes (Table A.4) or changes in applied potential (Tables A.6 and A.8) did not change this.

The high reproducibility in the measured membrane resistance (± 5%), indicates also that the humidifying conditions were good. If the MEA was drying out, R_{m} would be increasing. We can thus conclude that the membrane at all times is saturated with water at the given temperature. The reproducibility of experiments makes this conclusion reliable.

3.5.3 The ageing effect

An ageing effect was observed in the spectra after prolonged use. After a few days or after ten to thirty experiments, a change was seen in the spectra. It was therefore important that the experiments were done as soon as a new system was mounted and shown to be stable. When two experiments were done after each other within about 24 hours, the results were identical. When the time interval between the experiments grew, and ageing effect was seen. Fig. 3.3 shows the ageing effect in one EIS experiment, repeated after 5 days with about thirty measurements. The resistance of the high frequency arc (proton hydration step) increased from 0.030 to 0.074 Ω cm^2 (150%) and the resistance of the middle frequency arc (charge transfer step) increased with 100% from 0.023 to 0.046 Ω cm^2. The low frequency arc for the adsorption/diffusion step did not change; however, pointing to its independence of the catalyst layer.

3.5.4 Effect of temperature

The cell temperature was either 30 or 50°C. Three arcs were seen at 30°C (see Fig. 3.4). At 50°C, two of the arcs overlapped (Fig. 3.5). The membrane area resistance, R_{m}, the proton hydration resistance, ρ_{cm}, and the charge transfer resistance, ρ_{ct}, all decreased by increasing temperature, see Tables A.6 - A.9. R_{m} decreased with 25% when raising the temperature, and both ρ_{cm} and ρ_{ct} decreased with approximately 75% when the temperature increased from 30 to 50°C, see Fig. 3.6. The capacitance for the proton hydration, $C^{\mathrm{s}}_{\mathrm{H_3O^+}}$ increased 1500 % when the temperature increased in the unpolarised cell.

Data were reduced with the three-step model described in the theory. The relaxation time for the proton hydration (τ_{cm}) increased with increasing temperature, the relaxation time for the charge transfer reaction (τ_{ct}) was almost constant with the temperature, while the relaxation time for the adsorp-

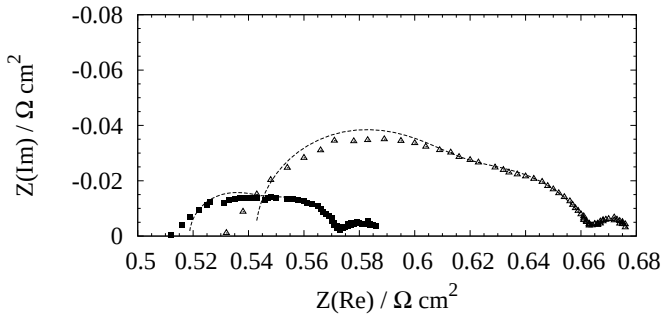

Figure 3.3. The impedance spectrum for the unpolarised symmetric cell at T=30°C and p_{H_2} = 1 bar. One experiment was done day one (left curve) and repeated 5 days later (right curve).

tion/diffusion process (τ_{ad}) decreased (see Tables 3.2 and 3.3).

3.5.5 Proton hydration as rate limiting step

The first arc (highest frequency) in the impedance diagram is, according to the model, related to proton hydration when the proton passes from the catalyst surface into the membrane. It was only possible to fit this arc using a pure capacitance and a resistance, and not a constant phase element. When the gas pressure increased, $C^{s}_{H_3O^+}$ and τ_{cm} decreased and ρ_{cm} increased slightly. The same was observed when the applied dc potential increased at constant gas pressure (1 bar) and 30°C, but here τ_{cm} remained almost constant. The results are given in Tables 3.1, 3.2, and A.6. When the temperature increased to 50°C and the gas pressure was constant (1 bar), $C^{s}_{H_3O^+}$ and ρ_{cm} were approximately constant while τ_{cm} decreased. The results are given in Tables 3.3 and A.8.

3.5.6 The charge transfer step

The second arc in the impedance diagram is, according to the model, related to the charge transfer step at the catalyst surface. As expected, it depended more on the applied dc potential than the other steps, see Tables A.5 and A.7. The relaxation time in these tables, τ_{ct}, increased with applied dc-potential and also with increased gas pressure. It is likely that the heterogeneity of the Pt surface can cause a depression like the one we observe. This was also the motivation for us and others [30] to fit this second arc to a constant phase element. The results in Tables A.5 and A.7 show that the resistance, ρ_{ct}, was not so sensitive to changes in applied dc-potential or gas pressure.

The value of α_{ct} decreased with increasing hydrogen gas pressure, see Table A.5. The value did not vary with the applied dc-potential at 30°C (see Table A.7). The average value was 0.82. When the temperature in the system was raised to 50°C, the value of α_{ct} increased (see Table A.9). The value approached one within the accuracy for all potentials given in Table A.9. When α_{ct} equals one, the CPE is a pure capacitance.

3.5.7 Rate-limiting adsorption/diffusion

The third arc was already related to an adsorption/diffusion step in the carbon backing in front of the catalyst [62]. The results from the present and previous experiments on this arc are given in Tables A.5, A.7, and A.9. The admittance, Y_0, decreased with the increasing dc-potential. It is now shown that Y_0 is a function of the hydrogen concentration in the gas phase, the equilibrium concentration (see Eq. 3.17) in Fig. 3.8. Only a small variation was seen, but the trend was systematic. The gradient of the straight line was found, and the diffusion coefficient was calculated to 1×10^{-7} m^2/s. This value fits very well with the estimate we made earlier for surface diffusion, represented for the porous material as a whole, 3×10^{-7} m^2/s and with a corresponding value of $c_{H_2,eq}$ of 260 mol/m^3. The relaxation time, τ_{ad}, remained constant when the gas pressure as well as the applied dc-potential was changed.

As an alternative interpretation, we considered also the finite-length Warburg element for the impedance of this layer. This element has the form

$$Z_{ad} = \frac{R_W \tanh\sqrt{T_W\ i\omega}}{\sqrt{T_W i\omega}} \tag{3.18}$$

giving here the impedance

$$Z_{ad} = \frac{RT}{4F^2 c_{H_2,eq,W}\sqrt{i\omega D_{H_2,W}}} \tanh\left(d\sqrt{\frac{i\omega}{D_{H_2,W}}}\right) \tag{3.19}$$

and the admittance

$$Y_0 = \frac{4F^2}{RT} c^a_{H_2,eq}\sqrt{D_{H_2,W}} = \frac{\sqrt{T_W}}{R_W} \tag{3.20}$$

where T_W and R_W are given directly from the fit of experiments to the Warburg element. The diffusion coefficient from this formula is $D_{H_2,W} = \frac{d^2}{T_W}$ where d is the thickness of the carbon matrix (200 μm) and T_W is from the fit (7.5 s). The fitted parameter R_W was 0.01 Ω cm^2. This gave the very small diffusion

coefficient 5×10^{-9} m^2/s, a reduction of two orders of magnitude compared to the aforementioned value. When this value is used in Eq. (3.20), the equilibrium concentration was calculated to 2700 mol/m^3 at 30°C. This value is ten times the value calculated before and corresponds to a fully occupied monolayer of gas on carbon [62]. So, in addition to the fit giving a less good description of the observation, the properties derived from the finite-length Warburg element are also less realistic for a hydrogen adsorption step. It was not possible to assign this part of the spectrum to a rate-limiting step in the membrane.

3.6 Discussion

3.6.1 Three, not two steps

The theoretical model (section 3.2) had three rate limiting steps, i.e. three arcs in the Nyquist plot. We allocated these in the Results section to (1) gas adsorption/diffusion in the electrode backing, (2) charge transfer at the catalyst, and (3) a step that involved proton hydration at the catalyst surface. Evidence for the first step was presented and discussed in our earlier work [62]. The present data give further support to this step, by the data that can be derived from Fig. 3.8. The second step is adopted in all similar investigations [30], while the third proposal about rate-limiting proton transfer at high frequencies is new. The experimental results gives support to the total model.

We may first note, that the results for the membrane resistance, R_m (Tables A.4, A.6 and A.7), confirm earlier investigations. The value is within a few percent reported earlier. The reduction in R_m with an increase of temperature from 20 to 45°C, was explained by Sone et al. [67] by the loss of water from the membrane at higher temperatures (see next section). The reproducibility of the experiments (cf. sections 3.5.2 and 3.5.3) allow several conclusions to be drawn.

The relaxation time of the third arc or the Gerischer element, did again (see [62]) not depend on the applied potential (see Tables A.7 and A.9) and it was also independent of the ageing effect. We expect that adsorption and diffusion of the hydrogen molecules along the surface of the carbon pores, is independent of ageing (or the Pt surface area, see below), and this is indeed observed, giving credence to this part of the interpretation. The hydrogen pressure variation in Y_0 is small (Fig. 3.8), and has a large uncertainty. Nevertheless, it is interesting to find that the diffusion coefficient that can be derived from the

slope is very near the one we estimated earlier [62], and which was used to support that reaction (3.1) takes place in the carbon matrix. The value, 1 x 10^{-7}m^2/s, is a likely value, as it is comparable with diffusion in the gas phase, and consistent with a fractional coverage of hydrogen on the carbon surface. A finite-length Warburg element, which give a similar mathematical form of the impedance, did not give a likely alternative explanation. The new evidence confirms our hypothesis of this step, that there is surface diffusion of hydrogen to the catalyst.

Support for the interpretation of next two steps is given from (1) the fits themselves, (2) the observed ageing effect, (3) the pressure effect, under the experimental conditions used.

The first arc (with highest frequency) had few signs of depression and the relaxation time was independent of the applied dc-potential. We had to use an ordinary capacitance and a resistance to model this arc. The fit was not perfect, but it was the only element that did not give an unphysical result (an α_{ct} value larger than unity in a fit to a constant phase element). In the fit of the second arc (the charge transfer step), a constant phase element was essential, however. It is likely that the charge transfer step, and not so much the proton hydration step, is affected by the surface heterogeneity and the applied potential. It is also likely that the heterogeneous nature of the surface becomes less important as the temperature rises, as evidenced by α_{ct}=1 for 50°C. So these variations are as expected for the chosen model.

We expect that an increase in the hydrogen pressure leads to an increased concentration of protons at the catalyst surface. The results in Table 3.1 support this idea because the charge transfer relaxation and the proton hydration relaxation depend on the hydrogen pressure. More protons at the surface may explain why both ρ_{ct} and T_{ct} increase in Table A.5. We have no clear explanation for the simultaneous reduction of ρ_{cm} and $C^{\mathrm{s}}_{\mathrm{H_3O^+}}$ in Table A.4. The formation of H_3O^+ is facilitated by the increased Γ_{H}, and this may have a bearing on ρ_{cm}.

We find it reasonable to relate the observed ageing effect to a reduction of the active catalyst (Pt) surface area. Such a reduction has been allocated to sintering or Pt particle agglomeration in the literature [52, 11]. Agglomeration and coalescence of Pt particles into larger ones will lower the surface-to-volume ratio. The sintering rate is strongly affected by the temperature [52, 11], and is therefore not so likely with the low temperatures used here. Another

explanation for a reduced active area may be the withdrawal of polymers from the surface sites.

Proton hydration as well as charge transfer, but not adsorption/diffusion, should depend on the catalyst surface area. A reduction of the surface area must make it more difficult for the reaction to proceed, and accordingly the resistance will increase. This is indeed seen in the data: The resistances of the two first steps increased with the number of experiments (Fig. 3.3). Further support to this interpretation may come from molecular dynamics simulations. These indicate that a water molecule has to be in the right position to catch the proton before it goes into the membrane [68].

Three arcs were observed also by Paganin et al. [29], Kim et al. [31], Freire et al. [40] and Schneider et al. [69] in the PEMFC, and water has also earlier been mentioned as playing a rate-limiting role. These authors assign the role of water to the low-frequency arc, however. They explain that water becomes rate-limiting because of diffusion of water through the membrane and support this by showing that this low-frequency arc disappears when a thinner membrane, as Nafion 115, is used. Our experimental conditions are such that concentration gradients in water are unlikely (see below). We have shown here and earlier [62] that the low-frequency arc support a Gerischer element for the carbon matrix. A finite-length Warburg element could not be equally well fitted and understood. Our interpretation of the low-frequency arc therefore disagrees with that of others [29, 31, 40]. The third arc is more sensitive to the temperature and hydrogen pressure than the other arcs.

In conclusion, we have presented theoretical and further experimental evidence to support rate-limiting surface diffusion of hydrogen to the catalytic site before charge transfer, and a rate-limiting step for proton hydration of water. A closer look on the state of water in the fuel cell membrane is now interesting.

3.6.2 Water in the fuel cell membrane

The performance of the polymer electrolyte membrane fuel cell depends on the water management in the system. The condition of the Nafion membrane is an important factor for this performance. Nafion is a proton conducting membrane based on a perfluorosulfonic acid (PFSA) polymer. It consists of a polytetrafluoroethylene (PTFE) backbone with side chains terminating in $SO_3^-H^+$ groups . The water content in the membrane, λ, is given by the number of water molecules per sulfonic acid group [44]. The water uptake in

the Nafion membrane depends strongly on the pre-treating procedure [70] and operational procedures. Nafion 117 membranes used in these experiments were rinsed and then boiled in pure water. The membranes were always stored in water and they never dried out. That gave us an expanded uniform membrane that was filled with water at all times (E-form) before mounting the MEA.

The MEAs were exposed to a varying applied potential. The small current densities that were used in Tables 3.2 and 3.3, can not cause a significant variation in the water content around the electrodes in one experiment, however. Diffusion of water is therefore *not* important for the experiment, since the water concentration can be expected to be uniform. This was one reason why we were able to allocate the high frequency arc to proton hydration, and exclude water diffusion as an explanation for he low frequency arc.

Two different states for water have been found in the membrane [71, 72]. When the membrane surface is in contact with saturated water vapour, the membrane can be treated as a single homogeneous phase, in which water dissolves and can move due to a concentration gradient [71]. When the membrane surface is in contact with liquid water, the membrane can be treated as a heterogeneous porous medium in which water can move also by convection, for instance in the presence of hydraulic pressure gradient [72]. In the present case with hydrogen electrodes only, we can regard the membrane phase as being homogeneous. This was the background for using the hydronium ion in the theoretical model, equivalent to a water transference number of unity [64]. This does not mean that exactly one water molecule will hydrate the proton. We have taken only one water along in our derivations, since the method is not good enough to tell the exact number of waters that are carried along.

Broka and Ekdunge [73] found that water uptake in a membrane exposed to saturated water vapour decreased with increasing temperature, and that the decrease was dramatic in the temperature range 25-50°C. Also Hinatsu et al. [74] published water sorption data that showed lower water uptakes at 80°C (λ=10) than at 18-30°C (Zawodzinski et al. [75]). Rieke et al. [76] measured water content and reported that the membrane had the highest water content at 30°C (λ=15) and lower at 50, 75 and 95°C (9, 6, and 11, respectively). We can therefore expect a dramatic change in water content when the temperature changes from 30 to 50°C in our experiments. The change in the properties $C_{H_3O^+}$ and ρ_{cm} with temperature may reflect this change.

We need to explain why proton hydration becomes considerably slower (Tables 3.2 and 3.3) at the higher temperature. The large variation in water content

may explain this. The smaller the water content is, the more difficult becomes the hydration step, and the higher is the relaxation time for this step. The data in Tables 3.2 and 3.3 have such a variation. The relaxation time, τ_{cm}, shows only a very weak dependence on the current density at 50°C, and no dependency at 30°C. A reduction in water content, may thus explain why the third rate-limiting step, $H^+ \cdot (t_{H_2O}\ H_2O)$, became less visible in the Nyquist diagram 50°C.

3.7 Conclusion

Electrochemical impedance spectroscopy was performed of the fuel cell electrode E-TEK, Elat/Std/DS/V2 0.5 mg Pt/cm^2, 20% Pt/C, with 0.6 mg Nafion/cm^2 (5 wt% solution). The membrane contact was Nafion 117 and the cell area was 4.91 cm^2. The electrode was studied at 30 and 50°C. The pressure was varied between 1 and 4 bar and the applied dc potential varied from 0 to 0.06 V. The results were interpreted by three reaction steps. The first is a slow adsorption/diffusion step supported by a best fit to a Gerischer element, independent of ageing and applied potential, with a surface diffusion coefficient of hydrogen of 1x10^{-7}m^2/s. The second, the well established charge transfer step, depends on ageing (catalyst surface area) and temperature as expected. The third step was given a new interpretation, as a rate-limiting proton hydration step. A large reduction in membrane water content at high temperatures increases the relaxation time of this step, and can explain why it then coincides with the second semicircle. By extending the temperature range of the investigation, one may earn more about the mechanism of the electrode reaction.

Acknowledgements

A.K. Meland is grateful to Nordic Energy Research and Norsk Hydro ASA for financial support. Rune Halseid is thanked for several constructive comments.

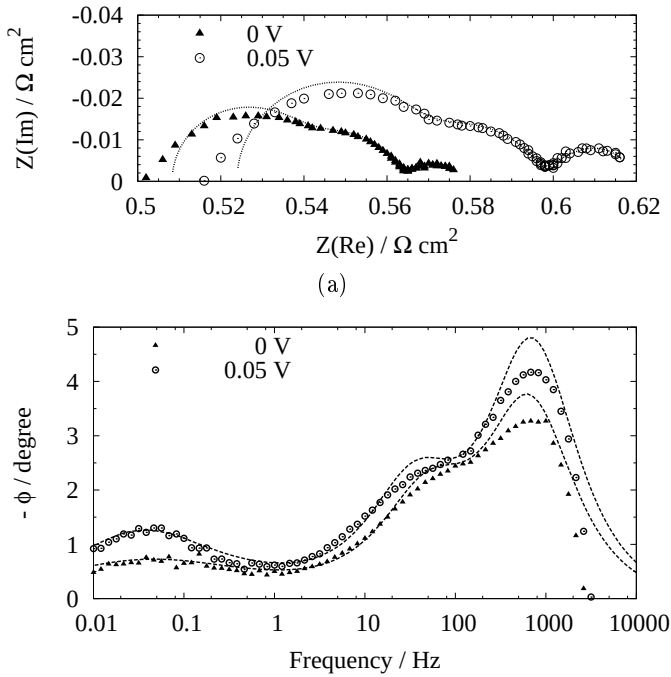

Figure 3.4. The impedance spectrum of a symmetrical H_2/H_2 cell at $p_{H_2} = 1$ bar and T=30° C. (a) Nyquist plot. (b) Phase shift plot. Points are experimental data and lines are data fitted with the equivalent circuit of Fig. 3.2.

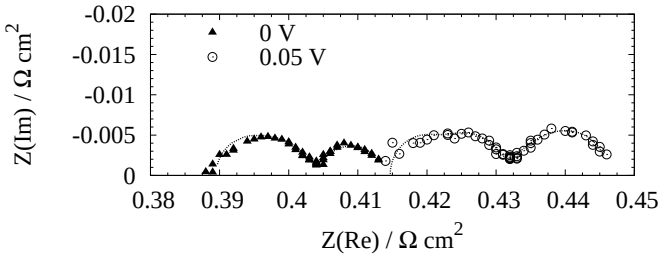

(a)

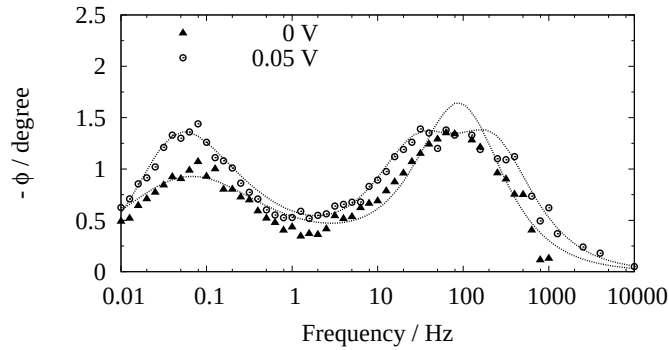

(b)

Figure 3.5. Impedance spectrum of a symmetrical H_2/H_2 cell at p_{H_2} = 1 bar and T=50°C. (a) Nyquist plot. (b) Phase shift plot. Points are experimental data and lines are data fitted with the equivalent circuit of Fig. 3.2.

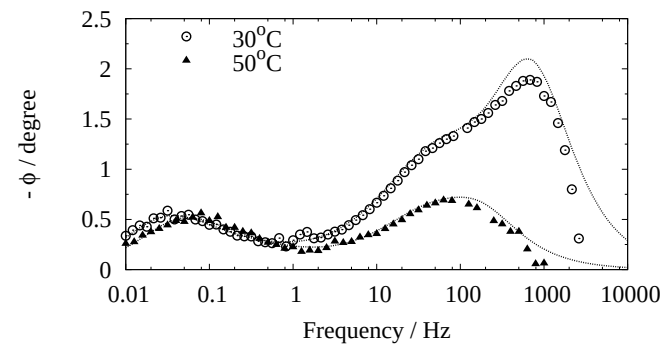

Figure 3.6. The phase shift plot for the unpolarised symmetric cell at T=30 and 50°C and p_{H_2} = 1 bar. Points are experimental data and lines are data fitted with the equivalent circuit of Fig. 3.2.

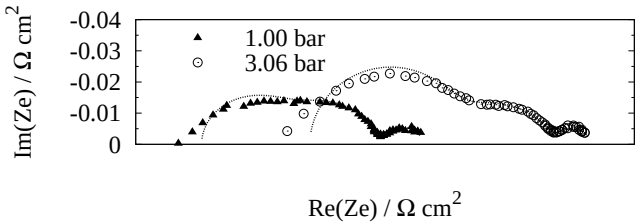

(a)

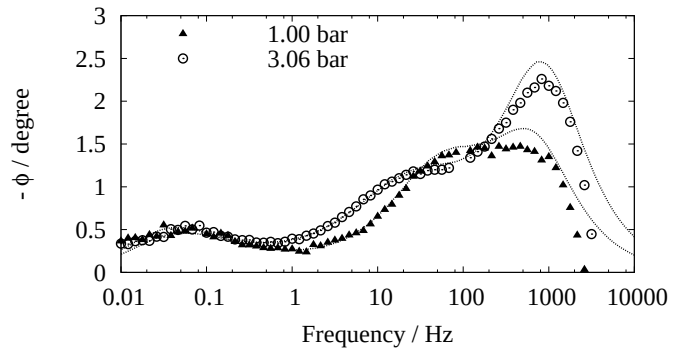

(b)

Figure 3.7. The impedance spectrum for the unpolarised symmetric cell at $T=30°C$. (a) Nyquist plot. (b) Phase shift plot. Points are experimental data and lines are data fitted with the equivalent circuit of Fig. 3.2.

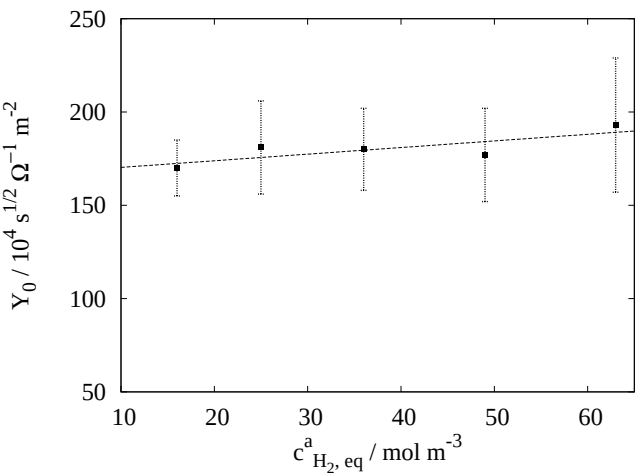

Figure 3.8. The admittance of equation (3.17) as a function of the hydrogen concentration in the gas phase. The error-bars of the single experiments are shown.

A.1 Appendix 1. The surface impedance

A.1.1 Mass and energy balances of the three steps

The mass balances and the polarisation of the surface follow from the three steps presented in section 3.2.

At the surface there is an adsorption of protons, Γ_{H^+}, hydronium ions, $\Gamma_{H_3O^+}$, and electrons, Γ_{e^-}. We take the catalyst surface to be electroneutral, by choosing its thickness such that the total adsorptions (in mol/m^2) of positive ions is equal to the adsorption of electrons:

$$\Gamma_{H^+} + \Gamma_{H_3O^+} = \Gamma_{e^-} \tag{A.21}$$

In the discussion of the properties of the surface it is convenient to use the polarisation of the surface. In this case there are two contributions to this polarisation, one is due to proton-electron pairs and the other is due to hydronium ion-electron pairs. As mentioned before, the extension of the surface is such that these pairs are contained. Together they make the interface electroneutral. The number of moles of the proton-electron dipoles per unit of surface area is given by Γ_{H^+} and for the hydronium ion-electron dipoles by $\Gamma_{H_3O^+}$.

The charge transfer (ct) reaction, Eq. (3.3), increases the number of adsorbed dipoles of the first kind while the proton hydration (cm), Eq. (3.4), reaction decreases it. We therefore have

$$\frac{d}{dt}\Gamma_{H^+} = r^s_{ct} - r^s_{cm} \tag{A.22}$$

where r^s_{ct} and r^s_{cm} refer to the reaction rates. Superscript s indicates a property of the surface. Similarly the cm reaction increases the number of dipoles of the second kind while the electric current decreases it. This gives

$$\frac{d}{dt}\Gamma_{H_3O^+} = r^s_{cm} - t_{H_2O}\frac{j}{F} \tag{A.23}$$

where F is Faraday's constant. The surface polarisation in the direction normal to the surface is equal to the sum of the polarisations due to the two dipole layers. These polarisations are equal to the dipole concentration times Faraday's constant times the average distances, $d^s_{H^+}$ and $d^s_{H_3O^+}$, between the charges

$$P^s = P^s_{H^+} + P^s_{H_3O^+} = F d^s_{H^+}\Gamma_{H^+} + F d^s_{H_3O^+}\Gamma_{H_3O^+} \tag{A.24}$$

There is no reason to assume that the average distance between both kind of positive ions and the excess electron layer is the same. For the interface, we assume that these average distances are constants independent of the ion densities. It therefore follows from Eqs. (A.22)-(A.24) that

$$r^{\mathrm{s}}_{\mathrm{ct}} = r^{\mathrm{s}}_{\mathrm{cm}} + \frac{1}{F d^{\mathrm{s}}_{\mathrm{H^+}}} \frac{d}{dt} P^{\mathrm{s}}_{\mathrm{H^+}} \tag{A.25}$$

The surface polarisation divided by the surface thickness gives a corresponding potential difference times a capacitance. For the two contributions to the total polarisation we have: $C^{\mathrm{s}}_{\mathrm{H^+}}$ and $C^{\mathrm{s}}_{\mathrm{H_3O^+}}$, of these two dipole layers

$$\frac{P^{\mathrm{s}}_{\mathrm{H^+}}}{d^{\mathrm{s}}_{\mathrm{H^+}}} = C^{\mathrm{s}}_{\mathrm{H^+}} \Delta_{\mathrm{s}} \phi \quad \text{and} \quad \frac{P^{\mathrm{s}}_{\mathrm{H_3O^+}}}{d^{\mathrm{s}}_{\mathrm{H_3O^+}}} = C^{\mathrm{s}}_{\mathrm{H_3O^+}} \Delta_{\mathrm{s}} \phi \tag{A.26}$$

Hydronium ions are present inside the surface as well as in the membrane. The potential difference between the membrane phase and the electron layer is the full potential difference $\Delta_{\mathrm{s}}\phi$ across the surface. The protons are closer to the electron layer, so that the potential difference between this layer and the electron layer $\Delta_{\mathrm{s,m}}\phi$ is smaller.

The rates of the three steps become, using Eq. (A.25),

$$r^{\mathrm{s}}_{\mathrm{ct,dc}} = \frac{r^{\mathrm{s}}_{\mathrm{cm,dc}}}{t_{\mathrm{H_2O}}} = \frac{1}{F} j_{\mathrm{dc}} \tag{A.27}$$

and

$$r^{\mathrm{s}}_{\mathrm{ct,ac}} = \frac{r^{\mathrm{s}}_{\mathrm{cm,ac}}}{t_{\mathrm{H_2O}}} + \frac{i\omega P^{\mathrm{s}}_{\mathrm{H^+,ac}}}{F d^{\mathrm{s}}_{\mathrm{H^+}}} \quad \text{and} \quad r^{\mathrm{s}}_{\mathrm{cm,ac}} = \frac{1}{F} \left(t_{\mathrm{H_2O}} j_{\mathrm{ac}} + \frac{i\omega P^{\mathrm{s}}_{\mathrm{H_3O^+,ac}}}{d^{\mathrm{s}}_{\mathrm{H_3O^+}}} \right) \tag{A.28}$$

We shall need the reaction Gibbs energy of the adsorption reaction (3.1):

$$\Delta_r G^{\mathrm{s}}_{\mathrm{ad}} = \frac{1}{2} \left(\mu^{\mathrm{a}}_{\mathrm{H_2}} - \mu^{\mathrm{g}}_{\mathrm{H_2}} \right) \equiv \frac{1}{2} \mu^{\mathrm{a}}_{\mathrm{H_2}}(x=0) - \frac{1}{2} \mu^{\mathrm{g}}_{\mathrm{H_2}} \tag{A.29}$$

Here $x = 0$ indicates the position of the surface. The chemical potential of hydrogen molecules just outside the surface and at the surface are the same, $\mu^{\mathrm{s}}_{\mathrm{H_2}} = \mu^{\mathrm{a}}_{\mathrm{H_2}}(x=0)$. The hydrogen gas in the experiment has a constant (position and time independent) pressure, leading to a constant $\mu^{\mathrm{a}}_{\mathrm{H_2}}$ as well as constant $c^{\mathrm{a}}_{\mathrm{H_2}}$. In the description of the electrochemical processes at the surface,

we use the change in Gibbs energy at the surface due to the neutral species. For the ct reaction (Eq. 3.3) we have:

$$\Delta_n G^{\mathrm{s}}_{\mathrm{ct}} = -\frac{1}{2}\mu^{\mathrm{s}}_{\mathrm{H_2}} \equiv -\frac{1}{2}\mu^{\mathrm{a}}_{\mathrm{H_2}}(x=0) \tag{A.30}$$

and for the cm reaction (3.4) we have:

$$\Delta_n G^{\mathrm{s}}_{\mathrm{cm}} = -\mu^{\mathrm{s}}_{\mathrm{H_2O}} \equiv -\mu^{\mathrm{m}}_{\mathrm{H_2O}}(x=0) \tag{A.31}$$

For the total electrode reaction, the contribution becomes:

$$\Delta_n G^{\mathrm{s}} = \Delta_r G^{\mathrm{s}}_{\mathrm{ad}} + \Delta_n G^{\mathrm{s}}_{\mathrm{ct}} + \Delta_n G^{\mathrm{s}}_{\mathrm{cm}} = -\frac{1}{2}\mu^{\mathrm{g}}_{\mathrm{H_2}} - \mu^{\mathrm{m}}_{\mathrm{H_2O}}(x=0) \tag{A.32}$$

A.1.2 The entropy production and the impedance

In order to derive the impedance of the model in section 3.2, we consider again our surface in Fig. 3.1. The excess entropy production rate of the surface, σ^{s}, contains the information about the surface dynamics. For isothermal conditions, the contributions to σ^{s} due to the alternating fields are [50]:

$$\begin{aligned} T\sigma^{\mathrm{s}}_{\mathrm{ac}} &= -j_{\mathrm{ac}}\Delta_{\mathrm{s}}\phi_{\mathrm{ac}} + i\omega P^{\mathrm{s}}_{\mathrm{H^+,ac}}\left(\frac{D^{\mathrm{s}}_{\mathrm{H^+,ac}} - D^{\mathrm{s}}_{\mathrm{H^+},eq}}{\varepsilon_0}\right) - r^{\mathrm{s}}_{\mathrm{ct,ac}}\Delta_n G^{\mathrm{s}}_{\mathrm{ct,ac}} \\ &\quad + i\omega P^{\mathrm{s}}_{\mathrm{H_3O^+,ac}}\left(\frac{D^{\mathrm{s}}_{\mathrm{H_3O^+,ac}} - D^{\mathrm{s}}_{\mathrm{H_3O^+},eq}}{\varepsilon_0}\right) - r^{\mathrm{s}}_{\mathrm{cm,ac}}\Delta_n G^{\mathrm{s}}_{\mathrm{cm,ac}} \end{aligned} \tag{A.33}$$

where $D^{\mathrm{s}}_{\mathrm{H^+,ac}}$ and $D^{\mathrm{s}}_{\mathrm{H_3O^+,ac}}$ are the displacement fields for the distribution of the two dipoles and ε_0 is the dielectric constant of vacuum. The equilibrium displacement fields are zero for free charges, $D^{\mathrm{s}}_{\mathrm{H^+,eq}} = D^{\mathrm{s}}_{\mathrm{H_3O^+,eq}} = 0$. The displacement fields are given by

$$D^{\mathrm{s}}_{\mathrm{H^+,ac}} = -\varepsilon_0\frac{\Delta_{\mathrm{s,H^+}}\phi_{\mathrm{ac}}}{d^{\mathrm{s}}_{\mathrm{H^+}}} \quad \text{and} \quad D^{\mathrm{s}}_{\mathrm{H_3O^+,ac}} = -\varepsilon_0\frac{\Delta_{\mathrm{s}}\phi_{\mathrm{ac}}}{d^{\mathrm{s}}_{\mathrm{H_3O^+}}} \tag{A.34}$$

The reaction Gibbs energies were defined above, Eqs. (A.29)-(A.32). For ac conditions we have:

$$\begin{aligned} \Delta_r G^{\mathrm{s}}_{\mathrm{ad,ac}} &= -\Delta_n G^{\mathrm{s}}_{\mathrm{ct,ac}} = \frac{1}{2}\mu^{\mathrm{a}}_{\mathrm{H_2,ac}}(x=0) \\ \Delta_n G^{\mathrm{s}}_{\mathrm{cm,ac}} &= \Delta_n G^{\mathrm{s}}_{\mathrm{ac}} = 0 \end{aligned} \tag{A.35}$$

Using Eq. (A.28) for the ac contributions one obtains

$$Fr^{\mathrm{s}}_{\mathrm{ct,ac}} = Fr^{\mathrm{s}}_{\mathrm{cm,ac}} + \frac{i\omega P^{\mathrm{s}}_{\mathrm{H^+,ac}}}{d^{\mathrm{s}}_{\mathrm{H^+}}} \quad \text{and} \quad Fr^{\mathrm{s}}_{\mathrm{cm,ac}} - \frac{i\omega P^{\mathrm{s}}_{\mathrm{H_3O^+,ac}}}{d^{\mathrm{s}}_{\mathrm{H_3O^+}}} = t_{\mathrm{H_2O}} j_{\mathrm{ac}} \tag{A.36}$$

Substituting this into Eq. (A.33) and using Eq. (A.35) we obtain

$$\begin{aligned} T\sigma^{\mathrm{s}}_{\mathrm{ac}} &= -r^{\mathrm{s}}_{\mathrm{cm,ac}}\left(F\Delta_{\mathrm{s}}\phi_{\mathrm{ac}} - F\Delta_{\mathrm{s,H^+}}\phi_{\mathrm{ac}}\right) \\ &\quad -r^{\mathrm{s}}_{\mathrm{ct,ac}}\left(F\Delta_{\mathrm{s,H^+}}\phi_{\mathrm{ac}} - \Delta_r G^{\mathrm{s}}_{\mathrm{ad,ac}}\right) \end{aligned} \tag{A.37}$$

Since the two reactions occur consecutively, the coupling of the reactions may be neglected. The theory of non-equilibrium thermodynamics then prescribes that the forces and the fluxes are related by

$$\begin{aligned} \Delta_{\mathrm{s,m}}\phi_{\mathrm{ac}} - \frac{1}{F}\Delta_r G^{\mathrm{s}}_{\mathrm{ad,ac}} &= -\rho^{\mathrm{s}}_{\mathrm{ct}} F r^{\mathrm{s}}_{\mathrm{ct,ac}} \\ \Delta_{\mathrm{s}}\phi_{\mathrm{ac}} - \Delta_{\mathrm{s,m}}\phi_{\mathrm{ac}} &= -\rho^{\mathrm{s}}_{\mathrm{cm}} F r^{\mathrm{s}}_{\mathrm{cm,ac}} \end{aligned} \tag{A.38}$$

where $\rho^{\mathrm{s}}_{\mathrm{ct}}$ and $\rho^{\mathrm{s}}_{\mathrm{cm}}$ are the resistivities of the ct and cm reactions. The electrochemical reaction rates are normally not related to their driving forces by linear relations. In this experiment, the alternating contribution to the forces are small (± 5 mV), however, so that we can use the linear theory. Adding the two relations in Eq. (A.38) one obtains

$$\Delta_{\mathrm{s}}\phi_{\mathrm{ac}} - \frac{1}{F}\Delta_r G^{\mathrm{s}}_{\mathrm{ad,ac}} = -\rho^{\mathrm{s}}_{\mathrm{ct}} F r^{\mathrm{s}}_{\mathrm{ct,ac}} - \rho^{\mathrm{s}}_{\mathrm{cm}} F r^{\mathrm{s}}_{\mathrm{cm,ac}} \tag{A.39}$$

The adsorption-diffusion layer has an impact on $\Delta_{\mathrm{s}}\phi_{\mathrm{ac}}$, because this layer determines the chemical potential of hydrogen at position $x = 0$. The resistivity is independent of the driving force, but can depend on the temperature and the polarisation induced by the dc-field.

The dc contribution to the excess entropy production rate is found using $\omega = 0$ and $j_{\mathrm{dc}} = F r^{\mathrm{s}}_{\mathrm{ct,dc}} = F r^{\mathrm{s}}_{\mathrm{cm,dc}}$. This gives

$$T\sigma^{\mathrm{s}}_{\mathrm{dc}} = -j_{\mathrm{dc}}\left[\Delta_{\mathrm{s}}\phi_{\mathrm{dc}} + \frac{1}{F}\left(t_{\mathrm{H_2O}}\ \Delta_n G^{\mathrm{s}}_{\mathrm{cm,dc}} + \Delta_n G^{\mathrm{s}}_{\mathrm{ct,dc}}\right)\right] \tag{A.40}$$

For small dc-currents the linear law is thus:

$$\Delta_{\mathrm{s}}\phi_{\mathrm{dc}} + \frac{1}{F}\left(t_{\mathrm{H_2O}}\ \Delta_n G^{\mathrm{s}}{}_{\mathrm{cm,dc}} + \Delta_n G^{\mathrm{s}}_{\mathrm{ct,dc}}\right) = -\left(\rho^{\mathrm{s}}_{\mathrm{ct}} + \rho^{\mathrm{s}}_{\mathrm{cm}}\right) j_{\mathrm{dc}} \tag{A.41}$$

The impedance of the charge transfer and the proton hydration steps is defined as:

$$Z^{\mathrm{s}} \equiv -\frac{\Delta_{\mathrm{s}}\phi_{\mathrm{ac}}}{j_{\mathrm{ac}}} \tag{A.42}$$

We find the surface impedance by adding $\Delta_{\mathrm{r}} G_{\mathrm{ad,ac}} = -\Delta_{\mathrm{n}} G_{\mathrm{ct,ac}} = -Z_{\mathrm{ad}} F^2 r^{\mathrm{s}}_{\mathrm{ct,ac}}$ to Eq. (A.39). This gives:

$$\Delta_{\mathrm{s}}\phi_{\mathrm{ac}} + \frac{\Delta_n G^{\mathrm{s}}_{\mathrm{ac}}}{F} = \Delta_{\mathrm{s}}\phi_{\mathrm{ac}} = -\left(\rho^{\mathrm{s}}_{\mathrm{ct}} + Z^{\mathrm{s}}_{\mathrm{ad}}\right) F r^{\mathrm{s}}_{\mathrm{ct,ac}} - \rho^{\mathrm{s}}{}_{\mathrm{cm}} F r^{\mathrm{s}}_{\mathrm{cm,ac}} \qquad \text{(A.43)}$$

where we used Eq. (A.35). It furthermore follows from Eqs. (A.25) and (A.26) that

$$F r^{\mathrm{s}}_{\mathrm{ct}} = F r^{\mathrm{s}}_{\mathrm{cm}} + i\omega \mathrm{C}^{\mathrm{s}}_{\mathrm{H^+}} \Delta_{\mathrm{s,H^+}}\phi \quad \text{and} \quad F r^{\mathrm{s}}_{\mathrm{cm}} = j_{\mathrm{ac}} + i\omega \mathrm{C}^{\mathrm{s}}_{\mathrm{H_3O^+}} \Delta_{\mathrm{s}}\phi \qquad \text{(A.44)}$$

These equations can now be combined to give the impedance presented in section 3.3.

A.2 Appendix 2

Table A.4. Fitted results for the first semi-circle for the symmetric, unpolarised cell at T=30° C and various hydrogen gas pressures.

p_{H_2} (bar)	R_m (Ω cm^2)	$C^s_{H_3O^+}$ (s/Ω cm^2)	$\rho_{cm} \pm 0.001$ (Ω cm^2)
1.00	0.53	0.0087±0.0001	0.030
1.56	0.55	0.0050±0.0003	0.041
2.25	0.55	0.0044±0.0002	0.044
3.06	0.56	0.0040±0.0002	0.048
4.00	0.56	0.0038±0.0001	0.049

Table A.5. Fitted results for the second and third arc for the symmetric, unpolarised cell at T=30° C and various gas pressures

p_{H_2} (bar)	T_{ct} (s^α/Ω cm^2)	α_{ct}	$\rho_{ct} \pm 0.002$ (Ω cm^2)	Y_0 ($s^{1/2}/\Omega$ cm^2)	τ_{ad} (s)
1.00	0.30±0.07	0.85±0.06	0.023	170±15	6
1.56	0.42±0.10	0.81±0.06	0.028	181±25	6
2.25	0.55±0.10	0.79±0.05	0.030	180±22	6
3.06	0.74±0.15	0.75±0.05	0.031	177±25	6
4.00	0.93±0.19	0.70±0.05	0.033	193±32	6

Table A.6. Fitted results for the first arc for the symmetric cell at $T = 30°C$, 1 bar hydrogen gas pressure and different applied voltages.

$\Delta\phi_{dc}$ (mV)	R_m (Ω cm^2)	$C_{H_3O^+}$ (s/Ω cm^2)	$\rho_{cm} \pm 0.001$ (Ω cm^2)
0	0.51	0.0071±0.0004	0.035
10	0.53	0.0061±0.0003	0.038
20	0.53	0.0057±0.0003	0.041
30	0.53	0.0053±0.0002	0.044
50	0.53	0.0049±0.0003	0.047
60	0.54	0.0047±0.0002	0.050

Table A.7. Fitted results for the second and third arc for the symmetric cell at $T = 30°C$, 1 bar hydrogen gas pressure and different applied potentials

$\Delta\phi_{dc}$ (mV)	T_{ct} (s^α/Ω cm^2)	α_{ct}	ρ_{ct} (Ω cm^2)	Y_0 ($s^{1/2}/\Omega$ cm^2)	τ_{ad} (s)
0	0.46±0.10	0.83±0.06	0.020±0.002	194±21	6
10	0.49±0.11	0.80±0.05	0.023±0.002	181±16	8
20	0.41±0.08	0.84±0.05	0.023±0.001	156±11	8
30	0.47±0.09	0.82±0.05	0.025±0.001	154±11	8
50	0.47±0.12	0.82±0.06	0.026±0.002	131±11	8
60	0.50±0.12	0.82±0.06	0.026±0.002	122±10	8

Table A.8. Fitted results for the first arc for the symmetric cell at $T = 50°C$, 1 bar hydrogen gas pressure and different applied voltages.

$\Delta\phi_{dc}$ (mV)	R_m (Ω cm^2)	$C_{H_3O^+} \pm 0.01$ (s/Ω cm^2)	$\rho_{cm} \pm 0.001$ (Ω cm^2)
0	0.39	0.11	0.009
10	0.40	0.11	0.009
20	0.40	0.10	0.009
30	0.41	0.09	0.009
50	0.42	0.08	0.010
60	0.42	0.06	0.010

Table A.9. Fitted results for the second and third arc for the symmetric cell at $T = 50°C$, 1 bar hydrogen gas pressure and different applied potentials

$\Delta\phi_{\mathrm{dc}}$ (mV)	T_{ct} (s^{α}/Ω cm^2)	α_{ct}	ρ_{ct} (Ω cm^2)	Y_0 ($s^{1/2}/\Omega$ cm^2)	τ_{ad} (s)
0	1.9±0.8	0.86±0.14	0.005±0.001	221±10	5
10	1.5±0.6	0.83±0.14	0.005±0.002	184±6	5
20	1.2±0.5	0.87±0.13	0.005±0.002	170±5	5
30	0.73±0.14	0.97±0.06	0.006±0.001	163±3	5
50	0.79±0.19	0.99±0.07	0.006±0.001	147±4	5
60	0.75±0.19	0.97±0.07	0.007±0.001	138±4	5

Chapter 4

Three steps in the anode reaction of the polymer electrolyte membrane fuel cell. The effect of CO

Anne-Kristine Meland and Signe Kjelstrup

Department of Chemistry
Norwegian University of Science and Technology,
N-7491 Trondheim, Norway

This paper has been accepted
J. Electroanal. Chem.

Abstract

We studied the influence of CO poisoning of the anode in the polymer electrolyte membrane fuel cell (PEMFC) using electrochemical impedance spectroscopy (EIS). The anode impedance was found by first feeding neat hydrogen gas and next hydrogen with CO into one of the electrodes, keeping neat hydrogen gas on the other electrode as a reference. The electrodes were E-TEK Elat gas diffusion electrodes with 0.5 mg Pt/cm^2, and the membrane was Nafion 117. The CO concentration was 103 ppm, and the total pressures were 1, 2.5 and 4 bar. Operating temperatures were kept constant, 30.0 or 50.0 $\pm$ 0.1°C. Bias voltages of 0 and 0.05 V were used. Three steps were revealed in the reaction mechanism, the slow adsorption/diffusion step, the charge transfer step and the proton hydration step, confirming earlier results. Carbon monoxide affects the charge transfer step by blocking active sites and by affecting the surface polarisation. We further conclude that CO adsorbs to the porous carbon matrix, and reduces significantly the rate of surface diffusion of hydrogen to the surface.

4.1 Introduction

In the polymer electrolyte membrane fuel cell (PEMFC), the largest overpotential is encountered at the oxygen electrode, the cathode, but this is only when the feed to the anode is neat hydrogen. When hydrogen contains small amounts of CO (around 100 ppm), as is the case when it is produced by reformer technology, the anode will be poisoned, and the anode overpotential becomes larger [77, 78]. It is believed that CO occupies the Pt sites and affects hydrogen adsorption by lowering the accessible surface [11, 12]. In addition, CO lowers the reactivity of the uncovered sites by dipole interaction and electron capture [79]. It is thus important to understand the anode under normal conditions and when it is poisoned with CO. Our aim here is to study the dynamic response of the anode for these conditions. A theoretical model that describe the rate limiting processes at the anode was thus developed earlier [62, 80], distinguishing between the transport up to the catalyst, at the catalytic site and from this site into the membrane.

Various porous gas-diffusion electrode models that also have been used for the PEMFC, have developed since the late 1960's [21, 22, 23]. Most of these models have treated the electrodes in their steady state [24, 25, 26]. The dynamic response of the system, the topic of this investigation, was also studied [27, 28].

Most of the focus has been on the oxygen electrode since this contributes most to the losses in the PEMFC in normal operation.

In two previous articles [62, 80] we investigated the anode reaction with electrochemical impedance spectroscopy (EIS) and found three steps in the reaction mechanism. The anode reaction was investigated in a cell with two hydrogen electrodes. The cell temperature, applied potential and hydrogen gas pressure were varied. Three steps were revealed, most importantly because we used temperatures below 50°C. The steps are discussed in detail in the section that follows below. This work gives a good basis for investigations of the CO-effect.

EIS provides a simple way to separate the contribution of CO poisoning from the behaviour without CO, and evaluate the influence of other parameters [30, 31]. We shall use this technique here.

The purpose of this paper is to find how the three postulated steps [62, 80] in the PEMFC anode reaction are affected by the presence of CO. In order to again see all three steps, we shall continue to use (mainly) the lowest temperature that was used before (30°C). We shall again be able to document that three steps are present. Using the three steps as a premise, we shall see that presence of CO changes only one of the three relaxation times, and that the observed changes in relaxation time, resistances and other parameters, can all be explained by a large surface coverage of CO on Pt (near 0.9), by changes in the polarisation of the catalyst, and by CO adsorption onto the porous carbon. In this manner we shall therefore also present a model for the CO effect on the anode, that is consistent with our previous model, and with other documented effects of CO in the literature [31].

The article is organised as follows. We repeat first (section 4.2) the essentials of our previously published model for hydrogen oxidation in the porous anode of the PEMFC. The expressions derived for the impedance of the surface are also repeatesd. Experimental conditions and results are given in section 4.3. In order to confirm our experimental methods, we report also results for the complete fuel cell poisoned with CO. Similar results were obtained by others [31]. The CO concentration used here (103 ppm) was one that is normally present in the reformer gases after purification [77].

The Results section contain spectra and spectra details, mostly for the main temperature investigated, 30°C. In the tabulation of fitted parameters we compare the values of the poisoned electrode with the unpoisoned, before conclusions are drawn.

4.2 The three steps of the anode reaction

As mentioned above, we are testing a model reported earlier [62, 80], consisting of three rate-limiting steps for the oxidation of hydrogen in the PEMFC anode. The model assumes that hydrogen gas is first adsorbed at any position x along the pores in the carbon matrix leading up to the Pt catalyst:

$$\frac{1}{2}\mathrm{H_2(g)} \rightarrow \frac{1}{2}\mathrm{H_2(a)} \tag{4.1}$$

The reaction is reversible giving

$$r(x,t) = \frac{1}{2}k^{\mathrm{a}}_{\mathrm{H_2}}c^{\mathrm{g}}_{\mathrm{H_2}} - \frac{1}{2}k^{\mathrm{d}}_{\mathrm{H_2}}c^{\mathrm{a}}_{\mathrm{H_2}}(x,t) \tag{4.2}$$

where $k^{\mathrm{a}}_{\mathrm{H_2}}$ and $k^{\mathrm{d}}_{\mathrm{H_2}}$ are reaction rate constants for adsorption and desorption, respectively, while $c^{\mathrm{g}}_{\mathrm{H_2}}$ and $c^{\mathrm{a}}_{\mathrm{H_2}}$ are concentrations in the gas phase, and at the surface, respectively. Once adsorbed, hydrogen diffuses along the carbon surface to the platinum (to position $x = 0$) where it reacts according to the familiar Tafel-Volmer mechanism:

$$\mathrm{H_2(a)} \rightarrow 2\mathrm{H_{ads}} \tag{4.3}$$

$$\mathrm{H_{ads}} \rightarrow \mathrm{H^+(s)} + \mathrm{e^-(a)} \tag{4.4}$$

where (a) denotes the anode and (s) the platinum surface. The molecule dissociates into protons and electrons at active sites in the electrode surface of the platinum particles. Electrons are eventually transported into the carbon phase.

The protons bind on the average to one water molecule before they leave the surface [64, 65]. In the third rate-limiting step net charge moves into the cation exchange membrane (m) as hydronium ions:

$$\mathrm{H^+(s) + H_2O(m)} \rightarrow \mathrm{H^+H_2O(m)} \tag{4.5}$$

4.2.1 The equivalent circuit

For the first of these three steps we derived a Gerischer impedance, using non-equilibrium thermodynamics. The fit of the experimental data to this impedance was always better than a fit to the finite length Warburg impedance, the most likely alternative. The impedance of step 1, the step for adsorption and surface diffusion was given by [62]

$$Z_{\mathrm{ad}} = \frac{RT}{2F^2c^{\mathrm{a}}_{\mathrm{H_2,eq}}\sqrt{2Dk^{\mathrm{d}}_{\mathrm{H_2}}(1+i\omega\tau_{\mathrm{ad}})}} \tag{4.6}$$

where the relaxation time in the absorption process due to the chemical reaction (4.2):

$$\tau_{\mathrm{ad}} = \frac{2}{k^{\mathrm{d}}_{\mathrm{H_2}}} = \frac{2c^{\mathrm{a}}_{\mathrm{H_2,eq}}}{c^{\mathrm{g}}_{\mathrm{H_2}} k^{\mathrm{a}}_{\mathrm{H_2}}} \tag{4.7}$$

The hydrogen concentration in the pores, $c^{\mathrm{g}}_{\mathrm{H_2}}$, was constant in the experiment, giving also a constant value for the concentration of absorbed gas at equilibrium, $c^{\mathrm{a}}_{\mathrm{H_2,eq}}$.

The fit of the experimental results to the theoretical expressions gave furthermore Y_0 and τ_{ad} in the following expression for Z_{ad}:

$$Z_{\mathrm{ad}} = \frac{1}{Y_0\sqrt{\tau_{\mathrm{ad}}^{-1} + i\omega}} \tag{4.8}$$

The expression for the relaxation time, $\tau_{\mathrm{ad}}^{-1} = k^{\mathrm{d}}_{\mathrm{H_2}}/2$, is given in Eq. (4.7). The other variable, the admittance, is

$$Y_0 = \frac{2F^2}{RT} c^{\mathrm{a}}_{\mathrm{H_2,eq}} \sqrt{2Dk^{\mathrm{d}}_{\mathrm{H_2}}\tau_{\mathrm{ad}}} = \frac{4F^2}{RT} c^{\mathrm{a}}_{\mathrm{H_2,eq}} \sqrt{D} \tag{4.9}$$

This admittance Y_0 is proportional to the hydrogen concentration in the adsorbed phase. This concentration is, at equilibrium, proportional to the gas concentration of hydrogen, and such a proportionality was found [80]. The slope of Y_0 versus the concentration was used to estimate a diffusion constant for hydrogen along the surface, using the assumption $c^{\mathrm{a}}_{\mathrm{H_2,eq}} = c^{\mathrm{g}}_{\mathrm{H_2,eq}}$, or $k^{\mathrm{a}}_{\mathrm{H_2}} = k^{\mathrm{d}}_{\mathrm{H_2}}$. This admittance did not depend on the applied bias potential.

The theoretical expression for the impedance of the whole surface was found as

$$Z^{\mathrm{s}} = \frac{\rho^{\mathrm{s}}_{\mathrm{cm}} + Z_{\mathrm{ct}}}{1 + i\omega C^{\mathrm{s}}_{\mathrm{H_3O^+}} (\rho^{\mathrm{s}}_{\mathrm{cm}} + Z_{\mathrm{ct}})} \tag{4.10}$$

In this equation, Z_{ct} is the impedance of the charge transfer step

$$Z_{\mathrm{ct}} = \frac{\rho^{\mathrm{s}}_{\mathrm{ct}} + Z_{\mathrm{ad}}}{1 + i\omega C^{\mathrm{s}}_{\mathrm{H^+}} (\rho^{\mathrm{s}}_{\mathrm{ct}} + Z_{\mathrm{ad}})} \tag{4.11}$$

and the capacitance and the resistivity of the proton hydration are given by $C^{\mathrm{s}}_{\mathrm{H_3O^+}}$ and $\rho^{\mathrm{s}}_{\mathrm{cm}}$. The relaxation time for the proton hydration reaction, τ_{cm}, is

$$\tau_{\mathrm{cm}} = \rho_{\mathrm{cm}}\ C^{\mathrm{s}}_{\mathrm{H_3O^+}} \tag{4.12}$$

The experiments were done with gases and membrane saturated with water, excluding water diffusion as a rate-limiting step, at OCV conditions, and confirming the pure semi-circle appearance of this step.

Data fitted the theoretical expression well, provided that we allowed for a depression of the semicircle in the charge transfer step, by setting

$$C_{\mathrm{ct}} = T_{\mathrm{ct}}(i\omega)^{\alpha} \tag{4.13}$$

where α is independent of the frequency. The surface heterogeneity as expressed by the parameter α was constant. The relaxation time for the charge transfer step is [62]:

$$\tau_{\mathrm{ct}} = (T_{\mathrm{ct}}\rho_{\mathrm{ct}})^{1/\alpha} \tag{4.14}$$

The charge transfer step, the second step, depended on the applied potential much more than the other two steps, as one would expect. This part of the impedance, i.e. both $\rho^{\mathrm{s}}_{\mathrm{cm}}$ and $\rho^{\mathrm{s}}_{\mathrm{ct}}$ were sensitive to the catalyst ageing. In a previous article [62] we interpreted ageing as a reduction in surface area; giving a doubling of these resistances.

The equivalent circuit that was put up on the basis of these equations is given in Fig. 4.1. The sequencing of the contributions to the total spectrum is fixed, as there is no possibility to switch the elements of the circuit.

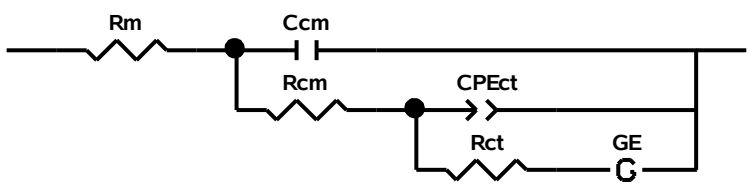

Figure 4.1. The equivalent circuit derived from non-equilibrium thermodynamics [62, 80] for the three rate-limiting steps of the anode of the polymer electrolyte fuel cell. The Gerischer impedance from adsorption/desorption and diffusion of hydrogen on carbon is denoted GE. The charge transfer step at a heterogeneous electrode surface contributes by R_{ct} and CPE_{ct} of a constant phase element (see text for definition), while the step that includes proton hydration gives the resistance R_{cm} and the capacitance C_{cm}. The Nafion membrane resistance is denoted R_{m}.

This model is taken as a premise in the present investigation. We shall see that it is possible to use it to explain the electrode behaviour also in the presence of

CO. While this does not prove that the model is the only possible explanation of the data; it does make it more plausible when the new experimental data can be explained in terms of the same model.

4.3 Experimental

4.3.1 Methods and materials

The electrode tested was a E-TEK Elat/Std/DS/V2 gas diffusion electrode with 0.5 mg Pt/cm^2 and 20% Pt/C on Vulcan XC-72. The electrode area was 4.91 cm^2.

To obtain a better ionic contact between the layers in the membrane- and electrode assembly (MEA) of the single cell, the electrodes were sprayed with a 5% Nafion solution to give 0.6 mg Nafion/cm^2. The MEA consisted of two identical electrodes separated by a Nafion 117 membrane. The membranes were pretreated in several steps as described for instance by Møller-Holst [51]. The mechanical pressure over the MEA was 4.2 barg, controlled by a pneumatic piston. The pressure and temperature were constant during each experiment within one percent variations.

The EIS measurements were done in an in-house fuel cell test station build by Møller-Holst [51] and modified by Vie [39]. The test station is also described in previous papers [62, 80]. The impedance diagrams were recorded using a PAR 263A/94 potentiostat and a Solartron 1260 FRA. The "Z-plot" software from Scribner Ass. Inc. was used to run the experiments. Measurements were made in a two-electrode set-up where the counter electrode which operated on neat H_2 also served as reference electrode. The impedance was obtained by sweeping over frequencies from 10 kHz to 10 mHz, recording 12 steps/decade, for each pressure. An amplitude of 5 mV was used in the experiments. The applied potentials was 0.05 V. All EIS spectra were fitted using the software "Z-View" (Scribner Associated Inc.) and are given as Nyquist plots of Z^{cell}.

Both cyclic voltammetry (CV) and stripping voltammetry was done at 30°C using a PAR 263A/94 potentiostat and "CorrWare" software from Scribner. The same cell was used as in the EIS experiments. In the CV experiments, the working electrode compartment was fed with pure N_2 and in the stripping voltammetry experiments it was fed with H_2+103 ppm CO. After the electrode had been equilibrated with CO, the working compartment was purged with N_2 for 2 hours before the CV experiments were done. The CO that remained on the surface was therefore chemisorbed. The scan rate was 20 mV/s.

4.3.2 EIS studies

1. Most experiments were performed at 30°C. At this temperature, we investigated the cell with pure hydrogen on both sides, and with hydrogen and 103 ppm CO on the working electrode, at 0 and 0.05 V applied dc voltage, and for three total gas pressures (1, 2.5 and 4 bar).

2. The experiments at 0 and 0.05 V applied dc voltage were repeated at 50°C and 1 bar.

3. The CO poisoning of the anode required time to come to equilibrium. At 30°C this time was approximately 2 hours. EIS measurements were done when the system was equilibrated, usually after 2 hours. The equilibration time was determined by recording the phase shift angle at 0 V and 100 Hz after admitting CO to the electrode compartment, see Figure 4.2 for a typical example, obtained at 30 °C. The time for equilibration was somewhat shorter at 50°C.

4. In order to be able to compare the experimental technique with that reported by other researchers, the EIS was also measured with a regular fuel cell with O_2 fed to the cathode and H_2 or H_2+103 ppm CO fed to the anode compartment. The applied dc voltages were 0 and 0.05 V.

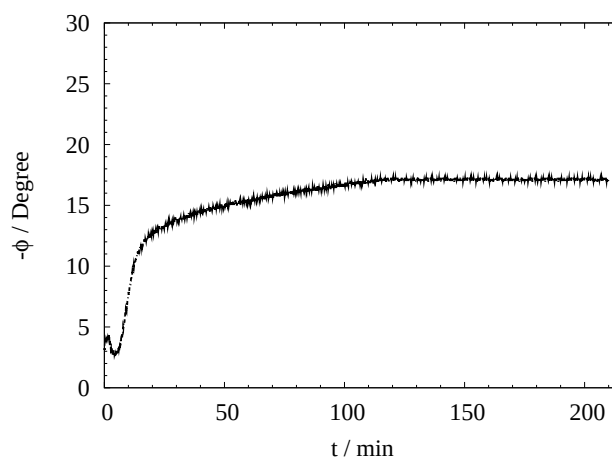

Figure 4.2. Phase angle variation with time as a clean electrode is flushed with 103 ppm CO in hydrogen gas at 1 bar, 100 Hz, 0.0 V and 30°C. A stable value is reached after 2 hours.

4.4 Results

4.4.1 The surface coverage

The stripping voltammogram for the electrode are shown in Figure 4.3. The CO coverage at 30°C was calculated from Fig. 4.3. The surface area below the peak corresponding to CO adsorption (0.6-0.9V) was integrated to give a surface charge of 48 mC/cm^2. Using the charge required to oxidise one monolayer CO on bright Pt (484 μC/cm^2) [81, 82], the surface area was calculated to 20 m^2 Pt/g Pt using the procedure explained in a previous article [80]. We found again the surface area of the unpoisoned electrode to be 22 m^2 Pt/g Pt. The chemisorbed layer of CO at 30°C has therefore a coverage of $\theta = 0.90$, giving a hydrogen coverage of 0.10. Both Felui et al. [81] and Weaver et al. [82] found a coverage of irreversibly adsorbed CO on platinum in aqueous sulphuric acid at room temperature of about 0.9. At 50°C, our CO coverage changes to 0.83. This compares well with Ciureanu and Wang [30] who obtained 0.85 at this temperature.

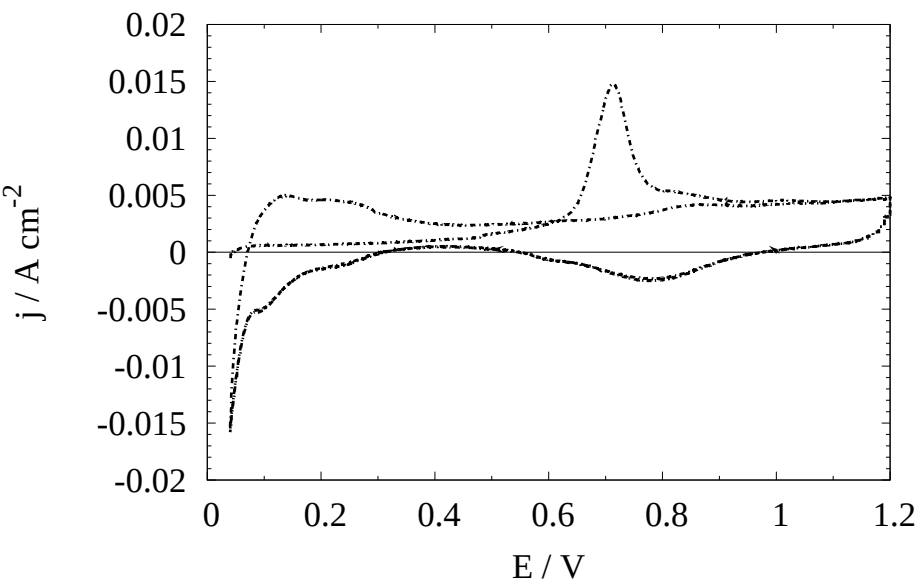

Figure 4.3. Stripping voltammogram obtained with a working electrode equilibrated 2 hours with H_2 + 103 ppm CO and subsequently flushed with N_2 for 2 hours before cycling. The temperature was 30°C and the scan rate was 20 mV/s.

4.4.2 The fuel cell spectra and the Nafion membrane resistance

An immediate control of the experimental set-up and the system was always provided by the Nafion membrane resistance derived from the spectra. This resistance has been recorded in the literature by many researchers [30, 31, 29, 40]. Our values were temperature dependent. They agreed with observations by Paganin et al. [29] and Freire et al. [40] and were reproducible within an error of ±5%, see Table 4.1.

The results from the fuel cell, with and without the poisoned electrode are shown in Fig. 4.4. We see the considerable change in the impedance spectra that also have been reported by others. We see the immediate change upon poisoning cited in the beginning of this article: While the main loss is associated to the cathode in Fig. 4.4a, it is associated with the anode in Fig. 4.4b.

Table 4.1. Parameters for the proton hydration step, obtained by fitting experimental data for the cell H_2/H_2+103 ppm CO to Eq. (4.10). The electrodes were equilibrated 2 hours before the experiment at 1 bar total pressure.

T (°C)	$\Delta\phi_{dc}$ (V)	R_m (Ω cm^2)	C^s_{cm} (s/Ω cm^2)	ρ_{cm} (Ω cm^2)
30	0.00	0.47	0.0029	0.11
30	0.05	0.50	0.0031	0.17
50	0.00	0.43	0.0079	0.15
50	0.05	0.42	0.0072	0.19

4.4.3 The spectra of the CO-poisoned electrode

The spectra of the anode equilibrated with 103 ppm CO and recorded at 30°C are shown in Fig. 4.5 for 0 and 0.05 V applied potential. The total resistance of the system increase with increasing bias potential. This is probably due to a change in Z_{ct}. Ciureanu and Wang [30] found that the total resistance in the CO poisoned hydrogen cell increased with increasing bias voltage at potentials below 0.3 V.

The first spectrum, repeated in Fig. 4.6, shows the fit of experimental data to the equivalent circuit in Fig. 4.1. Three rate-limiting processes can clearly be fitted. The high-frequency arc, to the left in the diagram, is again most pronounced at 30°C. The low frequency region fitted to the Gerischer impedance is shown in more detail in Fig. 4.7. The fit in this figure captures all data with a precision of a few per cent. In general the fits of step 1 and 2 were within

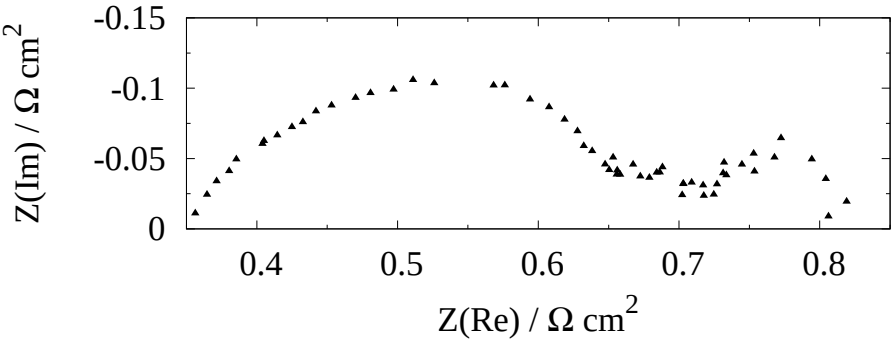

(a)

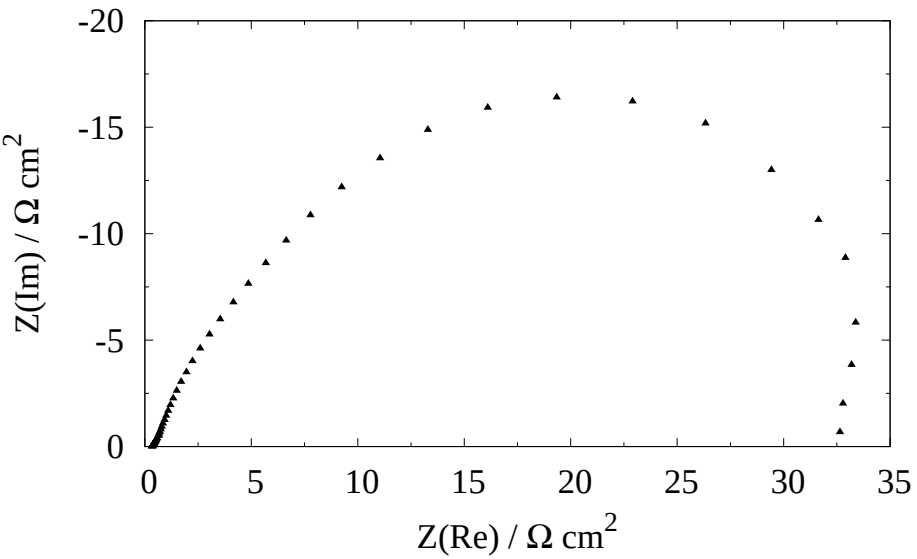

(b)

Figure 4.4. PEMFC impedance spectra at T=50° C, 1 bar and pure hydrogen and oxygen gas. (a) No CO present in the anode gas (b) 103 ppm CO present in the anode gas

5% and step 3 within 50%. Within these accuracies, there was no observable effect on the impedance by changing the pressure. Also there was no systematic variation in Y_0 with the pressure. The measurements at 50°C are shown in Fig. 4.8. The contribution from the unpoisoned electrode in the symmetrical hydrogen cell [62, 80] is negligible compared to the contribution from the CO poisoned hydrogen electrode.

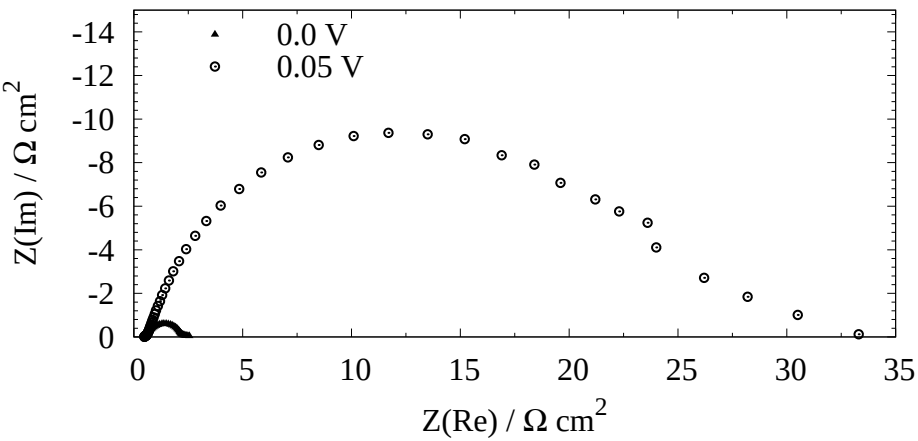

Figure 4.5. EIS of the H_2/H_2 + 103 ppm CO cell after 2 hours equilibration at 1 bar pressure and T=30°C, 0 and 0.05 V.

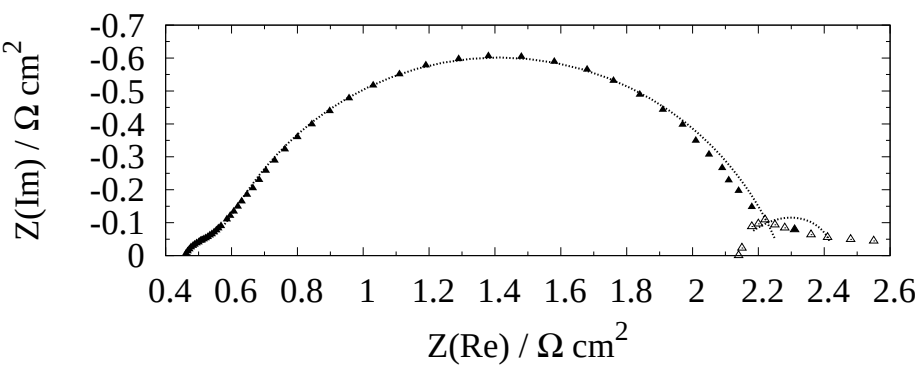

Figure 4.6. Detail of Fig. 4.5 for T=30°C and 0 V. The fit to the equivalent circuit 4.1 is shown and the superimposed area between the charge transfer part and the Gerischer part is split. The line is the fitted data.

The results of the data reduction from all fits are presented in Tables 4.1-4.3. The results for step 1 and 2 have an accuracy better than 5% while the accuracy for step three is better than 50% in all tables. Table 4.1 gives the characteristics of the proton hydration step. We see a significant variation in the parameters with applied potential and temperature. Table 4.2 gives the characteristic data for the charge transfer step and the Gerischer impedance. As we have found earlier, the factor α is remarkably constant. The potential has the greatest impact on the charge transfer step, T_{ct} and ρ_{ct}, but a systematic variation is also seen in the parameters of the Gerischer impedance, Y_0 and τ_{ad}.

The relaxation times for all three processes are given in Table 4.3. The table gives also their value relative to the value of the unpoisoned electrode (τ_{CO}/τ). The relative effect on Y_0 is tabulated in Table 4.2. From the change in impedance and temperature, we calculate from Eq. (4.9) that the surface diffusion coefficients are related by

$$D_{50,0V} = 8 \times D_{30} \tag{4.15}$$

$$D_{50,0.05V} = 28 \times D_{30} \tag{4.16}$$

The relative change in the diffusion coefficient with temperature and potential can be found, by assuming the surface concentration to be a temperature function only. Calculations gave then a 8 fold variation with a temperature change of 20°C at 0 V, and around a 30 fold variation at 0.05 V. The variation is large, and calls for a revision of the assumption.

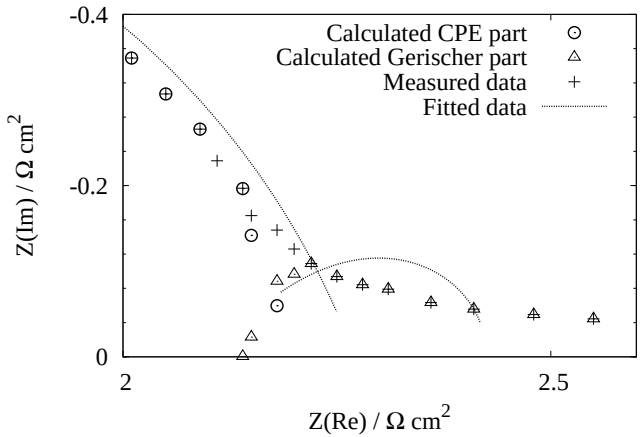

Figure 4.7. Enlargement of Fig. 4.5 showing the fit to the Gerischer impedance and the constant charge transfer element at T=30°C and 0 V. The superimposed part of the plot is split into the CPE part and the Gerischer part. The line is the fitted data.

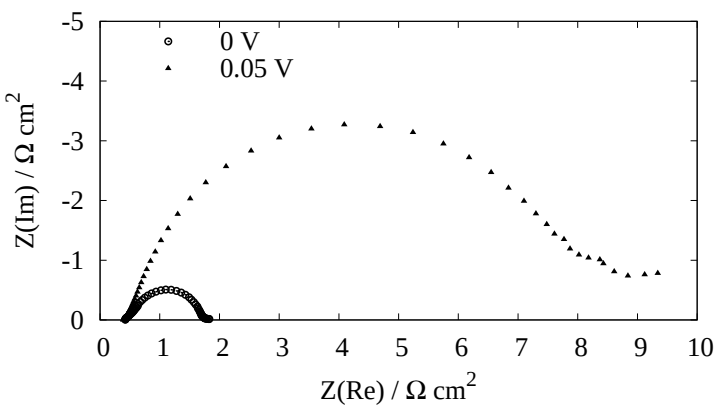

Figure 4.8. EIS of the cell H_2/H_2 + 103 ppm CO cell after 2 hours equilibration at 1 bar pressure and 50°C, 0 and 0.05 V.

Table 4.2. Parameters obtained for the constant phase element and the Gerischer impedance, by fitting experimental data for the cell H_2/H_2, 103 ppm CO to Eqs. (4.6), (4.8), (4.10), and (4.11). The electrodes were equilibrated 2 hours before the experiment at 1 bar total pressure. The admittance $Y_{0,\mathrm{rel}}$ gives the admittance relative to that of the unpoisoned electrode.

T (°C)	$\Delta\phi_{\mathrm{dc}}$ (V)	T_{ct} ($\mathrm{s}^{\alpha}/\Omega\mathrm{cm}^2$)	α_{ct}	ρ_{ct} ($\Omega\mathrm{cm}^2$)	Y_0 ($\mathrm{s}^{1/2}/\Omega\mathrm{cm}^2$)	$Y_{0,\mathrm{rel}}$	τ_{ad} (s)
30	0.00	0.079	0.77	1.69	6	0.032	4
30	0.05	0.041	0.83	24.8	0.3	0.0023	9
50	0.00	0.072	0.86	1.15	16	0.072	5
50	0.05	0.042	0.85	7.59	1.5	0.010	16

Table 4.3. Relaxation times for the three steps of the CO poisoned electrode of the cell H_2/H_2, 103 ppm CO. Gas diffusion electrodes were E-TEK Elat 0.5 mg Pt/cm^2 and a Nafion 117 membrane was used at 1 bar total pressure. Experimental conditions were $T = 30$ or 50°C and $E = 0$ or 0.05 V. The relaxation times τ_{cm} and τ_{ct} were calculated using Eqs. (4.12) and (4.14). τ_{ad} followed directly from the data fitting. Relative values are referred to the unpoisoned electrode at the same conditions.

T (°C)	$\Delta\phi_{\mathrm{dc}}$ (V)	τ_{cm} (10^{-4} s)	$\tau_{\mathrm{cm,rel}}$	τ_{ct} (s)	$\tau_{\mathrm{ct,rel}}$	τ_{ad} (s)	$\tau_{\mathrm{ad,rel}}$
30	0.00	3.2	1.3	0.073	21	4	0.7
30	0.05	5.3	2.3	1.01	220	9	1.1
50	0.00	12	1.2	0.0055	1.3	5	1.0
50	0.05	14	1.8	0.26	55	16	3.2

4.5 Discussion

In section 4.2 of this paper, we described our postulated three steps in the anode reaction. The new experimental data, obtained for electrodes equilibrated with 103 ppm CO, are discussed below with reference to these steps.

4.5.1 Hydrogen adsorption/desorption and diffusion

As hydrogen gas enters the porous electrode backing from the gas channel, the first step says that the gas is reversibly adsorbed to the carbon surface in the pores, and that the gas molecule migrates along this carbon surface to the catalyst particle.

A theoretical argument was given for the existence of such a step [80]: Direct access from the gas phase to the three-phase contact line is prohibited. Such an access leads to the divergence of the flux of hydrogen being infinite at the contact line, an impossible situation. Access is therefore via the interfaces between the materials that are involved. In the porous, gas-filled carbon, such an interface is provided by the carbon-gas interface. This interface will then eventually give access of hydrogen to the Pt particles. Such transport via the interface of two materials is in fact favourable, as it provides a more widely spaced access to the Pt particle. Also the interface between the membrane (Nafion) and the gas can provide a pathway. The variation in the phase angle with time, see Fig. 4.2, supports the idea that this kind of adsorption takes place. The figure shows two distinct phases, a rapid phase (when the chemical potential difference of CO between the gas and the surface is large) and a slow phase. The last phase can well be a reequilibration step across a porous layer, similar to the step seen for adsorption of gases in zeolites membranes [83].

As discussed earlier [62], the model does not discriminate between a molecular or an atomic state of hydrogen on the carbon surface. We have chosen to use molecular hydrogen in Eq. (4.2), because the adsorption on carbon is probably weak [78].

In the Results section, we showed that the experimental data in Figs. 4.5-4.8 could be fitted to the Gerischer impedance, cf. Table 4.2, Y_0 and τ_{ad}. f. Table 4.2, Y_0 and τ_{ad}. The fit to the two superimposed semi-circles have a high degree of uncertainty. It should be remembered that the model developed in our earlier work [80] is a premise of the analysis. The relaxation time τ_{ad} was measured in seconds after exposing the electrode surface to CO. The interesting fact is that this is precisely the same as observed in the unpoisoned electrode. Table

4.3, column 8, shows that the relaxation time of this step is unaffected by the presence of the CO-gas in the unpolarised electrode. This may be expected, if the state of the hydrogen on the carbon surface is unaltered.

If the argument about access to the catalyst holds for H_2, namely that the path to the catalyst is via the carbon-gas interface, it follows that also CO must follow the same path. A closer inspection of the variables, that define the relaxation time is therefore interesting. Most interesting is the admittance Y_0, given in Table 4.2. This value is reduced by a factor between 10 and 30 in the unpolarised cell when CO is present in the system, and a factor between 100 and 400 in the polarised cell. The reduction is expressed in $Y_{0,\mathrm{rel}}$, the ratio of admittances, in this table. Equation (4.9) gives a relation between the diffusion coefficient of hydrogen, the temperature and the hydrogen concentration on the surface.

We find that the reduction in the diffusion coefficient is by more than one order of magnitude, when a electrode with CO is compared to one without CO at the same temperature and same surface gas concentration. A reduction is likely if CO is binding to the carbon surface, and prevents H_2 from moving. The fractional coverage of platinum is high, 0.90 or 0.83, but it is also likely that some CO adsorbs to the carbon part of the electrode.

Using the assumption $k^{\mathrm{a}}_{\mathrm{H_2}} = k^{\mathrm{d}}_{\mathrm{H_2}}$, we calculated $D = 1 \times 10^{-7}$ m^2/s [80]. This assumption is less likely now, as the hydrogen concentration on the surface should be reduced in the presence of CO. This means that the diffusion coefficient does not account for all of the reduction in Y_0, as measured by $Y_{0,\mathrm{rel}}$. Also $c^{\mathrm{a}}_{\mathrm{H_2}}$ must be responsible for a reduction. Given that the relaxation time for hydrogen adsorption is unaltered, however, the adsorption of CO on the carbon matrix seems to be weak (physisorption).

According to Eq. (4.9) the admittance should change with a pressure change. This was not observed, but can be understood by the small value of Y_0. A possible variation in Y_0 with the pressure, like the one observed earlier [80], is not detectable within the accuracy in the experiment, when Y_0 becomes too small.

4.5.2 The charge transfer step

This investigation shows that the relaxation time of the charge transfer step, τ_{ct}, increases drastically in the presence of CO, see also $\tau_{\mathrm{ct,rel}}$ in Table 4.3. While the relaxation time of the adsorption step, and the proton hydration

step, barely changes, the relaxation time of the charge transfer step changes by more than one order of magnitude at both temperatures. Clearly the conditions at the surface for hydrogen oxidation are changed.

We know from Fig. 4.3 that the presence of CO reduces access of hydrogen to the platinum surface by a factor of ten. Access alone need not have an impact on the relaxation time. But CO is chemisorbed to the surface, as evidenced by its presence after nitrogen flushing. This plus the change in τ_{ct} indicate that CO also has changed the state of the surface and made it more polarisable. According to the literature [30, 79]), the bond made by CO to Pt, will lead to a localisation of electrons. The surface polarisation increases. The resistance increases, especially under a polarisation, meaning that the surface becomes more polarisable in the presence of CO. The increase in the system's resistance with an applied potential (Fig. 4.5) is in agreement with this view.

The catalyst layer of the PEM fuel cell electrode is porous, and has an extension of about 10 μm, which is significant compared to the thickness of the backing where gas transport takes place. This has led some researchers to describe the layer in a continuous fashion, taking the proton resistance along as a variable [84]. Our data do not allow for such a possibility, as the parameter α is constant, and there is no indication of diffusion in the second semicircle.

4.5.3 The proton hydration step

The relaxation time of the proton hydration step, τ_{cm}, is largely unaffected by the presence of CO, cf. Table 4.3. This is also what we should expect. Compared to the study without CO present, the two contributions to τ_{cm} have changed. The resistance has increased, while the capacitance has increased correspondingly. The more polarised surface discussed above can well result in a higher resistance to charge transfer. It is further likely that the presence of water in addition to CO at the surface modifies the capacitance.

4.6 Conclusion

The present impedance spectroscopy investigation of the anode reaction of the standard PEMFC in the presence of CO, has given additional experimental evidence in favour of a recently proposed three-step model for the electrode reaction [62, 80].

In particular we have found extra evidence for the hypothesis that the path of the reacting gas to the catalyst particle is via the interface of the porous

carbon phase and the gas phase. The hydrogen surface diffusion coefficient was clearly lowered compared to the diffusion coefficient that has been estimated earlier to 1×10^{-7} m^2/s. Carbon monoxide acts by hindering hydrogen access to the surface, by occupying the surface, and by making the surface more polarisable, as has also been observed by others [11, 12, 79]. The proton hydration step, needed for the proton to enter the ion-exchange membrane, is relatively unaffected by the presence of CO, and can only be distinguished from the other steps at low temperatures (30°C).

Acknowledgements

A.K. Meland is grateful to Nordic Energy Research and Norsk Hydro ASA for financial support. Rune Halseid is thanked for several constructive comments.

Chapter 5

The Butler-Volmer equation of the oxygen electrode in a polymer electrolyte membrane fuel cell

Anne-Kristine Meland and Signe Kjelstrup

Department of Chemistry
Norwegian University of Science and Technology,
N-7491 Trondheim, Norway

This paper has been submitted to
Electrochim. Acta

Abstract

The oxygen electrode in the polymer electrolyte membrane fuel cell (PEMFC) was examined using electrochemical impedance spectroscopy (EIS). The electrodes were E-TEK Elat gas diffusion electrodes with 0.5 mg Pt/cm^2 and the membrane was Nafion 117. Operating temperatures in the system were 30 and 50°C. Oxygen gas was fed into both sides of the system and the impedance was measured in the galvanostatic mode. The electrode impedance was also measured in the fuel cell. For the conditions used, with a potential around 0.7 V vs. the H_2 anode, we argue that the small, high-frequency, voltage-independent arc, is interpreted as coming from a proton dehydration step, whilst the main arc is associated with peroxide formation. The Butler-Volmer equation, fitted to experimental results for the two steps, gave a overall transfer coefficient β of 0.70±0.03 and an exchange current density, j_0, of $(9.42\pm0.01)\times10^{-5}$ A/cm^2 at 30°C.

5.1 Introduction

It is well known that the oxygen electrode is far from reversible, and is therefore cause of considerable dissipation of energy in almost all processes where it plays a role. The overpotential at the oxygen electrode is the single most important contribution to loss of efficiency in the polymer electrolyte fuel cell (PEMFC), and this has led to numerous investigations of the oxygen reduction reaction (ORR). Overviews are given by Damjanovic [85] and Tarasevich, Sadkowski and Yeager [86].

The cathodic reduction of oxygen in PEMFC takes place in an acidic environment, and the kinetics and mechanism for the cathodic reduction of oxygen are functions of many experimental factors like the cathode material and electrolyte. The difference between the reversible cell potential and open circuit potential is around 0.2 V. This then has lead one to suspect that reduction reactions take place in parallel, and that the observation is a result of mixed potentials [87, 88]. Slow dissolution of platinum in acidic solutions [89, 90, 91] has also been held responsible for the low potential [91].

Kinoshita et al. [88] proposed that the reduction of oxygen proceeds in two overall pathways; a direct 4 electron pathway (E_0=1.229 V)

$$O_2 + 4H^+ + 4e^- \rightarrow 2H_2O \tag{5.1}$$

and a peroxide pathway (E_0=0.67 V):

$$O_2 + 2H^+ + 2e^- \rightarrow H_2O_2 \tag{5.2}$$

followed by either the electro-reduction of peroxide (E_0=1.77 V):

$$H_2O_2 + 2H^+ + 2e^- \rightarrow 2H_2O \tag{5.3}$$

or the chemical decomposition of peroxide:

$$2H_2O_2 \rightarrow 2H_2O + O_2 \tag{5.4}$$

Here E_0 is the standard state potential for the reaction. Kuhn et al. [92] and Antoine et al. [93] found support for the direct 4 electron pathway.

The oxygen electrode in the polymer electrolyte fuel cell studied in this work, consists of catalyst ink containing platinum particles sprayed onto a porous carbon backing. Oxygen is supplied and most of the water that is formed is removed through the porous matrix. A water-containing proton-conducting membrane supplies hydrated protons [64] to the half cell reaction. The carbon phase gives electronic contact to the cell exterior.

We have earlier investigated the anode performance with such a porous PEMFC electrode, and found that a proton hydration step gives a possible rate-limiting step in the reaction mechanism [80]. A likely next hypothesis is thus that such a step also is possible on the cathode. The aim of this article is to study this possibility for conditions that favour peroxide formation (with applied potentials around 0.7 V vs. H_2 anode), in order to obtain the parameters of the Butler-Volmer equation for this series of steps. Such information is important in fuel cell modelling, as the typical operating range of the cell is around such a potential.

Rate-limiting steps in electrode reactions can be favourably examined by impedance spectroscopy. The technique has been used to examine processes in polymer electrolyte fuel cells [32, 33, 36]. Investigations have been done on the cell as a whole, and on the symmetrical cell with two hydrogen electrodes [30, 31, 33, 94, 95]. Also some investigations on the symmetric cell with two oxygen electrodes have been done [30, 33, 94], but the contribution from the water electrochemical reaction has not been obtained before. This work presents such results for a frequency range from 10 kHz to 10 mHz. We shall see that the data can be fitted well to a model for the oxygen reduction reaction with two steps;

$$H_3O^+ \rightarrow H^+ + H_2O \tag{5.5}$$

$$O_2 + 2H^+ + 2e^- \rightarrow H_2O_2 \tag{5.2}$$

It follows from the data (two possible arcs in the impedance diagram) that the third step most likely is a chemical step.

$$2H_2O_2 \rightarrow 2H_2O + O_2 \tag{5.4}$$

The overpotential of the oxygen electrode depends on the direction of the current density [96]. We shall therefore have to pay attention to the direction of the current, when we derive the single electrode impedance. The whole cell impedance and the cell with two hydrogen electrodes shall be used in combination with the cell with two oxygen electrodes, to find the cathodic as well as the anodic performance of the oxygen electrode. We shall then take advantage of earlier studies of the hydrogen electrode [62, 80] and of results for the regular fuel cell. The oxygen electrode shall be investigated with a constant current, at two temperatures, in a symmetrical cell ($O_2|O_2$), and also in a regular fuel cell ($H_2|O_2$). The overpotential characteristics of each electrode can then be found and the parameters of Butler-Volmer fitted.

5.2 Theory

The ac and dc potentials in an impedance experiment can be regarded independently; they are superimposed on one another, giving

$$Z_i^s = Z_{i,\mathrm{ac}}^s + Z_{i,\mathrm{dc}}^s \tag{5.6}$$

Subscript i refers to the anode or the cathode (a or c) and s refers to the surface. Electrode reactions that are far from reversible, have highly non-linear flux-force relations, and therefore a value of $Z_{i,\mathrm{dc}}^s$ that is non-linear in j_{dc}.

The Butler-Volmer equation gives the most general relation between the electrode overpotential and the cell current density, whilst the Tafel equation is the high current density version of this equation, found to apply below 0.6 V in the oxygen electrode of the fuel cell. The standard derivation of the Butler-Volmer equation uses the picture of an activated complex to be discharged or charged, at the top of an energy barrier in front of the metal surface, see i.e. [97]. In the present case we have illustrated this situation in Fig. 5.1.

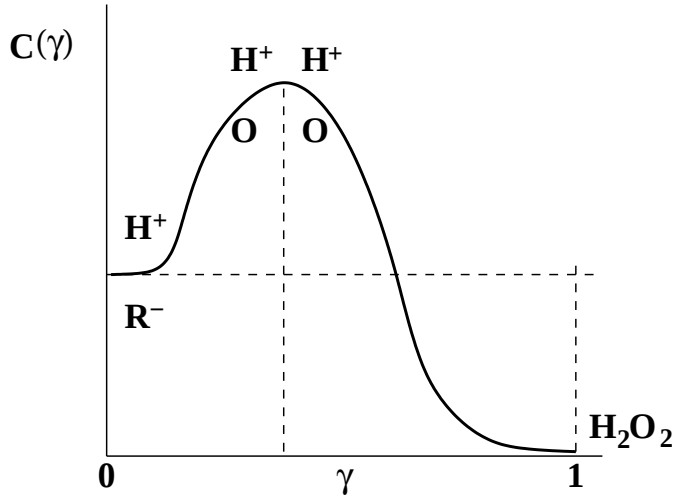

Figure 5.1. The enthalpy profile of the reacting mixture where the energy of the activated complex is raised to the peak of the energy barrier before they react. γ is the reaction coordinate.

Rubi and Kjelstrup [98] gave a derivation starting from the system's entropy production, and we shall give their derivation here, to emphasise the link between the overpotential and the dissipation of energy as heat. The first step in their procedure is to recognise as net driving force for the electrode reaction the sum of the chemical and the dc electric potential of the reacting mixture, $\Delta_s\phi_{\rm dc} + \Delta G/F$. The rate of the electrode reaction is proportional to the electric current density under dc conditions. The entropy production in the surface is therefore

$$\sigma^s = -\frac{j}{T^s}\left[\Delta_s\phi_{\rm dc} + \Delta G/F\right] \tag{5.7}$$

and the energy dissipated as heat is $T^s\sigma^s$. Nernst equation appears, when the process is reversible, i.e. when the entropy production, σ^s, is zero. This is in the limit of zero current density. Away from this limit, we find that the sum defines the electrode overpotential

$$\eta = \Delta_s\phi_{\rm dc} + \Delta G/F \tag{5.8}$$

This is obtained from the following argument. The overpotential is seen as the total resistance to charge transfer in the reaction, so

$$\eta = -R_{\rm tot}j \tag{5.9}$$

where R_{tot} is the surface resistance under dc conditions. The energy dissipated as heat at the electrode surface is given by the product ηj, an ohmic type loss:

$$T^s \sigma^s = -\eta j = R_{\text{tot}} j^2 \tag{5.10}$$

By comparing Eqs. (5.10) and (5.7), we obtain (5.8).

The non-linear relation between the overpotential and the current density cannot be deduced from the entropy production (Eq. 5.7), but it can be derived by studying the system on the mesoscopic level. Like in the common derivation of the Butler-Volmer equation, we introduce then the reaction coordinate γ as a variable. We assume now that thermodynamic relations can be written at any value of γ. This is the assumption of local electrochemical equilibrium in γ-space:

$$\int_{\gamma_1}^{\gamma_2} \sigma^s(\gamma)\, d\gamma = -\frac{j}{T^s} \int_{\gamma_1}^{\gamma_2} \left[\frac{\partial \phi(\gamma)}{\partial \gamma} + \frac{1}{F} \frac{\partial G(\gamma)}{\partial \gamma} \right] d\gamma \tag{5.11}$$

The local driving force, on this finer scale, is thus the combination of $\phi(\gamma)$ and $G(\gamma)/F$. We see that the entropy production of the surface, Eq. (5.7) is recovered by integrating Eq. (5.11) over the range of γ at constant j.

The reaction is also in this theory seen as proceeding over an activation energy barrier, $C(\gamma)$, see Fig. 5.1. In order to guide the thought, let us assume that the charge transfer step in the model (Eq. 5.2) dominates. Two protons stripped of water need to be activated in the presence of oxygen. The energy of the activated complex is raised to the peak of the energy barrier before they react. This is the situation illustrated in Fig. 5.1. The Gibbs energy of the reacting mixture at any position γ along the barrier is

$$G(\gamma) = C(\gamma) + RT \ln \Gamma(\gamma) \tag{5.12}$$

Here $\Gamma(\gamma)$ is the concentration of the activated reaction mixture. If the mixture is ideal, the function $C(\gamma)$ is the enthalpy profile of the activation energy barrier, see Fig. 5.1. The variation of $\Gamma(\gamma)$ has a minimum at the peak of the barrier.

A dc electric field is now applied to the system, so the total energy per unit of charge at any position γ changes to

$$\tilde{\mu}(\gamma) = C(\gamma) + RT \ln \Gamma(\gamma) + F\phi(\gamma) \tag{5.13}$$

Here F is Faraday's constant. The expression can be contracted to

$$\tilde{\mu}(\gamma) = RT \ln \left(f(\gamma) \Gamma(\gamma) \right) \tag{5.14}$$

where $f(\gamma)$ is the activity coefficient:

$$f(\gamma) = e^{(C(\gamma)+F\phi(\gamma))/RT} \tag{5.15}$$

When no current is drawn from the system, there is electrochemical equilibrium at the electrode. Equilibrium is characterised by a distribution of species $\Gamma(\gamma)$ over the γ-coordinate, with minimum concentration at the peak point as usual in reaction kinetics. The driving force for progress of the reaction at constant temperature is then [98]:

$$-\frac{d\tilde{\mu}(\gamma)}{d\gamma} = \frac{RT}{f(\gamma)\Gamma(\gamma)}\frac{df(\gamma)\Gamma(\gamma)}{d\gamma} \tag{5.16}$$

The system's entropy production $\sigma^s(\gamma)$ in Eq. (5.4) can now be rewritten for any state γ. In that state, the flux is a linear combination of the driving force, according to classical non-equilibrium thermodynamics. For isothermal dc conditions, the only flux is the electric current density, giving

$$\begin{aligned} j_{\mathrm{dc}} &= -L\frac{RT}{Ff\Gamma(\gamma)}\frac{df\Gamma(\gamma)}{d\gamma} \\ j_{\mathrm{dc}} &= -ue^{-(C+F\phi)/RT}\frac{d}{d\gamma}e^{\tilde{\mu}(\gamma)/RT} \end{aligned} \tag{5.17}$$

where the electric mobility of the ion is defined by $u = L/\left[F\Gamma(\gamma)\right]$. It was shown [98] that this equation can be integrated, assuming constant electric mobility, from $\gamma = 0$ to $\gamma = 1$ to give the familiar Butler-Volmer equation

$$j_{\mathrm{dc}} = j_0\left[e^{(1-\beta)\eta F/RT} - e^{-\beta\eta F/RT}\right] \tag{5.18}$$

with the overpotential defined by Eq. (5.8). The exchange current density found in this manner is, $j_0 = Le^{\tilde{\mu}_{eq}/RT}$ where $\tilde{\mu}_{eq}$ is defined from the equilibrium distribution along the reaction coordinate. The factor β defines the deviation of the real state from the equilibrium state, and can also in this derivation be interpreted as the overall transfer coefficient for the two-step reaction.

We shall perform the experiments under such conditions that both branches contribute. The data shall thus be fitted to the full Butler-Volmer equation (Eq. 5.18).

5.3 Experimental

5.3.1 The system

The electrode tested was a E-TEK Elat/Std/DS/V2 gas diffusion electrode with 0.5 mg Pt/cm^2 membrane area and 20% Pt/C on Vulcan XC-72. The electrode area was 4.91 cm^2.

To obtain a better ionic contact between the layers in the membrane and the electrode, the electrodes were sprayed with a 5% Nafion solution to give 0.6 mg Nafion/cm^2. The MEA consisted of two identical electrodes separated by a Nafion 117 membrane. The membranes were pretreated in several steps as described by Møller-Holst [51]. The pressure and temperature were constant during each experiment within a percent variations.

The experiments were done in a in-house fuel cell test station built by Møller-Holst [51] and modified by Vie [39]. The test station is described in previous papers [62, 80].

The gas pressures on the two sides of the MEA were always atmospheric. The temperature was constant during each experiment, 30 or 50°C. Most of the experiments were performed at 30°C. The oxygen gas (AGA 99.999%) and the hydrogen gas (AGA 99.999%) were humidified at 80°C before entering the cell housing.

The MEAs were conditioned as a fuel cell ($H_2|O_2$) and ran for 48 hours until stable polarisation curves were achieved. This was done with every new MEA.

5.3.2 Case studies

Most of the experiments were done at 30°C since the proton hydration step is better visible at this temperature [62, 80, 99]. The following systems were studied:

1. The fuel cell, denoted $H_2|O_2$, in a galvanostatic mode. The motivation for this was two fold. Firstly we wanted to see how far we were able to reproduce results that already are reported in the literature [29, 31, 32]. Secondly we needed the impedance of the cathode in the same cell that we have documented data for the hydrogen anode [80].

2. The symmetrical cell with two oxygen electrodes, denoted $O_2|O_2$. Care was taken to use the same current density in this cell as in the fuel cell in 1), so that a combination of the results was possible. The current density was always lower than 1 mA/cm^2, corresponding to an applied voltage around 0.7 V at 30°C, in order not to damage the MEA. Galvanostatic as well as potentiostatic mode was used. Potentiostatic mode revealed a shoulder in the impedance diagram.

5.3.3 Methods

Impedance diagrams were recorded using a PAR 263A/94 potentiostat and a Solartron 1260 FRA. The "Z-plot" software from Scribner Ass. Inc. was used to run the experiments. Measurements were made in a two-electrode set-up. The impedance was obtained by sweeping over the frequencies from 10 kHz to 10 mHz, recording 12 steps/decade.

Galvanostatic as well as potentiostatic experiments were done. In the potentiostatic experiments, an amplitude of 5 mV was used, and the applied dc potentials were in the 0.5-0.7 V range. In the galvanostatic experiments, the amplitude varied when the constant current density changed. The amplitude was never more than 5% of the constant current density. The current densities used varied between 0.17 and 0.22 mA/cm^2 with corresponding voltage between the anode and the cathode of about 0.60 V in the experiments done at 30°C. For the experiments done at 50°C the current density range was 0.5-1 mA/cm^2 with corresponding voltages of 0.85-0.95 V. For the $H_2|O_2$ cell the corresponding voltage was 0.96 V at the current densities mentioned above.

The galvanostatic mode of operation gave relatively more reproducible results than the potentiostatic ones, and was used with the wider range of current densities.

The potentiostatic mode of operation resulted in relatively rapid system failure at the highest current densities, but proved to be important at and near OCV conditions, because they were then less disturbed by noise.

The OCV of the $H_2|O_2$ cell was 1.00 V. When the experiments of the symmetric oxygen cell were done in the potentiostatic mode at voltages above 0.7 V (current densities higher than 1 mA/cm^2), we saw a change in the cell performance at both temperatures. The charge transfer arc got more depressed, and it was no longer possible to reproduce earlier experiments. It turned out that these high potentials were not a problem in the galvanostatic mode. Still this

region was avoided.

5.3.4 Data reduction

The measurements give the ac potential difference of the whole cell, and accordingly the cell impedance equal to

$$Z^{\text{cell}} = Z^{\text{mem}} + Z_a^s + Z_c^s \tag{5.19}$$

Here Z^{mem} is the impedance of the membrane electrolyte in the cell. When the two electrodes are equal as in the symmetrical cell with hydrogen electrodes, we have

$$Z_{\text{H}_2}^s = \frac{1}{2}(Z^{\text{cell}} - Z^{\text{mem}}) \tag{5.20}$$

The performance of the cathodic oxygen electrode, is derived from

$$Z_{\text{c,O}_2}^s = Z_{\text{H}_2|\text{O}_2}^{\text{cell}} - Z^{\text{mem}} - Z_{\text{H}_2}^s \tag{5.21}$$

while the performance of the anodic oxygen electrode is given by

$$Z_{\text{a,O}_2}^s = Z_{\text{O}_2|\text{O}_2}^{\text{cell}} - Z^{\text{mem}} - Z_{\text{c,O}_2}^s \tag{5.22}$$

The low-noise potentiostatic experiments showed two arcs. On this background we chose to interprete the data in terms of the reaction scheme Eq. (5.4) which has the equivalent circuit in Fig. 5.2. A constant phase element in parallel with a resistance was used for each arc. The mathematical equivalent is

$$Z_i = \frac{R_i}{1 + R_i T_i (i\omega)^{\alpha_i}} \tag{5.23}$$

The smaller α_i is, the more the arc is depressed, and when α_i=1, the CPE becomes a pure capacitance. The circuit for the whole cell is:

$$Z_{\text{cell}} = R_{\text{m}} + \frac{R_{\text{cm}}}{1 + R_{\text{cm}} T_{\text{cm}} (i\omega)^{\alpha_{\text{cm}}}} + \frac{R_{\text{ct}}}{1 + R_{\text{ct}} T_{\text{ct}} (i\omega)^{\alpha_{\text{ct}}}} \tag{5.24}$$

The spectra were fitted using the software Z-View (Scribner Associated Inc.) At the open circuit voltage (OCV), α_{ct} was found to be 0.82 for the O_2 $|O_2$ cell. This corresponds well with the values found for the charge transfer step of the same electrode, but with hydrogen gas; $H_2|H_2$ [80], and indicates that constant phase element is reasonable. The value of

$$R_{\text{tot}}^{\text{s}} = R_{\text{cm}} + R_{\text{ct}} \tag{5.25}$$

was calculated from the fits, and used to find the electrode overpotential from Eq. (5.9).

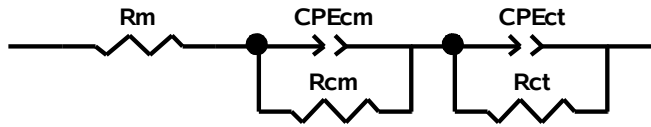

Figure 5.2. The equivalent circuit for the rate-limiting steps of the cathode of the PEMFC. The proton dehydration step gives the resistance R_{cm} and the constant phase element CPE_{cm}. The charge transfer step at a heterogenous surface contributes by R_{ct} and CPE_{ct}. The Nafion membrane resistance is denoted R_{m}.

5.4 Results

5.4.1 Experimental results

The $H_2|O_2$ impedance, shown in Fig. 5.3 confirm results obtained by others [29, 31, 32], cf. case study 1). The total resistance increases with increasing potential. There is one small high frequency arc and a dominating mid frequency arc. Paganin et al. [29] also observed the low frequency arc that disappears at higher potentials. All results were reproducible with an accuracy of 5%.

The potentiostatic results at 30°C are shown in Fig. 5.4. The fits to the equivalent circuit Fig. 5.2 for the model (Eqs. 5.2, 5.4 and 5.5) are also shown.

The potentiostatic experiments gave two arcs for the oxygen electrode, one small at the highest frequencies and one large dominating at the low frequencies, both at OCV and with a bias voltage. The small arc can be best seen when the high-frequency area is magnified, see Fig. 5.5. In the galvanostatic experiments no clear indication was found of a high frequency arc, neither at 30 nor at 50°C. There was some noise at the highest frequencies and we believe that the real signal was smaller than the noise. The experiments were done in a potential range, which favours peroxide formation. When the cell housing was opened after the $O_2|O_2$ experiments, a discolouring of the membrane was observed. The membrane had turned bright yellow and something had clearly happened during the experiments. This is therefore taken as a strong indication for peroxide formation in our system.

In the fit of the experimental data to the model, we found that the small arc did not change when the voltage was changed. This supports further the idea

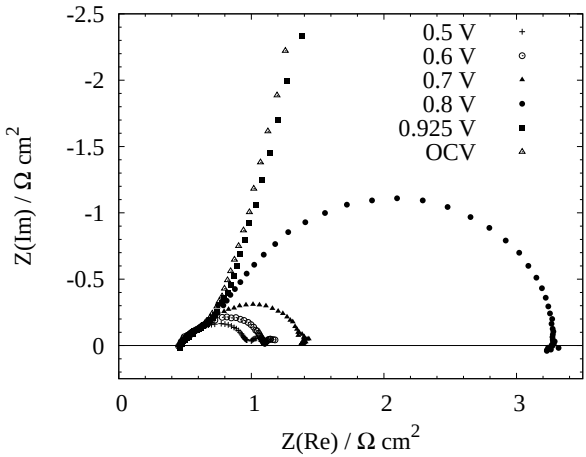

(a)

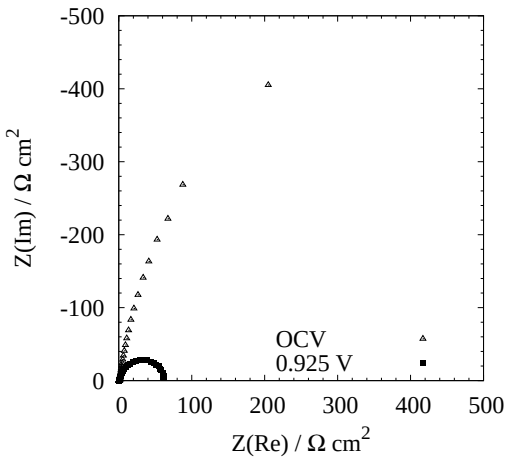

(b)

Figure 5.3. Nyquist diagram of the whole fuel cell (H_2 /O_2) at T=30°C and 1 bara.

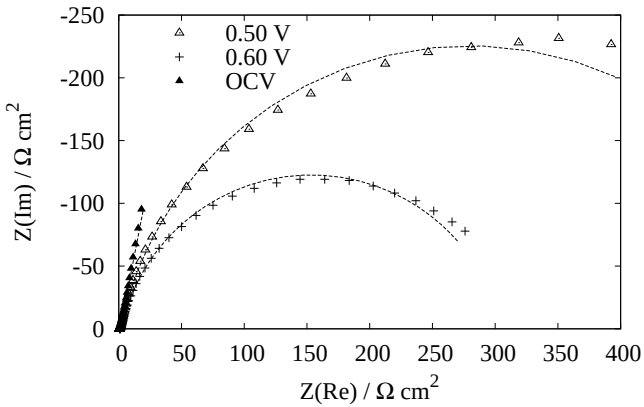

Figure 5.4. Nyquist diagram of the symmetric O_2/O_2 cell at 30° C, 1 bara, and different applied dc voltages.

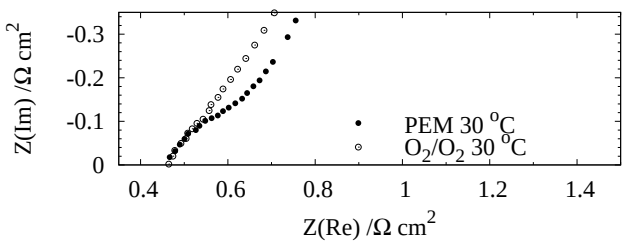

Figure 5.5. Nyquist diagram of O_2/O_2 cell and H_2/O_2 cell at 30° C, 1 bara, and OCV conditions. The high frequency part magnified.

that there is no charge transfer involved in this step.

A potential-independent semi-circle at the highest frequencies was observed not only for the symmetrical cell, but also for the fuel cell. The relaxation time for this proton hydration step at OCV and 30°, $\tau_{cm}^{O_2}$, was calculated to 0.22 s. At 50°C the relaxation time was 0.75 ms. We found earlier that the relaxation time for the hydrogen electrode at the same conditions $\tau_{cm}^{H_2}$ was 0.25 ms at 30°C. [80].

These facts taken together, all point in favour of an interpretation in terms of the model described with Eqs. (5.2), (5.4) and (5.5) and Fig. 5.2.

The galvanostatic results for the $O_2|O_2$ cell at 30°C are given in Fig. 5.6. Corresponding results for the $H_2|O_2$ cell are given in Fig. 5.7. The galvanostatic results were used to calculate the performances of the oxygen electrode as a cathode and as an anode, according to Eqs. (5.21) and (5.22). The contribution from H_2 anode was very small [62, 80].

The calculated anodic impedance of the oxygen electrode acting as an anode is shown in Figs. 5.8-5.11. Results for the cathode are also shown. We see from Figs. 5.8-5.11 that the charge transfer resistance from the anode is much larger than for the cathode.

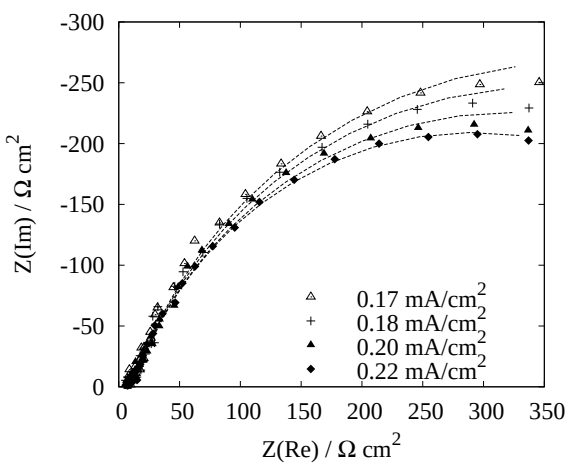

Figure 5.6. Nyquist diagram of the symmetric O_2/O_2 cell at 30°C, 1 bara, and different current densities.

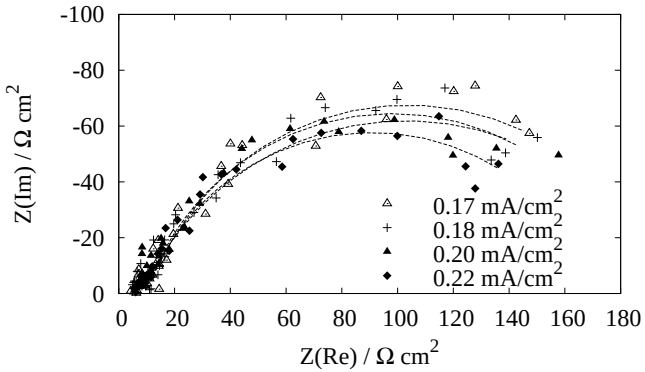

Figure 5.7. Nyquist diagram of the whole fuel cell, H_2/O_2, at 30° C, 1 bara, and different current densities.

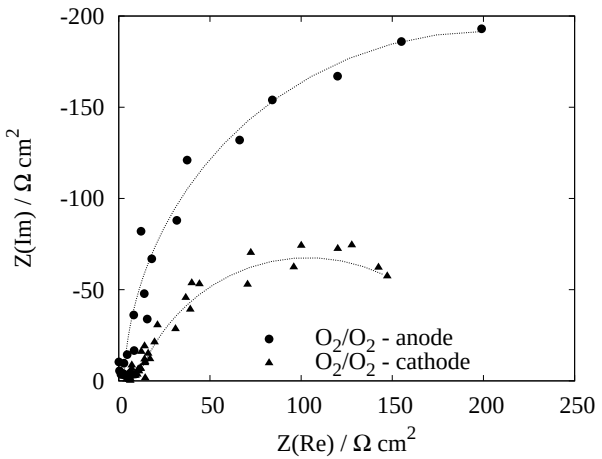

Figure 5.8. Nyquist diagram of the O_2/O_2 cell at 30° C and 1 bara in galvanostatic mode with a constant current density at 0.17 mA/cm^2.

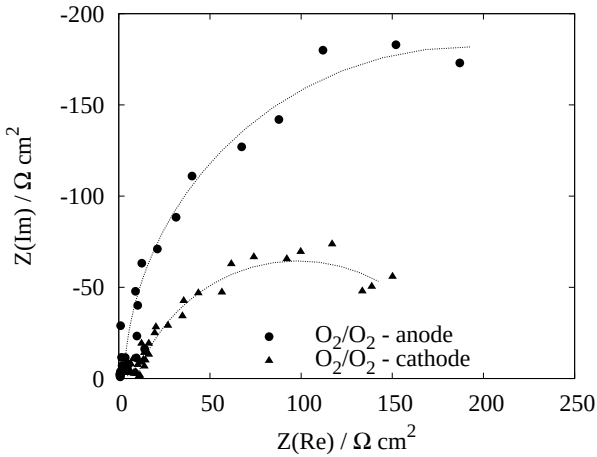

Figure 5.9. Nyquist diagram of the O_2/O_2 cell at 30°C and 1 bara in galvanostatic mode with a constant current density at 0.18 mA/cm^2.

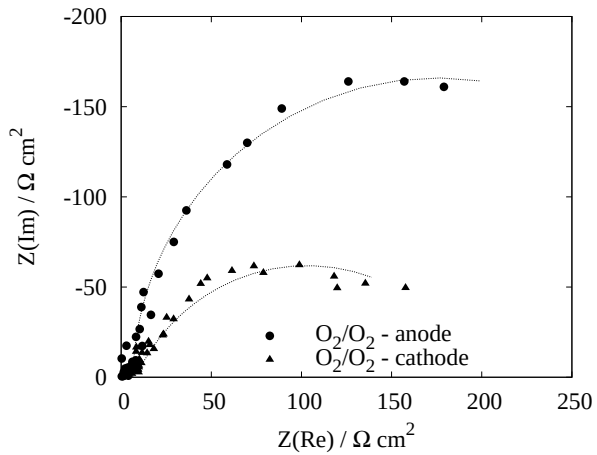

Figure 5.10. Nyquist diagram the O_2/O_2 cell at 30°C and 1 bara in galvanostatic mode with a constant current density at 0.20 mA/cm^2.

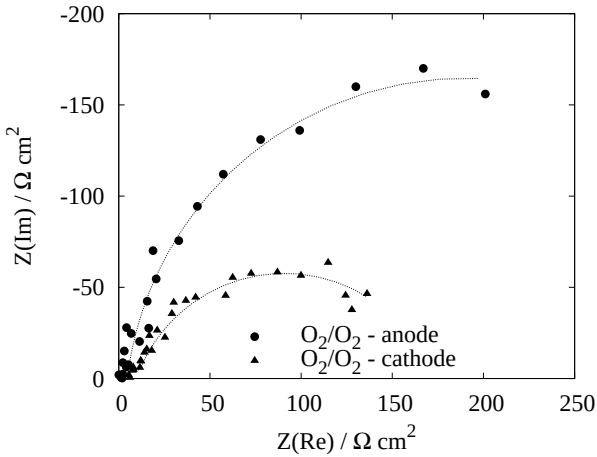

Figure 5.11. Nyquist diagram the O_2/O_2 cell at 30°C and 1 bara in galvanostatic mode with a constant current density at 0.22 mA/cm^2.

The results show that the charge transfer resistance decreases with increasing current density at both temperatures for the symmetric oxygen cell, in agreement with other observations [93]. As expected, the resistance also decrease with increasing temperature.

The overpotential was plotted as a function of the current density. The overpotential was calculated using the applied constant current and the resistances from the fitted data, using Eq. (5.8). The Butler-Volmer equation (5.18) was next used to fit the experimental data and is shown in Fig. 5.12. The value of β was found to be 0.70±0.03 and the exchange current density, j_0, was $(9.4 \pm 0.6)\times 10^{-5}$ A/cm^2. The measurements of the j and η was done in a narrow range because of experimental limitations. As seen from the plot, the cathodic branch of the total current rises more steeply than the anodic branch, a consequence of the high overall transfer coefficient factor.

5.5 Discussion

Our experimental results gave support to a fit of the data in terms of a particular mode of electrode operation, namely the mode given by Eq. (5.4), and the equivalent circuit in Fig. 5.2. From this we deduced the parameters in the Butler-Volmer equation. Below we discuss our findings also in view of results of other investigators.

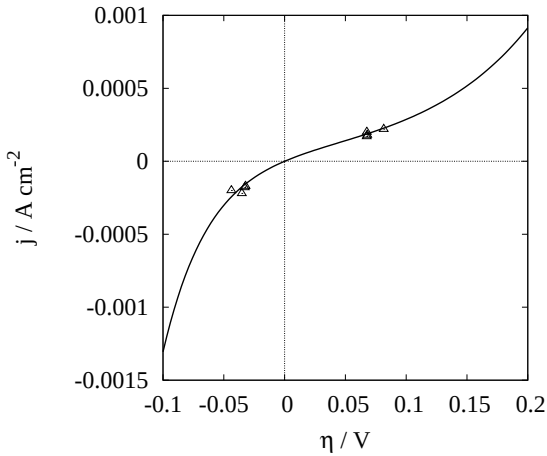

Figure 5.12. Butler-Volmer plot of the oxygen reduction reaction in the PEMFC.

5.5.1 Impedance spectra of the fuel cell electrodes

Several others have also observed two semi-circles for this reaction, including a high frequency arc. Romero-Castañón et al. [32] investigated the MEA in the PEM fuel cell using a reference electrode to separate the anode and cathode contribution. They discovered a small incomplete semicircle at the high frequencies for the $H_2|O_2$ cell, at all voltages including OCV. This semicircle did not vary with the potential. They concluded that the high frequency region was not associated with any faradic process nor with mass transport limitations on the cathode electrode side but to structural features of the MEA. This may also support our proposal about an initial proton dehydration step.

Hombrados et al. [33] found one arc in the mid frequency area for ORR and connected this to the charge transfer. At the lowest frequencies a line with almost 45°C angle was observed, and they associated this with a mass transfer (Warburg) impedance. They stopped the frequency sweep at 10 Hz, however. They used a PEMFC with a Nafion 117 membrane and measured when the fuel cell was in symmetrical mode ($O_2|O_2$) and 45% humidification of the reactant gases. Operating temperature was 40-70°C and OCV. We do not find any Warburg-like behaviour. Our use of OCV conditions, the presence of saturated water vapour, and absence of gas diffusion limitations makes it unlikely that one should observe a Warburg impedance usually attributed to mass transport limitations.

Kuhn et al. [92] observed from the EIS experiments an inductive semi-circle in the low frequency range in addition to a high frequency and a mid frequency arc. They assigned this inductive semi-circle to a second charge transfer step (the formation of OH_{ads} from the adsorbed O^-). They used non-impregnated electrodes that allow for an unhindered access of the gaseous species to the catalyst particle. These authors supported the reaction pathway of Damjanovic et al. [100] with two charge transfer steps. We do not find inductive contributions. According to Kuhn et al. [101] this is difficult to observe when the electrode is impregnated with an ionomere because the inductive loop will be masked, so we do also not expect to see this in our experiments.

The galvanostatic experiments were done in a potential range which favours peroxide formation, cf. Eq. (5.2). We observed that the membrane had turned yellow during the EIS experiments and belive that this is due to formation of peroxide. We also assign the small voltage-independent, high-frequency arc to a proton dehydration step (Eq. 5.5). The arc did not change with a change in bias voltage indicating that it is not a charge transfer step. Earlier investigations of the anode showed that a proton hydration step gives a possible rate-limiting step in the reaction mechanism [80]. Our hypothesis is that such a step can also occur at the cathode. The mechanism is illustrated in Fig. 5.13. Hydronium ion from the water-filled membrane splits into a proton and a water molecule. Oxygen molecules react with protons and electrons from the carbon phase and protons to form peroxide molecules at the platinum surface. This reaction is a more difficult than the one on the anode, and it is likely that the relaxation time for the proton dehydration is larger on the anode side then the cathode side. The surface diffusion of O_2 is shown at the bottom, and the still hydrated peroxide close to the upper Pt island.

5.5.2 The Butler-Volmer equation

The region close to OCV conditions is the region where the activation loss dominates in the fuel cell, and the loss is connected with the kinetics of the ORR. All experiments reported here were done in this voltage range. For the low current densities in this range, mass transport limitations are negligible [92]. This means that the overpotential we are working with is a pure activation overpotential.

We have not been able to find any reported values for β for PEMFC in the literature. Ciureanu and Wang [30] calculated what they called "apparent exchange current density" for a symmetrical oxygen cell where they used the

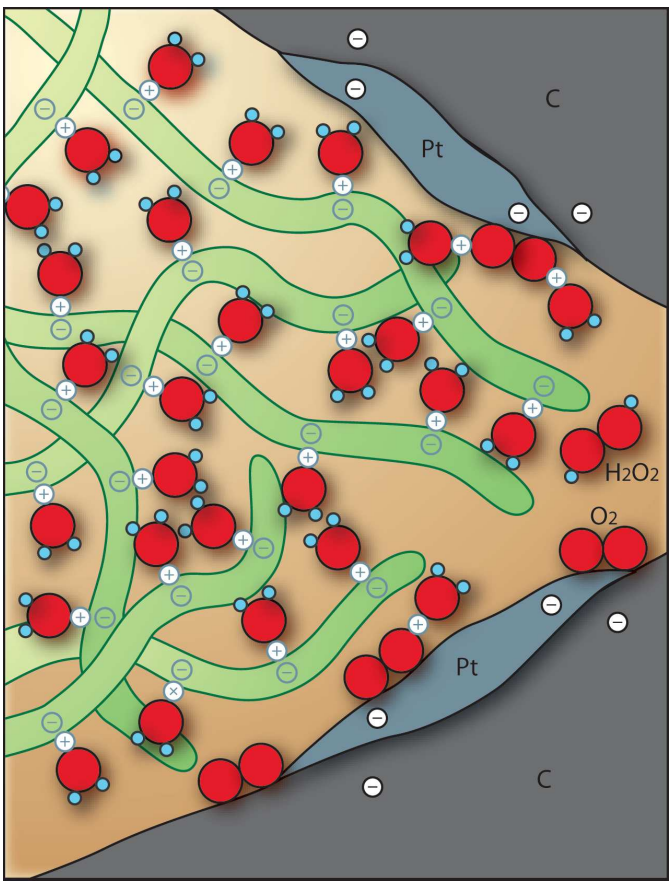

Figure 5.13. Illustration of the mechanism of the formation of hydrogen peroxide in the cathode of the PEMFC. Oxygen diffusion on carbon is shown at the bottom. The hydrated proton migrate along the negatively charged polymer, and react with oxygen at the platinum island in the upper part of the figure.

resistance for the charge transfer reaction related to the geometric surface area of the electrode. They used the value obtained from the EIS experiment and calculated the value to 8.6×10^{-5} A/cm^2. This is very similar to the value obtained from our fit to the Butler-Volmer equation, $(9.4 \pm 0.6)\times10^{-5}$ A/cm^2. The cathodic Tafel slope was calculated to -86 mV/decade which corresponds well with the Tafel slope calculated by Ihonen et al. [102] at low current densities and a cell temperature of 40°C.

The Butler-Volmer equation is needed for reliable fuel cell modelling at low overpotentials. We have shown above that the full equation need to be taken into account in the range of experimental parameters used here at low η.

5.6 Conclusion

The oxygen electrode in the polymer electrolyte membrane fuel cell was examined using electrochemical impedance spectroscopy. The electrodes were E-TEK Elat gas diffusion electrodes with 0.5 mg Pt/cm^2 and the membrane was Nafion 117. Operating temperatures in the system was 30°C. With a potential around 0.7 V vs. H_2 anode, the small voltage-independent, high-frequency arc can be interpreted as coming from a proton dehydration step, while the main arc is associated with peroxide formation. The anodic branch of the oxygen reduction reaction in the Butler-Volmer equation was determined. The Butler-Volmer equation fitted to experimental results for the two steps gave a overall transfer coefficient β of 0.70±0.03 and an exchange current density of $(9.42\pm0.01)\times10^{-5}$ A/cm^2 at 30°C.

Acknowledgements

A.K. Meland is grateful to Nordic Energy Research and Norsk Hydro ASA for financial support. Rune Halseid is thanked for valuable comments.

Chapter 6

Conclusions and further work

6.1 Conclusions

The electrodes of the polymer electrolyte membrane fuel cell (PEMFC) were studied in this thesis. The electrodes investigated were porous gas-diffusion electrodes (E-TEK Elat/Std/DS/V2) with 0.5 mg Pt/cm^2 and 20% Pt/C. These electrodes were impregnated with a 5 wt% Nafion solution to give 0.6 mg/cm^2. The two similar electrodes were separated by a Nafion 117 membrane. The geometric cell area was 5 cm^2. Electrochemical impedance spectroscopy (EIS) was used to study the electrode processes. A two electrode set-up was used in all the experiments. The frequency range used was 10 kHz-10 mHz. The operating temperatures were 30 and 50° with the emphasis on 30°.

We wanted to avoid a reference electrode and therefore used symmetrical cells. When studying the hydrogen oxidation reaction (HOR) at the anode, a $H_2|H_2$ cell was used. When studying the oxygen reduction reaction (ORR) an $O_2|O_2$ cell was used, and we also did experiments with the total fuel cell, the $H_2|O_2$ cell.

The contribution to the overpotential from the anode is almost negligible in a PEM fuel cell at normal operation compared to the contribution from the cathode. The HOR at the anode is a reversible reaction, and in a symmetrical hydrogen cell at OCV there is an equal contribution from both the electrodes.

The data were represented in Nyquist diagrams. By using irreversible thermodynamics we were able to make an equivalent circuit that represented our

experimental data well. The data were then analysed using this model and we saw that the data fitted the model well.

We found three rate-limiting steps at the anode, connected to different reactions. In the low frequency area we discovered the Gerischer behaviour. This behaviour was best seen at the lowest temperature. This showed that hydrogen diffused along the carbon pores in the electrode and that the adsorption reaction took place in combination with surface diffusion of hydrogen in the carbon layer located before the platinum surface. The reaction was thus not only dependent of the platinum catalyst particles. The surface coefficient of hydrogen diffusion was estimated to 10^{-7} m^2/s. We were not able to distinguish between molecular or atomic adsorption. The relaxation time for this rate-limiting adsorption/diffusion step was independent of bias voltage. In the mid frequency area we found the well known charge transfer step taking place at the platinum particles. In the high frequency area we discovered the was the proton hydration step. We showed that water plays an important role at the anode. This third step was best seen at the low temperature, 30°C, at 50°C this small arc was superimposed on the charge transfer arc in the Nyquist plot. We now had a model that described the processes at the anode.

We were then interested in how CO poisoning affected the fuel cell and with the background from the unpoisoned anode, we introduced 100 ppm CO into the fuel. When the anode is poisoned, even with a small amount as 100 ppm CO, the anode suddenly has an impact on the total loss in the PEM fuel cell. Bias voltages of 0 and 0.05 V were used. Three steps were again revealed in the reaction mechanism, the charge transfer step, the adsorption/diffusion step, and the proton hydration step. This confirmed earlier results from the unpoisoned anode. The CO had a big effect on the charge transfer step and the relaxation time increased drastically. The relaxation time for the adsorption/diffusion step was unaffected by the CO. We also concluded that CO reduces the diffusion rate of the surface diffusion of hydrogen on carbon. Also the relaxation time for the proton hydration step was unaffected by CO. CO hindered hydrogen access to the Pt surface, occupied the Pt surface and made the surface more polarisable. From cyclic voltammetry and stripping voltammetry experiments we found the CO coverage to be 0.90 at 30°C and 0.85 at 50°C.

We then looked at the ORR at the cathode. The oxygen electrode is not reversible like the hydrogen electrode. The symmetric oxygen cell was therefore investigated both in galvanostatic mode where we were able to control the

amount of electrons passing in the system. To be able to find the contributions from the anode and the cathode in the oxygen cell, the whole fuel cell was also investigated at the same conditions as the symmetric oxygen cell. The anodic and cathodic contribution of the oxygen electrode were then discovered. We found two rate-limiting steps. One dominating arc in the Nyquist diagram related to the charge transfer reaction and one small high frequency arc that we assigned to a proton dehydration step. This small high frequent arc did not change with the bias voltage. We belive we had peroxide formation followed by decomposition of peroxide. The Butler-Volmer equation was also fitted to the experimental data. The transfer coefficient β was determined to 0.70 $\pm$ 0.03 and the exchange current density, j_0 was (0.094 $\pm$ 0.0001) mA/cm^2.

6.2 Further work

More experiments are necessary to be able to fully understand the anode in the PEM fuel cell. We were not able to distinguish between molecular and atomic diffusion of hydrogen. We assumed that there was molecular diffusion, but we need more knowledge about the surface diffusion constant of hydrogen. Also the role of water has to be clarified. To learn more about this, more EIS experiments are needed where the temperature range is extended. Also other experimental techniques, like Neutron Diffraction, should be used to find out more about the anode structure. EIS experiments with different Nafion membranes should also be performed and a wide temperature range should be used. The model as it is today, is only valid for the gas-diffusion teflon-bonded electrode with the Nafion 117 membrane. One should try to get more information about other systems as well and see how this experimental data corresponds with the developed model.

For the poisoned anode, different levels of CO could be used. It is known from other researchers that the anode reacts differently dependent of the concentration of CO in the fuel. As a starting point, 2% CO should be fed to the electrode. Also more bias potentials should be used in the experiments, both at 100 ppm and 2% CO.

From the experiments at the oxygen electrode, several current densities in galvanostatic mode should be performed to get more information, more data in a wider current and potential range, for the fit to the Butler-Volmer equation. The temperature range should also be extended to higher temperatures to see how this affects the electrode.

Bibliography

[1] http://www.fuelcell.no/principle_history_eng.htm. Last visited 10.06.2007.

[2] C. Stone and A.E. Morrison. From curiosity to "power to change the world". *Solid State Ionics*, 152-153:1–13, 2002.

[3] L.J.M.J. Blomen and M.N. Mugerwa, editors. *Fuel Cell Systems*. Plenum Press, 1993.

[4] R. von Helmholt and U. Eberle. Fuel cell viechles: Status 2007. *J. Power Sources*, 165:833–843, 2007.

[5] http://www.fuelcelltoday.com/FuelCellToday/EducationCentre/ EducationCentreExternal/EduCentreDisplay/0,1741,History,00.html, Last visited 10.06.2007.

[6] M. Eikerling, A. Kornyshev, and A. Kulikovsky. Can theory help to improve fuel cells? *The Fuel Cell Review*, January:15–24, 2005.

[7] http://www.greencarcongress.com/2007/05/chevy_sequel_dr.html. Last visited 10.06.2007.

[8] H.S. Lee, H.J. Kim, and S.H. Ahn. Evalutation of grapite composite bipolar plate for PEM (proton exchange membrane) fuel cells: Electrical, mechanical, and molding properties. *Mater. Proc. Tech.*, 187-188:425–428, 2007.

[9] W.H. Zhu, R.U. Payne, D.R. Cahela, and B.J. Tatachuk. Uniformity analysis at MEA and stack levels for a Nexa PEM fuel cell system. *J. Power Sources*, 128:231–238, 2004.

[10] X. Cheng, Z. Shi, N. Glass, L. Zhang, J. Zhan, D. Song, Z.-S. Liu, H. Wang, and J. Shen. A review of PEM fuel cell contamination: Impacts, mechanismes, and mitigation. *J. Power Sources*, 165:739–756, 2007.

[11] P. Forzatti and L. Lietti. Catalyst deactivation. *Catal. Today*, 52:165–181, 1999.

[12] C.H. Bartholomew. Mechanism of catalyst deactivation. *Appl. Catal. A*, 212:17–60, 2001.

[13] Z. Qi, C. He, and A. Kaufmann. Poisoning of proton exchange membrane fuel cell cathode by CO in the anode fuel. *Electrochem. Solid-State Lett.*, 4(12):A204–A205, 2001.

[14] Z. Qi, C. He, and A. Kaufmann. Effect of CO in the anode fuel on the performance of PEM fuel cell cathode. *J. Power Sources*, 111:239–247, 2002.

[15] R.W. Reeve, P.A. Christensen, A.J. Dickinson, A. Hamnett, and K. Scott. Methanmol-tolerant oxygen reduction catalysts based on transition metal sulfides and their application to the study of methanol permeation. *Electrochim. Acta*, 45:4273–4250, 2000.

[16] M. Pabatti, P.J. Sebastian, and X. Mathew. Synthesis and characterization of $W_x(CO)_n$ electrocatalyst for application in a fuel cell electrode. *J. New Mater. Electrochem. Syst.*, 4(1):7–9, 2001.

[17] M.S. Wilson and S. Gottesfeld. Thin-film catalyst layers for polymer electrolyte fuel cell electrodes. *J. Appl. Electrochem.*, 22:1–7, 1992.

[18] E. Gulzow, M. Schulze, N. Wagner, T. Kaz, R. Schneider, and R. Reissner. New dry preparation techniquies for membrane electrode assemblies for PEM fuel cells. *Fuel Cell Bull.*, 15:8–12, 1999.

[19] E.J. Taylor, E.B. Anderson, and N.R.K. Vilambi. Preparation of high-platinum-utilization gas diffusion electrodes for proton-exchange-membrane fuel cells. *J. Electrochem. Soc.*, 139(5):L45–L46, 1992.

[20] O. Savadogo. Emerging membranes for electrochemical systems: (I) Solid polymer electrolyte membranes for fuel cell systems. *J. New Mater. Electrochem. Syst.*, 1:47–66, 1998.

[21] S. Srinivasan, H.D. Hurwitz, and J.O'M. Bockris. Fundamental equations of electrochemical kinetics at porous gas-diffusion electrodes. *J. Chem. Phys.*, 46(8):3108–3122, 1967.

[22] S. Srinivasan and H.D. Hurwitz. Theory of a thin film model of porous gas-diffusion electrodes. *Electrochim. Acta*, 12:495–512, 1967.

[23] J. Giner and C. Hunter. The mechanism of operation of the teflon-bonded gas diffusion electrode: A mathematical model. *J. Electrochem. Soc.*, 116:1124–1130, 1969.

[24] M.B. Cutlip. An approximate model for mass transfer with reaction in porous gas diffusion electrodes. *Electrochim. Acta*, 20:767–773, 1975.

[25] R.P. Iczkowski and M.B. Cutlip. Voltage losses in fuel cell cathodes. *J. Electrochem. Soc.*, 127(7):1433–1440, 1980.

[26] P. Bjornbom. Modelling of a double-layered PTFE-bonded oxygen electrode. *Electrochim. Acta*, 32(1):115–119, 1987.

[27] T.E. Springer and I.D. Raistrick. Electrical impedance of a pore wall for the flooded agglomerate model of porous gas-diffusion electrodes. *J. Electrochem. Soc.*, 136(6):1594–1603, 1989.

[28] I.D. Raistrick. Impedance studies of porous electrodes. *Electrochim. Acta*, 35(10):1579–1586, 1990.

[29] V.A. Paganin, C.L.F. Oliveira, E.A. Ticianelli, T.E. Springer, and E.R. Gonzalez. Modelistic interpretation of the impedance response of a polymer electrolyte fuel cell. *Electrochim. Acta*, 43:3761–3766, 1998.

[30] M. Ciureanu and H. Wang. Electrochemical impedance study of electrode-membrane assemblies in PEM fuel cells I. Electro-oxidation of H_2 and H_2/CO mixtures on Pt-based gas-diffusion electrodes. *J. Electrochem. Soc.*, 146(11):4031–4040, 1999.

[31] J.-D. Kim, Y.-I. Park, K. Kobayashi, M. Nagai, and M. Kunimatsu. Characterization of CO tolerance of PEMFC by AC impedance spectroscopy. *Solid State Ionics*, 140:313–325, 2001.

[32] T Romero-Castanon, L.G. Arriaga, and U. Cano-Castillo. Impedance spectroscopy as a tool in the evaluation of MEA's. *J. Power Sources*, 2003.

[33] A.G. Hombrados, L. Gonzalez, M.A. Rubio, W. Agila, E. Villanueva, D. Guinea, E. Chinarro, B. Moreno, and J.R. Jurado. Symmetrical electrode mode for PEMFC characterisation using impedance spectroscopy. *J. Power Sources*, 151:25–31, 2005.

[34] D. Bedeaux and S. Kjelstrup. Heat, mass and charge transport, and chemical reactions at surfaces. *Int. J. Thermodynamics*, 8(1):25–41, 2005.

[35] S. Kjelstrup and D. Bedeaux. Non-equilibrium thermodynamics for heterogenous systems. *World Scientific*, Submitted.

[36] T.E. Springer, T.A. Zawodzinski, M.S. Wilson, and S. Gottesfeld. Characterization of polymer electrolyte fuel cells using ac impedance spectroscopy. *J. Electrochem. Soc*, 143:587–599, 1996.

[37] D.A. Harrington and B.E. Conway. AC impedance of faradaic reactions involving electrosorbed intermediates-i. kinetic theory. *Electrochim. Acta*, 32:1703–1712, 1987.

[38] S. Kjelstrup, P. Pugazhendi, and D. Bedeaux. Impedance of the hydrogen polymer fuel cell electrode. theory and experiments. *Z. Phys. Chem.*, 214(7):895–916, 2000.

[39] P.J.S. Vie. *Characterisation and Optimisation of the Polymer Electrolyte Fuel Cell*. PhD thesis, Norwegian University of Science and Technology, Department of Chemistry, Trondheim, Norway, 2002. ISBN 82-471-5431-5, ISSN 0809-103X.

[40] T.J.P. Freire and E.R. Gonzalez. Effect of membrane characteristics and humidification conditions on the impedance response of polymer electrolyte fuel cells. *J. Electroanal. Chem.*, 503:57–68, 2001.

[41] P.M. Gomadam, J. W. Weidner, T. A. Zawodzinski, and A. P. Saab. Theoretical analysis for obtaining physical properties of composite electrodes. *J. Electrochem. Soc.*, 150(8):E371–E376, 2003.

[42] S.M. Lee, K.H. An, Y.H. Lee, G. Seifert, and T. Frauenheim. Novel mechanism of hydrogen storage in carbon nanotubes. *J. Korean Phys. Soc.*, 38:686–691, 2001.

[43] S.L. Chen and A. Kucernak. Electrocatalysis under conditions of high mass transport: Investigation of hydrogen oxidation on single submicron Pt particles supported on carbon. *J. Phys. Chem. B*, 108:13984–13994, 2004.

[44] A.Z. Weber and J. Newman. Transport in polymer-electrolyte membranes ii. Mathematical model. *J. Electrochem. Soc.*, 151(2):A311–A325, 2004.

[45] S. Kjelstrup, P.J.S. Vie, and D. Bedeaux. *Surface Chemistry and Electrochemistry of Membranes, T.S. Sørensen, ed.*, chapter Irreversible thermodynamics of membrane surface transport with application to polymer fuel cells, pages 483–510. Marcel Dekker, New York, 1999.

[46] W.H. Mulder and J.H. Sluyters. An explanation of depressed semi-circular arcs in impedance plots for irreversible electrode reactions. *Electrochim. Acta*, 33(3):303–310, 1988.

[47] J.W. Gibbs. *The Scientific Papers of J.W. Gibbs.* Dover, New York, 1961.

[48] M. Gonzales-Cuenca, W. Zipprich, B.A. Boukamp, G. Pudmich, and F. Tietz. Impedance on chromite titanate porous electrodes under reducing conditions. *Fuel Cells*, 1:256–264, 2001.

[49] P. Holtappels, J. Bradley, J.T.S. Irvine, A. Kaiser, and M. Mogensen. Electrochemical characterization of ceramic SOFC anodes. *J. Electrochem. Soc.*, 148:A923–A929, 2001.

[50] D. Bedeaux and S. Kjelstrup. The impedance of an electrode surface described by irreversible thermodynamics. *J. Non-Equil. Thermody.*, 24:80–96, 1999.

[51] S. Møller-Holst. Preparation and evaluation of electrodes for solid polymer fuel cells. *Denki Kagaku*, 64:699–705, 1996.

[52] J. Xie, D.L. Wood III, D.M. Wayne, T.A. Zawodzinski, P. Atanassov, and R.L. Borpu. Durability of PEFCs at high humidity conditions. *J. Electrochem. Soc.*, 152(1):A104–A113, 2005.

[53] T. Biegler, D.A.J. Rand, and R. Woods. Limiting oxygen coverage on platinized platinum - relevance to determination of real platinum area by hydrogen adsorption. *J. Electroanal. Chem.*, 29:269–277, 1971.

[54] J.A. Harrison and Z.A. Khan. The oxidation of hydrogen. *J. Electroanal. Chem.*, 30:327–330, 1971.

[55] A. le Méhauté and G. Crepy. Introduction to transfer and motion in fractal media: The geometry of kinetics. *Solid State Ionics*, 9-10(1):17–30, 1983.

[56] M. Brown, S. Primdahl, and M. Mogensen. Structure/performance relations for Ni/yttria-stabilized zirconia anodes for solid oxide fuel cells. *J. Electrochem. Soc.*, 147:475–485, 2000.

[57] E. Budevski. Structural aspects of fuel cell electrodes. *J. Optoelectron. Adv. M.*, 5:1319–1325, 2003.

[58] R.B. Bird, W.E. Stewart, and E.N. Lightfoot. *Transport Phenomena.* Wiley, Chichester, UK, 1960.

[59] Y.-S. Bae and C.-H. Lee. Sorption kinetics of eight gases on a carbon molecular sieve at elevated pressure. *Carbon*, pages 95–107, 2005.

[60] S. Kjelstrup and A. Røsjorde. Local and total entropy production and heat and water fluxes in a one-dimensional polymer electrolyte fuel cell. *J. Phys. Chem. B*, 109:9020–9033, 2005.

[61] F. Jaouen, G. Lindbergh, and G. Sundholm. Investigation of mass-transport limitations in the solid polymer fuel cell cathode. *J. Electrochem. Soc.*, 149:A437–A447, 2002.

[62] A.-K. Meland, D. Bedeaux, and S. Kjelstrup. A Gerischer phase element in the impedance diagram of the polymer electrolyte membrane fuel cell anode. *J. Phys. Chem. B*, 109(45):21380–21388, 2005.

[63] U.A. Paulus, Z. Veziridis, B. Schnyder, M. Kuhnke, G.G. Scherer, and A. Wokaun. Fundamental investigation of catalyst utilization at the electrode/solid polymer electrolyte interface Part i. Development of a model system. *J. Electroanal. Chem.*, 541:77–91, 2003.

[64] Magnar Ottøy. *Mass and Heat Transfer in Ion-Exchange Membranes.* PhD thesis, Norwegian University of Science and Technology, Department of Physical Chemistry, Trondheim, Norway, 1996. ISBN 82-7119-933-1, ISSN 0802-3271.

[65] T.A. Zawodzinski, T.E. Springer, J. Davey, R. Jestel, C. Lopez, J. Valerio, and S. Gottesfeld. A comparative study of water uptake by and transport through ionomeric fuel cell. *J. Electrochem. Soc.*, 140(7):1981–1985, 1993.

[66] P. Vie and S. Kjelstrup. Thermal conductivites from temperature profiles in the polymer electrolyte fuel cell. *Electrochim. Acta*, 49:1069–1077, 2004.

[67] Y. Sone, P. Ekdunge, and D. Simonsson. Proton conductivity of Nafion 117 as measured by a four-electrode AC impedance method. *J. Electrochem. Soc.*, 143(4):1254–1259, 1996.

[68] Christoph Hartnig. Personal communication.

[69] Schneider I.A., D. Kramer, A. Wokaun, and Scherer G.G. Spatially resolved characterization of PEFCs using simultaneously neutron radiography and locally resolved impedance spectroscopy. *Electrochem. Commun.*, 7:1393–1397, 2005.

[70] K.A. Mauritz and R.B. Moore. State of understanding of Nafion. *Chem. Rev.*, 104:4535–4585, 2004.

[71] T.E. Springer, T.A. Zawodzinski, and S. Gottesfeld. Polymer electrolyte fuel-cell model. *J. Electrochem. Soc.*, 138(8):2334–2342, 1991.

[72] M. Eikerling, Y.I. Kharkats, A.A. Kornyshev, and Y.M. Volfkovich. Phenomenological theory of electro-osmotic effect and water management in polymer electrolyte proton-conducting membranes. *J. Electrochem. Soc.*, 145(8):2684–2699, 1998.

[73] K. Broka and P. Ekdunge. Oxygen and hydrogen permeation properties and water uptake of Nafion 117 membrane and recast film for PEM fuel cell. *J. Appl. Electrochem.*, 27(2):117–123, 1997.

[74] J.T. Hinatsu, M. Mizuhata, and H. Takenaka. Water uptake of perfluorosulfonic acid membranes from liquid water and water vapor. *J. Electrochem. Soc.*, 141(6):1493–1498, 1994.

[75] T.A. Zawodzinski, C. Derouin, S. Radzinski, R.J. Sherman, V.T. Smith, T.E. Springer, and S. Gottesfeld. Water-uptake by and transport through Nafion 117 membranes. *J. Electrochem. Soc.*, 140(4):1041–1047, 1993.

[76] P.C Rieke and N.E. Vanderborgh. Temperature-dependence of water-uptake and proton conductivity in polyperfluorosulfonic acid membranes. *J. Mem. Sci.*, 32:313–328, 1987.

[77] J.C. Amphlett, K.A.M. Creber, J.M. Davis, R.F. Mann, B.A. Peppley, and D.M. Stokes. Hydrogen production by steam reforming of methanok for polymer electrolyte fuel cells. *Int. J. Hydrogen Energy*, 19(2):131–137, 1994.

[78] R.J. Bellows, E.P. Marucchi-Soos, and D.T. Buckley. Analysis of reaction kinetics for carbon monoxide and carbon dioxide on polycrystalline platinum relative to fuel cell operation. *Ind. Eng. Chem. Res.*, 35:1235–1242, 1996.

[79] P. Stoneheart and G. Kohlmayr. Effect of poisons on kinetic parameters for platinum electrocatalyst sites. *Electrochim. Acta*, 17:369–382, 1972.

[80] A.-K. Meland, S. Kjelstrup, and D. Bedeaux. Rate limiting proton hydration in the anode of the polymer electrolyte membrane fuel cell. *J. Mem. Sci.*, 282:96–108, 2006.

[81] J.M. Feliu, J.M. Orts, A. Fernandez-Vega, and A. Aldaz. Electrochemical studies in sulphuric acid solutions of adsorbed CO onPt(111) electrodes. *J. Electroanal. Chem.*, 296:191–201, 1990.

[82] M.J. Waver, S.-C. Chang, L.-W.H. Leung, and X. Jiang. Evaluation of absolute saturation coverages of carbon monoxide on ordered low-index platnium and rhodium electrodes. *J. Electroanal. Chem.*, 327:247–260, 1992.

[83] I. Inzoli, J.M. Simon, S. Kjelstrup, and D. Bedeaux. Temperaure effects during the adsorption of n-butane on a silicalite-1 membrane. A non-equilibrium molecular dynamics study. *J. Colloid. Interf. Sci.*, 313:563–573, 2007.

[84] G.J.M. Janssen and E.F. Sitters. Performance of thin-film cathodes for proton-exchange-membrane fuel cells based on high-surface-area carbon supports. *J. Power Sources*, doi:10.1016/j.jpowsour.2006.11.008, 2007.

[85] A. Damjanovic. *Progress in the Studies of Oxygen Reduction during the Last Thirty Years.* Electrochemistry in Transition From the 20th to the 21st Century. Plenum Press, New York, 1992.

[86] M.R. Tarasevich, A. Sadkowski, and E. Yeager. *Kinetics and Mechanisms of Electrode Processes.* Comprehensive Treatise of Electrochemistry. Plenum Press, New York, 1983.

[87] J.P. Hoare. *The Electrochemistry of Oxygen.* Interscience, New York, 1968.

[88] K. Kinoshita. *Electrochemical Oxygen Technology.* Interscience, New York, 1992.

[89] K. Kinoshita, J.T. Lundquist, and P. Stonehart. Potential cycling effects on platinum electrocatalyst surfaces. *J. Electroanal. Chem.*, 48:157–166, 1973.

[90] R.M. Darling and J.P. Meyers. Kinetic model of platinum dissolution. *J. Electrochem. Soc.*, 150:A1523–A1527, 2003.

[91] D.B. Sepa and M.V. Vojnovic. Reaction intermediates as controlling factor in the kinetics and mechanism of oxygen reduction at platinum electrodes. *Electrochim. Acta*, 26(6):781–793, 1981.

[92] H. Kuhn, A. Wokaun, and G.G. Scherer. Exploring single electrode reactions in polymer electrolute fuel cells. *Electrochim. Acta*, 52(6):2322–2327, 2007.

[93] O. Antoine, Y. Bultel, and R. Durand. Oxygen reduction freaction kinetics and mechanism on platinum nanoparticles inside Nafion. *J. Electroanal. Chem*, 499:85–94, 2001.

[94] N. Wagner, W. Schnurnberger, B. Muller, and M. Lang. Electrochemial impedance spectra of solid-oxide fuel cells and polymer membrane fuel cells. *Electrochim. Acta*, 43(24):3785–3793, 1998.

[95] O. Himanen, T. Hottinen, M. Mikkola, and V. Saarinen. Characterization of membrane electrode assembly with hydrogen-hydrogen cell and ac-impedance spectroscopy. Part I. Experimental. *Electrochim. Acta*, 52:206–214, 2006.

[96] B. Andreaus, A.J. McEvoy, and G.G. Scherer. Analysis of performance losses in polymer electrolyte fuel cells at high current densities by impedance spectroscopy. *Electrochim. Acta*, 47:2223–2229, 2002.

[97] J.O'M. Bockris and D.M. Drazic. *Electro-chemical Science*. Taylor and Francis, London, 1972.

[98] J.M. Rubi and S. Kjelstrup. Mesoscopic nonequilibrium thermodynamics gives the same thermodynamis basic to Butler-Volmer and Nernst equations. *J. Phys. Chem*, 107:13471–13477, 2003.

[99] A.-K. Meland and S. Kjelstrup. Three steps in the anode reaction of the polymer electrolyte membrane fuel cell. Effect of CO. *J. Electoanal. Chem.*, 10.1016/j.jelechem.2007.07.008, 2007.

[100] A. Damjanovic and V. Brusic. Electrode kinetics of oxygen reduction on oxide-free platinum electrodes. *Electrochim. Acta*, 12:615–628, 1967.

[101] H. Kuhn, B. Andreaus, A. Wokaun, and G.G. Scherer. Electrochemical impedance spectroscopy applied to polymer electrolyte fuel cells with a pseudo reference electrode arrangement. *Electrochim. Acta*, 51:1622–1628, 2006.

[102] J. Ihonen, F. Jaouen, G. Lindbergh, A. Lundblad, and G. Sundholm. Investigation of mass-transport limitations in the solid polymer fuel cell cathode. *J. Electrochem. Soc.*, 149(4):A448–A454, 2002.